Technische Universität München
TUM School of Engineering and Design

Wind Turbine Tower Top Motion Assessment for the Development of a Digital Shadow

Johannes Rupfle

Vollständiger Abdruck der von der TUM School of Engineering and Design der Technischen Universität München zur Erlangung eines

Doktors der Ingenieurswissenschaften (Dr.-Ing.)

genehmigten Dissertation.

Vorsitz:
Prof. Dr.-Ing. Boris Lohmann

Prüfende der Dissertation:
1. Prof. Dr.-Ing. Christian U. Große
2. Prof. Dr.ir. Daniel J. Rixen

Die Dissertation wurde am 21.02.2025 bei der Technischen Universität München eingereicht und durch die TUM School of Engineering and Design am 15.07.2025 angenommen.

To my grandfather.

† 08.02.2024

Contents

1 Introduction **1**
- 1.1 State of the Art . . . 1
- 1.2 Research at the Chair of Non-destructive Testing . . . 2
- 1.3 Motivation . . . 2
- 1.4 Thesis Outline . . . 3

2 Materials and Methods **5**
- 2.1 Test Facility . . . 5
  - 2.1.1 Wind Turbine . . . 5
  - 2.1.2 Measurement System . . . 6
  - 2.1.3 Data Pre-Processing . . . 8
  - 2.1.4 Tower Motion Module (TMM) . . . 10
- 2.2 Digital Representations of Wind Turbines . . . 12
  - 2.2.1 Real-Time Environment . . . 14
  - 2.2.2 Frequency Analysis . . . 15
  - 2.2.3 Remaining Useful Life . . . 17
- 2.3 Data Analysis Techniques . . . 19
  - 2.3.1 Kalman Filter . . . 19
  - 2.3.2 Machine Learning . . . 20

3 Additional Experiment: Tower Displacement Estimation **29**
- 3.1 Background . . . 29
- 3.2 Design of Experiments . . . 29
- 3.3 Results . . . 33

4 Discussion **41**

5 Conclusion **45**

References **51**

List of Related Publications **63**
- Publication 1 . . . 64
- Publication 2 . . . 77
- Publication 3 . . . 86

List of Supervised Student Projects **99**

List of Abbreviations **103**

List of Symbols **105**

List of Figures **107**

List of Tables **109**

Abstract

Damages to wind turbine supporting structures are associated with high costs and long downtime. Structural Health Monitoring of wind turbines is key for structural integrity and maintenance planning, avoiding cost-intensive damage-induced downtime. It also enables End-of-Life repowering and lifetime extension decisions, thus increasing return on investment and sustainability. The application of Structural Health Monitoring is not a standard industry practice and associated with cost-intensive installations and is often not economically feasible. Wind turbine operators generally do not benefit from using such systems, although prevention of rare but severe failure would be possible.

This work identifies critical damages and their influences on structural response, investigates possible low-cost measurement solutions to assess tower top displacement using optimal state estimation and deep learning, and outlines well-established methods and techniques that can be applied. Based on the main findings of the associated publications, a stand-alone measurement system - *Tower Motion Module* - is developed enabling data fusion of acceleration and Real-Time Kinematic through Kalman Filter and Long Short-Term Memory neural networks to estimate the tower top displacement. Highly accurate static and dynamic displacement of the tower top opens new possibilities for enhanced structural analysis, anomaly detection, damage detection and localization, and remaining useful life estimation, thus making it a valuable tool for Structural Health Monitoring of wind turbines.

1 Introduction

Wind energy has an increasing share in the renewable energy sector. Structural integrity and safety play an important role in the operation of wind turbines, especially in urban areas where space around the turbines is limited, and human beings can be around. Therefore, it is key to monitor the structure's health and integrity.

1.1 State of the Art

Failure case investigations on wind turbines have been widely conducted by numerous researchers. Ma et al. (2019) investigates WT tower collapse cases between 2000 and 2016 and found, that unexpected extreme wind load levels combined with human errors such as poor quality control, faulty construction, erroneous operation, and improper maintenance are the most common failure mechanisms. Alonso-Martinez et al. (2019) evaluates the flange connection of a collapsed WT with FEM and concludes poor quality control and design issues as the causes of the incident. Bolt pre-tension associated with a tower collapse is investigated from Liu and Ishihara (2015), where it was found, that a loss of pre-tension of bolts reduces the fatigue life to a magnitude of days. Chou et al. (2019) found in a study, that most structural failure cases occur due to buckling followed by bolt fractions and occur during high wind speeds above 60 m/s. Damages leading to a collapse of the WT might be detectable in advance. Notable changes in the structural response of simulated damage were investigated in a study from Dai et al. (2017). The approaching collapse significantly influenced static and dynamic tower top displacement. To detect damages and plan maintenance, NDT and SHM are applied to WT towers in various forms and applications.

Civera and Surace (2022) investigates NDTs for CM and SHM of WT. In Civera (2021), vibration-based structural analysis and damage detection methods are discussed. Furthermore, data acquisition techniques and signal processing including mode decomposition, cleansing for ML, feature extraction, and numerical modeling techniques are analyzed and interpreted. Other approaches than vibration- and SCADA-based methods such as VI, optical methods, LDV, video spectroscopy, IRT for blade inspection (Traphan et al., 2018), RT, Microwave and Terahertz Testing, Electromagnetic Testing, AE of tendons and anchor rods (Grosse et al., 2022, Raith et al., 2015), UT, oil monitoring, and static strain measurements are investigated in more detail. Olabi et al. (2021) studies possible failure modes for wind turbine towers such as fatigue, cracks, and corrosion. Also, earthquakes, unanticipated soil volatility, and unwarranted tainting of the foundation are considered in the investigation. Tower displacement is investigated from Feliciano et al. (2018) and provides a general analytical model for tower displacement with *openFAST*. Grundkötter and Melbert (2021) models blade deflection and needs tower displacement as an input for the model. Currently, tower displacement is estimated utilizing a digital twin using tower deflection Euler angles and tower mode shapes. Quaternion rotation and tower displacement thereby serve as input for all subsequent reconstruction algorithms to consider tower dynamics always. Khazaee et al. (2022) carried out a feasibility study to detect structural faults in blades by analyzing tower vibration. Virtual acceleration and displacement sensors are utilized in a modeled onshore WT using the NREL FAST code and emphasizing the remarkable potential for detecting structural faults. The dissertation from Puruncajas Maza (2024) elaborates on vibration-based SHM methods to detect fault and damage in WT and finds, that vibration-based methods do not require a dense network of sensors. A very limited number can accurately identify dynamic properties of large and complex structures. García Márquez and Peinado Gonzalo (2021) provides a Comprehensive Review of Artificial Intelligence and wind energy. Oliveira et al. (2018) presents a vibration-based long-term monitoring and Eigenfrequency & damping analysis as a key element of SHM on WT. Hernandez-Estrada et al. (2021) states, that little structural analysis is conducted at WT and investigates tools for structural analysis.

1.2 Research at the Chair of Non-destructive Testing

The former projects *Mistralwind* and *IM Wind* established a comprehensive measurement system in a WT in northern Bavaria, refined and extended up to now. A detailed insight into the previously utilized techniques and applied analysis tools can be found in Botz (2022), Botz et al. (2017a,b), Geiss and Grosse (2018), Rupfle et al. (2023). The current measurement setup consists of a central DAQ and distributed sensors across the tower. The sensors are acceleration, strain, seismometer, temperature, tilt, an RTK sensor, two independent systems of wireless acceleration sensors, and within the course of this work established TMM, that represents a stand-alone solution to predict tower top displacement based on data fusion of acceleration and RTK measurements through KF and ANN. Previous research also utilized DIC (Botz et al., 2017a, Ozbek and Rixen, 2013) and LDV (Botz, 2022, Dai et al., 2015, Dilek et al., 2019, Zieger et al., 2020) techniques for displacement and vibration measurements.

1.3 Motivation

Vibration-based SHM for wind turbines is a widely studied field, yet many research groups continue to face significant challenges in measuring displacement rather than acceleration. Despite these difficulties, displacement data offers notable advantages over acceleration, particularly as a direct input for modeling processes and to enhance RUL estimation. This work aims to provide a measurement and data analysis solution that helps assess the tower displacement under varying loads, and proposes methods to detect anomalies under operation, and determines the RUL of the structure with well-established methods like Bayesian models (Nguyen and Goulet, 2019), independent component analysis (Liu et al., 2020), Gaussian mixture model (Hasegawa et al., 2020), or by predictive POD curves (Mendler et al., 2023), and rainflow-counting & S/N-curves (Botz, 2022, Botz et al., 2020, Loew et al., 2019, Osterminski and Gehlen, 2018).

In this study, structural response as a result of damage to supporting structures is investigated. Methods to determine tower top displacement based on other measured data are developed. A low-cost hardware platform and the corresponding software environment is developed and further experiments on data fusion techniques using KF and LSTM are investigated.

1.4 Thesis Outline

The *Materials and Methods* section provides an overview of the test facility and the measurement techniques applied during the long-term monitoring projects, including the developed *Tower Motion Module*. Additionally, the pre-processing involved in the monitoring system is detailed.
Section *Digital Representations of Wind Turbines* outlines the general concept of digital representations of wind turbines and details the proposed concept and the contributions of this work. Furthermore, foundations of data processing techniques involving KF and ANN (especially LSTM) are provided in section *Data Analysis Techniques*. Section Additional Experiment: Tower Displacement Estimation introduces the DL based approach for estimating the tower displacement, rounding up the main findings of the associated publications. The *Discussion* sets the investigations into context, outlines the potentials and limitations of the results, and suggests further methods and techniques utilizing the results of this work.

This cumulative dissertation is based on the three peer-reviewed first-author publications:

- "Investigation of the Measurability of Selected Damage to Supporting Structures of Wind Turbines" (Publication 1)
- "Development of a Minimalistic Smart Sensor System for Motion Measurement of Wind Turbine Towers" (Publication 2)
- "Operational Sensor Adjustment for Structural Health Monitoring Systems in Wind Turbines using Machine Learning" (Publication 3)

and the additional related publications:

- "Soft real-time framework for Structural Health Monitoring of wind turbine supporting structures" (Publication 4)
- "Analysis of Icing on Wind Turbines by Combined Wireless and Wired Acceleration Sensor Monitoring" (Publication 5)

The TMM presented in this thesis emerged directly from the findings of this research and from the practical challenges encountered. It was implemented on commercially available hardware components. The overall concept, system architecture, and complete software implementation were conceived and developed exclusively by the author and constitute the author's exclusive intellectual property. A corresponding patent application covering the TMM has been filed with the European Patent Office.

2 Materials and Methods

This work adheres to the terminology from Rooij (2001) that proposes general notations and conventions that have become common practice within the considered disciplines and the reporting standards for machine learning based science proposed from Kapoor et al. (2023)

2.1 Test Facility

This section presents the test facility provided and the measurement system developed. The initial *Mistralwind* (2015 - 2018) project was realized as a collaborative project from TUM Chair of Non-destructive Testing, Chair of Materials Science and Testing, Chair of Structural Analysis, IABG mbH, Siemens AG, Sachverständigenbüro Otto Lutz, and Max Bögl Wind AG, and installed the initial measurement setup on a WT, described in Section 2.1.1. The consortium carried out important work on the development of a high-definition FEM and model updating through measured modal properties. During the project, the measurement setup was refined and extended. The subsequent project *IM Wind* (2019 - 2021), also carried out as a collaborative project with TUM Chair of Non-destructive Testing, Chair of Structural Analysis, ASC GmbH, ClockworkX GmbH, ASC GmbH, and elunic AG, further extended the measurement system and refined data analysis. The measurements are continued up to the submission of this work. Both projects were financed from the *German Federal Ministry for Economic Affairs and Climate Action.*

The section elaborates on the WT, the complete measurement system, however, some sensors are redundant and not utilized in the experiments conducted for this work. Furthermore, the data pre-processing which ensures unified and synchronized data sets is detailed and the TMM is introduced.

2.1.1 Wind Turbine

The test facility utilized within the scope of this work is an onshore horizontal axis conventional three-bladed upwind WT located in northern Bavaria. It consists of a hybrid tower construction with a hub height of 142.5 m. An overview of its structural components is provided in Figure 2.1.

The tower's lower segment, extending 78.8 m, is constructed from pre-stressed concrete, with internal tendons ensuring the pre-stressing. Above this, the tower consists of two steel sections, making up the remaining 60 m. The diameter reduces from 8.8 m at the base to 2.7 m at the top. This hybrid design and progressive narrowing of the tower significantly reduces the tower's stiffness as it ascends leading to a higher deflection at the tower top and almost negligible deflections in the lower parts of the tower.

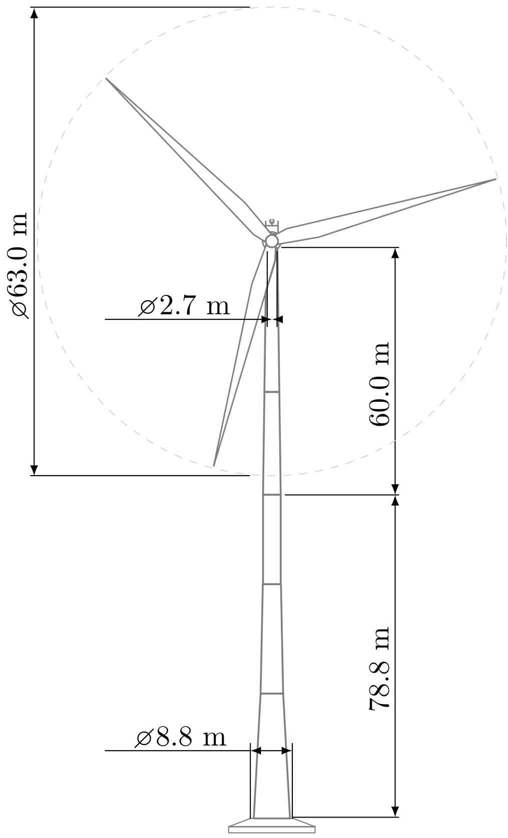

Figure 2.1: Hybrid tower construction dimensions. Hub-height: 142.5 m with 2.0 m basement height and 1.7 m distance from tower top to hub.

The WT has a nominal power of 3.0 MW and a maximum rotor speed of 15.5 rev/min with a variable rotor speed due to direct drive technology. Its cut-in wind speed is 4.0 m/s and the rated power is achieved at 12.5 m/s. The cut-out wind speed is set to 25.0 m/s. The turbine was established in 2014 and has been equipped with a long-term monitoring system since 2016.

2.1.2 Measurement System

The initial measurement system installed in 2016 consisted of a distributed data acquisition system on three levels of the turbine: The main data acquisition including an edge computer on the ground level, and two further data acquisition units at a height of 80.8 m and 138.9 m, respectively. Its main focus is measuring acceleration on four levels: 47.5 m, 80.9 m, 114.9 m, and 139.0 m. The system was also equipped with strain gauges at two levels: 82.4 m and 139.0 m, and a fiber-optical strain measurement system at ground level (3.5 m). An additional triaxial seismometer was installed at the ground level (2.0 m), and temperature sensors were placed at 2.0 m, 80.9 m, and 139.0 m to compensate for temperature influences. In a test phase, an RTK sensor was placed on top of the nacelle (147.0 m), and optic measurements using DIC were taken (Botz et al., 2016, 2017a, Geiss et al., 2017).

As an extension, the measurement system was equipped with a redundant acceleration sensor at a height of 139.0 m and two biaxial tilt sensors at 80.9 m and 139.0 m, respectively. Furthermore, the developed TMM (see Section 2.1.4), consisting of a triaxial acceleration sensor, a temperature sensor, and a permanently installed RTK module was installed to gather long-term measurements (see Publication 1).

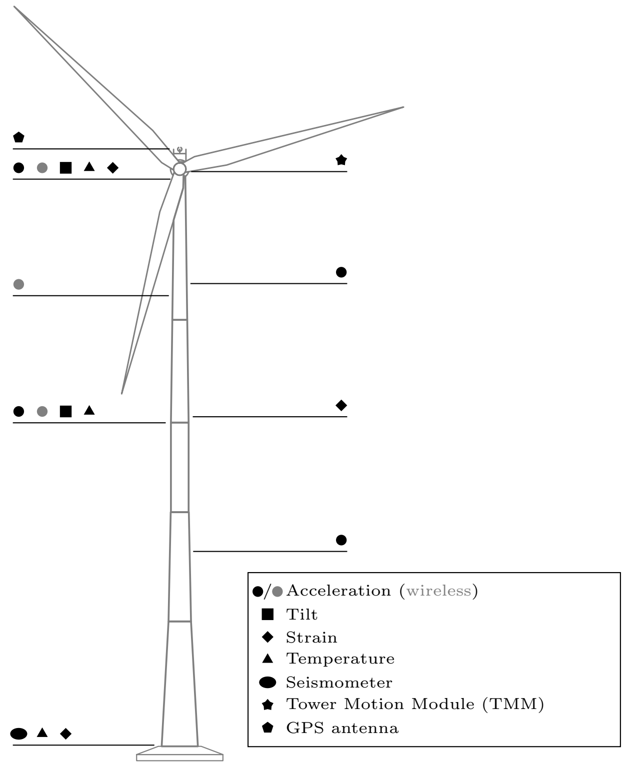

Figure 2.2: Measurement setup at the test facility. Corresponding heights from bottom to top: 2.0 m, 47.5 m, 80,9 m, 82.4 m, 112.0 m, 114.9 m, 139.0 m, 142.0 m, 147.0 m.

In addition, long-term monitoring using wireless acceleration sensors is carried out at the test facility. Two independent systems are installed, each providing sensors at heights of 80.9 m, 112.0 m, and 139.0 m (Wondra et al., 2016, 2023).

Figure 2.2 summarizes the comprehensive test setup, installed in the course of the projects. The sensors are connected via UART to a central data acquisition at ground level or connected to the tower-wide network via Wi-Fi or Ethernet.

The systems can be subdivided into independent measurement systems. The main part of the sensors is connected to the central data acquisition at ground level. The TMM works independently in the nacelle and the wireless systems are distributed over the tower height. Table 2.1 summarizes the characterizations of the measurement systems.

In addition to the installed measurement system, the wind turbine operator provides access to SCADA data. Usually, SCADA data are provided in 10-minute or 15-minute average values. For research purposes, access to high-resolution SCADA data with an acquisition rate of up to 1 Hz is provided by the operator. In addition, the WT is equipped with a blade monitoring system consisting of acceleration sensors inside the blades. The operator provides the processed data from this enclosed system, including rotor blade condition data and ice alerts.

System	Sample Rate	Sensor	Height	Model
DAQ	100 Hz	Strain	139.0 m	TML FCA-6-11-1L
		Acceleration	139.0 m	PCB 3713B112G
		Acceleration	139.0 m	triaxial
		Tilt	139.0 m	ASC TS92V5-015-5A
		Temperature	139.0 m	Heraeus W-SZK
		Acceleration	114.9 m	ASC EQ-321-003-20A
		Acceleration	114.9 m	PCB 3713B112G
		Acceleration	80.9 m	PCB 3713B112G
		Strain	82.4 m	TML FCA-6-11-1L
		Tilt	80.9 m	ASC TS91V5-090-6A
		Temperature	80.9 m	Heraeus W-SZK
		Acceleration	47.5 m	MMF KB12VD
		Seismometer	2.0 m	Lennartz 3Dlite MkIII
		Temperature	2.0 m	Heraeus W-SZK
		Strain[1]	3.5 m	fos4Strain expert nSens
TMM	10 Hz	Acceleration	142.0 m	Analog Devices ADXL355
		Temperature	142.0 m	Analog Devices ADXL355
		RTK	147.0 m	EMLID Reach M+
NI myRIO	62.5 Hz	Acceleration	139.0 m	Analog Devices ADXL355
		Acceleration	107.0 m	Analog Devices ADXL355
		Acceleration	80.9 m	Analog Devices ADXL355
NeoMote[2]	31.25 Hz	Acceleration	139.0 m	Analog Devices ADXL355
		Acceleration	107.0 m	Analog Devices ADXL355
		Acceleration	80.9 m	Analog Devices ADXL355
Blade	$\approx$ 0.016 Hz	HMU[3]		
SCADA	max. 1 Hz	Power		
		Rot. Speed		
		Pitch Angle		
		Yaw Angle		
		Env. Temperature		
		Wind Speed		
		Status		

[1] Fiber optical system
[2] Low power wireless sensing network developed by Prof. Steven D. Glaser (UC Berkeley) and Metronome Systems LLC
[3] Hub Measurement Unit (proprietary name)

Table 2.1: Summary of the installed and used measurement systems and their corresponding sample rate and sensor including height and specification, if applicable.

2.1.3 Data Pre-Processing

The data pre-processing applied to the measurement systems consists of several stages, including low pass filtering & arithmetic mean, implementation of sensor characteristics, sensor offset correction, coordinate transformation to either tower fixed coordinates or nacelle fixed coordinates, and conversion into a unified format.

Low-pass filtering and arithmetic mean: to exclude high-frequency influences from grid frequencies and other sources, the 100 Hz data of the main DAQ is initially filtered with a Butterworth low-pass filter of 2$^{\mathrm{nd}}$ order and 3 dB frequency of 20 Hz. In addition, the arithmetic mean of a sample count of 2 is built to smooth the measurements.

Furthermore, acceleration data of TMM and *Wireless 1 & 2* directly incorporates an analog, low-pass, antialiasing filter of 31.25 Hz, derived from the sample rate of the ADXL355z sensing elements. This effectively ensures the exclusion of high-frequency noise such as grid frequency interference.

Sensor characteristics: The sensor characteristics of each sensor are saved in a database and applied to the measurements directly within the measurement system before further pre-processing. All sensor data output is linearized using Equation 2.1, where Y is the sensor data in the desired unit, S_{sens} is the sensitivity of the sensor, U_m is the measured voltage output from the sensor, and U_o is the offset voltage derived from sensor calibration data sheets.

$$Y = S_{sens} \times (U_m - U_o) \tag{2.1}$$

Seismometer data are processed independently as of its nonlinearity according to Haney et al. (2012).

Sensor offset and orientation: In addition to the sensor data offset determined in calibration data sheets, each sensor is subjected to an additional offset due to non-planar installation and aging processes. Publication 1 introduces a method (RSA) to determine sensor offsets and sensor orientations utilizing an initiated 360-degree rotation of the nacelle. Due to the rotor and nacelle weight, a quasi-static tower bending in the rotor direction is introduced. This leads to a sinusoidal sensor data output that fits a parameterized sinusoidal model to determine adjustment values.
Publication 3 further refines this method and introduces two data-driven methods USA and BSA to determine sensor offsets more accurately by fully excluding external remaining wind influences.

Coordinate transformation: Coordinate transformations between different systems, such as S, T, and N, are essential for the analysis of measured data. This transformation utilizes Tait-Bryan angles, employing intrinsic sequence $X - Y' - Z''$. The rotation matrices R for each axis are defined in Equations 2.2 - 2.4.

Rotation around the X-axis (α):

$$R_X(\alpha) = \begin{bmatrix} 1 & 0 & 0 \\ 0 & \cos\alpha & -\sin\alpha \\ 0 & \sin\alpha & \cos\alpha \end{bmatrix} \tag{2.2}$$

Rotation around the Y'-axis (β):

$$R'_Y(\beta) = \begin{bmatrix} \cos\beta & 0 & \sin\beta \\ 0 & 1 & 0 \\ -\sin\beta & 0 & \cos\beta \end{bmatrix} \tag{2.3}$$

Rotation around the Z"-axis (γ):

$$R''_Z(\gamma) = \begin{bmatrix} \cos\gamma & -\sin\gamma & 0 \\ \sin\gamma & \cos\gamma & 0 \\ 0 & 0 & 1 \end{bmatrix} \tag{2.4}$$

The combined rotation matrix from S to T coordinates ($R_{S\to T}$) is given by the product of these rotations:

$$R_{S\to T} = R_{Z''}(\gamma) \cdot R_{Y'}(\beta) \cdot R_X(\alpha) \tag{2.5}$$

Similarly, the rotation matrix from S to N coordinates ($R_{S\to N}$) is an additional rotation around the Z-axis (θ) of the tower:

$$R_{S\to N} = R_{S\to T} \cdot R_Z(\theta) \tag{2.6}$$

where $R_Z(\theta)$ is the rotation matrix for the Z-axis rotation in the tower-fixed coordinates.

Conversion to unified data format: To unify the data format and appearance to simplify access to measured data, a common file system was chosen where measured data from all systems is converted to. MathWorks® binary *MAT* files, based on the *HDF5* format and commonly used in MATLAB®, were chosen for their widespread compatibility across multiple programming languages. Additionally, a script was developed to convert data into parquet files, a format optimized for DL applications (Ivanov and Pergolesi, 2020).

To address data imbalances from differing sampling rates, source files are downsampled or upsampled with specifically developed interpolation schemes to a standardized sampling rate of 10 Hz, adequate to resolve natural frequencies, including the second bending frequency range (1.06 to 1.10 Hz) of the WT tower.

2.1.4 Tower Motion Module (TMM)

To provide a measurement solution to effectively estimate the static and dynamic tower displacement, a low-cost system was developed and introduced in Publication 2. An established system prototype is shown in Figure 2.3.

Figure 2.3: Tower Motion Module prototype consisting of a single-board computer, an acceleration element, an RTK module with antenna connector, and external memory for data logging.

The prototype is based on a single board computer, gathering the measurement data and providing a data logging platform and an online data streaming solution. The system acquires measurement data from an RTK module, a triaxial acceleration sensor including a temperature measurement element, and a socket to receive online SCADA data. The counterpart that provides online SCADA data over MQTT was developed in the student project *"Automation of a script for downloading SCADA data via a programming interface"* (Mosiej, 2023) and can either run as a cloud service or within the measurement system itself.
A more detailed conceptual visualization of the TMM can be found in Publication 2, Figure 1.

Reliability analysis of dynamic displacement measurement using RTK is provided in *Publication 1*. Botz (2022)[1] states that quasi-static deflection during the downtime of 7 hours at high wind speeds shows values above 5 m, which would make them unsuitable for this purpose. The standard deviation (σ) of the solution and the quality flag (q, i.e., the *RTKLIB* (Takasu and Yasuda, 2009) solution-status indicator: `fix` (integer ambiguity resolved), `float` (integer ambiguity unresolved), or `single` (single point positioning)) were not further specified in this analysis. An investigation of long-term stability was carried out in preparation for the experiment. As the wind turbine tower shows highly dynamic motion and a mass-induced direction-dependent static displacement, statements on statistics would only be possible with data from several years.

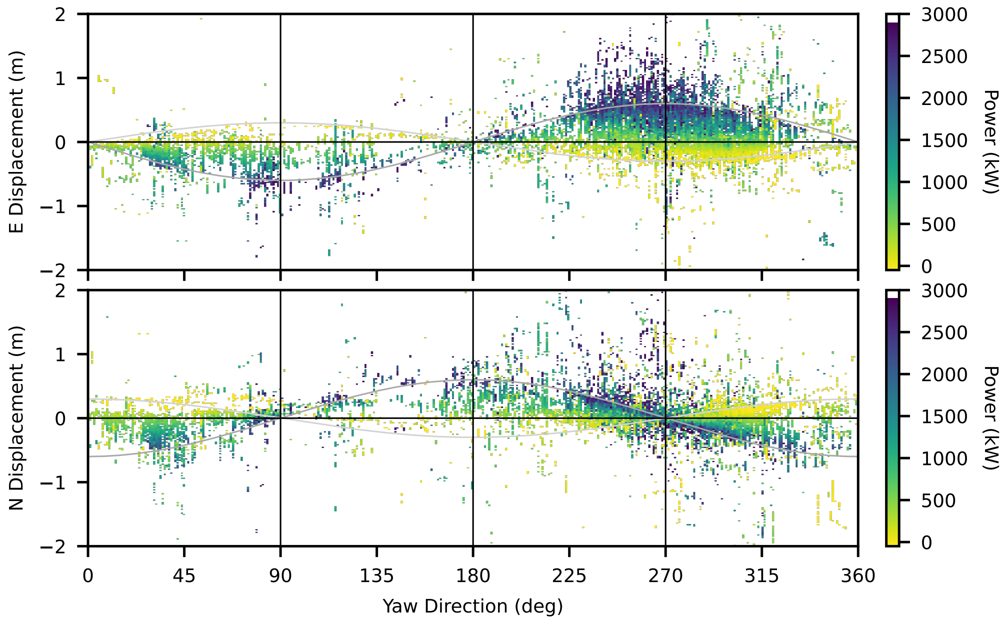

Figure 2.4: Binned RTK data of a long-term observation (2023-11-17 to 2024-02-14) that fulfills the quality requirements over the yaw angle (to true north).
Quality requirements: $q = 1\texttt{fixed}$, $\sigma_E < 0.020\,\mathrm{m}$, $\sigma_N < 0.020\,\mathrm{m}$, $AR > 3$
Binning resolution: $\Phi = 1\,\mathrm{deg}$, $E = 0.02\,\mathrm{m}$

[1]Page 114, Figure 5.10

Figure 2.4 shows the RTK position over the yaw angle of data from the period of 2023-11-17 to 2024-02-14. The data is limited to 14.31 % of the data points that fulfill a standard deviation in E and N direction of $\sigma < 0.020\,\mathrm{m}$, an AR of $AR > 3$, and a fixed solution status.

As investigated in *Publication 2*, mass-induced forces bend the tower into fore direction at downtime. The thrust force compensates for the mass-induced tower bending at a power output of $P \approx 450\,\mathrm{kW}$. This means, the tower displacement equals zero. Furthermore, the thrust-induced bending at rated power output is around three times higher than the mass-induced tower bending, thus bending the tower into aft direction.

The predominant wind direction is concentrated around a yaw angle of $\Phi = 270 \pm 45\,\mathrm{deg}$ (south-west to north-west direction). Derived from *Publication 3*, it can be assumed that the thrust force-induced displacement at rated power is about double the (rotor and nacelle) mass-induced displacement acting in the opposite direction at the downtime of the wind turbine. The sinusoidal line plots indicate the expected displacement behavior at downtime (light gray) and rated power (dark gray) over the yaw angle (Φ) of an ideal system not affected by turbulent winds. The displacement in the E direction for a yaw angle of $\Phi = 270\,\mathrm{deg}$ (corresponding to the west direction) from true north concentrates on the sinusoidal plots for rated power output and idle. Values in between show predominantly power output values of partial load. Deviations from the expected behavior can be explained through various factors. In addition to the dynamic displacement (due to turbulence and wind gradients) and yaw misalignment, acquisition issues from multipath reflections (Smyrnaios et al., 2013) originating from the rotor, and ionospheric (Wielgosz et al., 2005) and tropospheric (Ahn et al., 2006) bias influence the precision of the gathered data.

Two distinct data fusion and prediction methods have been developed to address the challenges associated with outliers, uncertainties, and missing RTK data. A fusing algorithm using an optimal state estimator (KF) to fuse RTK and acceleration data is developed in *Publication 2* and an approach using an ANN (LSTM) to train on acceleration and SCADA data for predicting tower displacement is detailed in Chapter 3. Both methods are designed to integrate with the TMM system, providing robust estimation capabilities for both static and dynamic tower displacements.

2.2 Digital Representations of Wind Turbines

Digital representations of physical systems such as WT, often categorized as DM, DS, and DT, vary in complexity and functionality (Kritzinger et al., 2018). However, there's a lack of consensus across different domains about these terminologies, with some literature on DM or DS incorrectly referred to as DT (Singh et al., 2021).

This dissertation specifically addresses the development of a DS, characterized by its automated, unidirectional data flow from the WT to its digital counterpart. In contrast, a DT features a bidirectional data exchange where the digital entity can influence the WT, forming a closed-loop system (Sepasgozar, 2021).

The concept of DT, along with DS and DM, has gained attraction across various industries, from manufacturing (Pal et al., 2022) to cultural heritage (Hassanien et al., 2022). It represents the convergence of human knowledge and objective world information (Wang and Liu, 2021). Typically, a DT features a digital representation of a physical system, updated in real-time (Rabczuk and Bathe, 2023), and is common in applications like structural life prediction and system verification & validation (Wagg et al., 2020).

A DS has to handle multiple timescales (Rabczuk and Bathe, 2023). In wind turbine applications, data acquisition periods range from milliseconds (e.g., acceleration data) to seconds (e.g., SCADA data). Additionally, long-term features like Eigenfrequencies may display trends over several months or years, as evidenced in studies on monopile-supported offshore wind turbines (Abdullahi et al., 2022).

The central platform is a key component within the framework of a DS. Development needs and specifications of such platforms vary between applications and may impose risks. Their development requires constant effort to improve, update, and consolidate the platform. (Crespi et al., 2023)

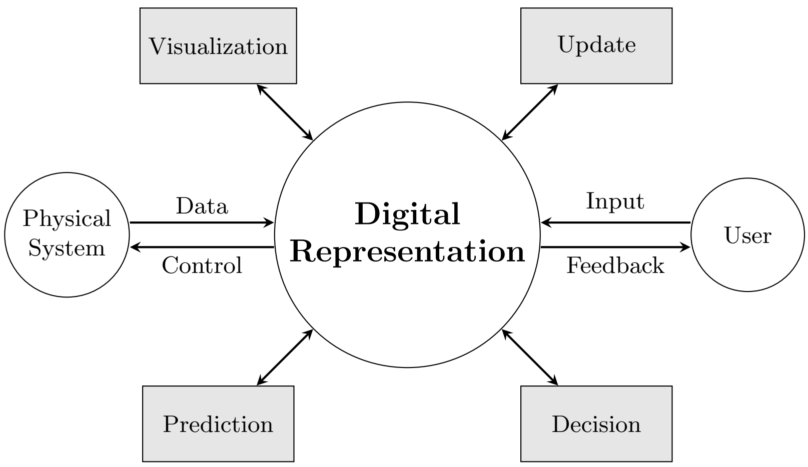

Figure 2.5: Concept of a Digital Representation and its interaction with the physical system and the user. The degree of automation (manual/automatic) of the *Data* and *Control* flows distinguishes between the terminology DM, DS, and DT. Representation contains four potential modules derived from Rabczuk and Bathe (2023).

A data-based framework as illustrated in Figure 2.5, can be subdivided into three principal components: *Digital Representation*, *Physical System*, and *User*. The *Physical System*, equipped with measurement technologies, supplies data to the *Digital Representation* and, in turn, can be managed or controlled based on a return channel from the *Digital Representation*. The degree of automation of the flow hereby distinguishes between the terminology DM, DS, and DT. The *User* interacts with the system by obtaining feedback from the *Digital Representation* and providing inputs, such as manual inspection data.

This framework presents four key modules derived from Rabczuk and Bathe (2023). The predictive module is responsible for monitoring changes in the system and forecasting future conditions for tasks like maintenance planning or estimating the RUL. The update module ensures that the *Digital Representation* remains aligned with the physical model, particularly through model updating techniques as suggested in Geiss et al. (2017). Additionally, a decision module aids in providing recommendations and supporting decision-making processes, as outlined from Granacher et al. (2022).

This section introduces aspects relevant to developing digital representations of physical systems, fundamental for anomaly detection, predictive maintenance, and estimating RUL. It presents a framework designed to handle and analyze various data types, ranging from numerical to textual inputs across multiple time scales. The analysis of natural frequencies for anomaly detection is proposed, and methods to estimate tower displacement are discussed to determine tower loads, enabling accurate RUL estimation.

2.2.1 Real-Time Environment

To enhance the monitoring capabilities of the test facility, a soft real-time environment was developed, as outlined in Rupfle and Grosse (2023). In contrast to hard real-time systems, soft real-time environments are not deterministic and response time is a statistical criteria. This environments foundation was partly laid through the initiatives in the student projects *"Implementation of a Real-Time Data Analysis Environment in MATLAB/Simulink"* (Zimmermann, 2022) by testing MQTT connection environments and *"Design and Implementation of a Central Data Collection and Visualization System for a Multi Sensor Wind Turbine Monitoring System"* (Theisen, 2023) by implementing a NoSQL database being able to accomodate data from various sources.

Central to the proposed environment is a network of two MQTT brokers, which bridge the local and cloud-based systems, as depicted in Figure 2.6.

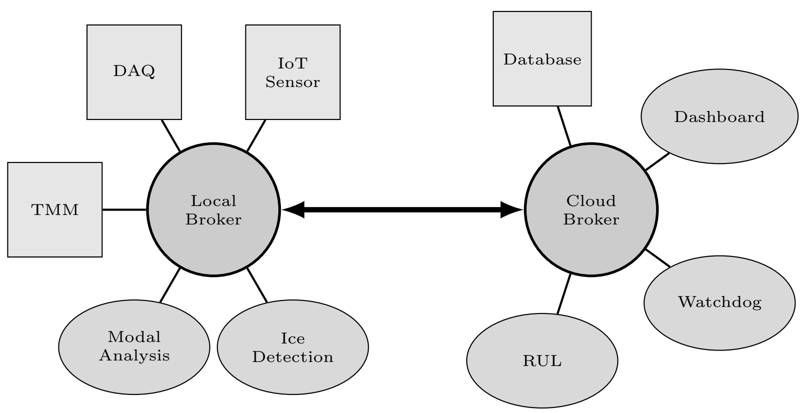

Figure 2.6: Soft real-time environment for SHM systems, showing a local and cloud infrastructure interconnected via an MQTT bridge. Devices are represented as rectangles and modules as ellipses.

The MQTT infrastructure functions as a bridged connection, enabling the exchange of topics between local and cloud systems. This architecture permits autonomous operation and offers robust security through advanced authentication and encryption techniques. Additionally, its design incorporates measures to handle connection interruptions, thereby preventing data loss by queuing messages at both the client and broker ends. Reconnection ensures straightforward feeding of queued messages into NoSQL databases. The local infrastructure consists of devices such as TMM, DAQ, and IoT sensors, along with modules for *Modal Analysis* and *Ice Detection*. These components are essential for supporting real-time and time-sensitive applications. In contrast, the cloud infrastructure is responsible for housing databases and undertaking computationally intensive, non-time-critical tasks. These tasks include RUL evaluation, neural network training, and other machine learning activities. Additionally, the cloud setup provides a *Dashboard* as a user interface and incorporates a *Watchdog* mechanism for malfunction detection.

2.2.2 Frequency Analysis

In order to obtain the frequency spectrum of a time series, DFT can be employed. Particularly its computationally efficient version, the FFT, to analyze the frequency content of the signals under investigation. The FFT is a widely used algorithm for computing the DFT introduced by Cooley and Tukey (1965), which decomposes a signal into its constituent frequencies, transforming it from the time domain to the frequency domain. A further investigation of decomposition techniques for SHM is carried out in Civera and Surace (2021). The FFT significantly reduces the number of computations required for the DFT, particularly for signals with a large number of samples, by exploiting symmetries in the DFT formula. This efficiency gain is achieved through a divide-and-conquer approach that recursively breaks down the DFT into smaller DFTs. The standard DFT is defined in Equation 2.7, where $X[k]$ represents the frequency spectrum of the signal, $x[n]$ is the original time-domain signal, N denotes the total number of samples, k is the frequency index ranging from 0 to $N-1$, and i is the imaginary unit.

$$X[k] = \sum_{n=0}^{N-1} x[n] \cdot e^{-\frac{2\pi i}{N}kn} \tag{2.7}$$

Prior to the Fourier transformation, a bandpass filter shall be applied to the data. This filtering process aims to retain signal components within a specific frequency range while attenuating components outside this range, thus excluding both static (low-frequency) and high-frequency parts of the signal. The bandpass filter used in this study is a Butterworth filter, known for its maximally flat frequency response in the passband. Detailed information on the filter's implementation and its Python realization can be found in the work of Esakkirajan et al. (2024). Its order and cut-off frequencies characterize the Butterworth filter design. The order of the filter determines the steepness of the filter's response around the cut-off frequency. A higher order results in a steeper roll-off. The filter's transfer function in the continuous-time domain for a n^{th} order low-pass filter is given by Equation 2.8, where $H(s)$ represents the filter's transfer function, s is the complex frequency variable, ω_c is the cut-off frequency, and n is the filter's order. This design is adapted for the bandpass filter implementation by specifying both a lower and upper cut-off frequency to form the desired passband. The resulting filter effectively allows signal components within these frequency boundaries to pass while attenuating those outside the range.

$$H(s) = \frac{1}{1 + \left(\frac{s}{\omega_c}\right)^{2n}} \tag{2.8}$$

Before performing Fourier analysis, the data is processed with a bandpass filter. This step is important for focusing on the frequency range of interest by suppressing undesired low and high-frequency signals. This study uses a Butterworth bandpass filter, renowned for its flat amplitude response within the passband.

The Butterworth filter is designed based on a specific order, which dictates the roll-off rate around the cut-off frequencies. The steeper the roll-off, the higher the filter's order. The continuous-time transfer function of a low-pass Butterworth filter of order n is expressed in Equation 2.9, where $H(s)$ is the filter's transfer function, s denotes the complex frequency, ω_0 is the cut-off frequency, and n represents the filter's order. This study adapts the Butterworth design to form a bandpass filter with defined lower and upper frequency limits. Notably, a zero-phase filtering approach is implemented, which ensures no phase distortion in the signal, a significant aspect when analyzing time series data. This approach processes the data forward and then backward, doubling the filter's order while preserving the phase characteristics of the signal.

$$H(s) = \frac{1}{\sqrt{1 + \left(\frac{s}{\omega_0}\right)^{2n}}} \tag{2.9}$$

Additionally, a Tukey window can be applied to the signal before executing the FFT. The purpose of windowing is to minimize the spectral leakage effect, which occurs when a signal is not periodic within the observation window. The Hamming window, a type of tapered window, is particularly effective in reducing this leakage due to its specific characteristics (Harris, 1978) and used in this study. In Equation 2.10, $w(n)$ denotes the window function value at the n-th sample for a signal with N samples. The parameter α influences the taper ratio. The function is defined in segments: the first for the initial taper, the second for the flat middle section, and the third for the ending taper. This minimizes spectral leakage in the FFT.

$$w(n) = \begin{cases} \frac{1}{2}\left[1 + \cos\left(\pi\left[\frac{2n}{\alpha(N-1)} - 1\right]\right)\right], & \text{for } 0 \leq n \leq \frac{\alpha(N-1)}{2} \\ 1, & \text{for } \frac{\alpha(N-1)}{2} < n \leq N - \frac{\alpha(N-1)}{2} \\ \frac{1}{2}\left[1 + \cos\left(\pi\left[\frac{2n}{\alpha(N-1)} - \frac{2}{\alpha} + 1\right]\right)\right], & \text{for } N - \frac{\alpha(N-1)}{2} < n \leq N - 1 \end{cases} \tag{2.10}$$

After windowing, the FFT is performed to obtain the PSD of the filtered and windowed signals. The PSD provides insight into the power distribution of the signal across different frequencies, enabling a more nuanced understanding of its frequency-domain characteristics. Provided that natural frequencies are distinguishable, simple peak-picking algorithms can identify them.

Comprehensive methods for the detailed identification of modal properties such as natural frequencies, damping ratios, and mode shapes are achieved through modal analysis techniques like EMA and OMA. While EMA is a powerful tool when controlled excitation under laboratory conditions is possible, OMA, including techniques like SSI, extends modal analysis capabilities to situations where EMA is not practical. EMA utilizes external excitation, but analysis of a WT under operational conditions does not allow for controlled excitation. Therefore, OMA is more feasible for this purpose. Over time, various algorithms have been developed within OMA, each offering progressively more accurate and computationally efficient solutions. Apart from peak picking, frequency and time domain decomposition techniques are available. Furthermore, methods such as auto-regressive moving average and SSI are both computationally intensive and mathematically complex, providing advanced solutions for modal identification (Zahid et al., 2020). A general introduction to OMA techniques and their application can be found in Brincker and Ventura (2015).

In the dynamic analysis of wind turbines, understanding the mode shapes, or the modal parameters, is essential for assessing the structural integrity and performance under varying operational conditions. A typical approach to characterize these mode shapes involves the application of TDD techniques on acceleration data collected from the wind turbine, particularly at the tower top. The wind turbine structure resembles a cantilever beam, so its dynamic behavior can be effectively modeled using Euler-Bernoulli beam theory.

The TDD method can employ time-series data of acceleration or displacement at the turbine's tower top and further measurements distributed over the height to extract the modal parameters. By analyzing these data, particularly through specific techniques such as the SSI, it is possible to deduce the mode shapes of the structure. The accuracy of SSI, especially for extracting mode shapes from structures, is generally enhanced with multiple measurements from different positions. The mode shape can then be expressed with Equation 2.11, where $\psi_n(x)$ denotes the n-th mode shape, expressing the structural deflection at position x. The modal coefficients a_{ni} represent the contribution of each basis function $\phi_i(x)$. In other words, $\psi_n(x)$ is written as a weighted sum of known basis functions $\phi_i(x)$. The weights a_{ni} indicate how much each basis function contributes to the n-th mode shape.

$$\psi_n(x) = \sum_{i=1}^{N} a_{ni}\phi_i(x) \tag{2.11}$$

2.2.3 Remaining Useful Life

The RUL represents the predicted duration over which a component can continue to perform its intended function before failure occurs due to fatigue. By analyzing the cumulative fatigue damage calculated using methods like the Palmgren-Miner rule and understanding the stress cycles experienced by the structure, it is possible to predict the remaining service life. This enables the implementation of proactive maintenance strategies, and allows for informed decisions on lifetime extension, repowering and dismantling of a WT.

Based on the previously covered mode shape determination, a way to calculate the stress (σ) for the use in determining the fatigue of a structure may look as follows. The displacement, curvature, and bending moments along the tower height can be expressed as described by Branlard et al. (2020). The deflection δ of the wind turbine tower in the horizontal directions x and y (which can correspond to sensor axes, East/North, or FA/SS) at a specific height z and time t can be represented by the sum of the tower shape functions scaled by the respective degrees of freedom. This relationship is mathematically expressed as:

$$\delta_x(z,t) = \sum_i q_{xt,i}(t)\tau_i(z), \tag{2.12}$$

$$\delta_y(z,t) = \sum_i q_{yt,i}(t)\tau_i(z). \tag{2.13}$$

The curvature of the tower, denoted by κ, is derived by differentiating the deflection δ twice with respect to z. This results in the following expressions for curvatures in the x and y directions:

$$\kappa_x(z,t) = \sum_i q_{xt,i}(t)\frac{d^2\tau_i}{dz^2}(z), \tag{2.14}$$

$$\kappa_y(z,t) = \sum_i q_{yt,i}(t)\frac{d^2\tau_i}{dz^2}(z). \tag{2.15}$$

Utilizing Euler beam theory, the bending moments along the tower height are computed from the curvatures. For a given tower cross-section with bending stiffness $EI(z)$, the bending moments in the y and x directions are:

$$M_y(z,t) = EI(z)\kappa_x(z,t), \tag{2.16}$$

$$M_x(z,t) = EI(z)\kappa_y(z,t). \tag{2.17}$$

The stress at a point on the wind turbine tower due to bending can be calculated with Equation 2.18, where $\sigma(z,t)$ is the bending stress, $M(z,t)$ is the bending moment, $c(z)$ is the distance from the neutral axis to the outermost fiber, and $I(z)$ is the moment of inertia of the cross-section. Partial safety factors for load and materials can be applied according to Germanischer Lloyd (2007) and Musial and Butterfield (1997).

$$\sigma(z,t) = \frac{M(z,t)\cdot c(z)}{I(z)} \tag{2.18}$$

The stress-time history of the wind turbine structure is processed using a rainflow counting algorithm as per IEC (2019) guidelines. This analysis identifies stress cycles for fatigue evaluation, applying each to an S-N curve to estimate the number of cycles until failure at varying stress ranges. Cumulative fatigue damage is then assessed using the Palmgren-Miner rule (Miner, 1945) with Equation 2.19, where D quantifies the cumulative fatigue damage in a material subjected to cyclic loading. In this rule, n_i represents the number of stress cycles, and N_i the corresponding number of cycles to failure, typically derived from S-N curves.

$$D = \sum_{i=1}^{n} \frac{n_i}{N_i} \tag{2.19}$$

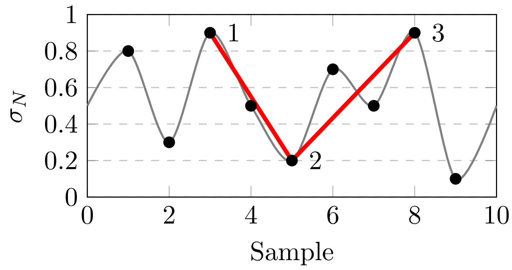

Figure 2.7: Conceptual visualization of rainflow counting.

RUL can then be derived from D by simply extrapolating the current rate of damage accumulation to predict when a critical damage level will be reached. Figure 2.7 shows a conceptual illustration of the rainflow counting method. It shows samples of normalized stress and visualizes a derived load cycle spanning from point 1 over point 2 to point 3, marking the upper and lower limits and omitting changes below a threshold. Various counting algorithms exist that only differ from each other in small aspects. Lee et al. (2014) provides more insight into different techniques and applications.

A detailed linear damage accumulation hypothesis description can be found in Bracke (2024). Further literature on the implementation is provided in Grosse (2012), Osterminski and Gehlen (2018), Loew et al. (2019), Botz et al. (2020), and Botz (2022).

2.3 Data Analysis Techniques

This section discusses the applied data processing and analysis techniques. It focuses on two methodologies that extend beyond the discussed content of the published papers: the KF and ML for sensor data adjustment and displacement estimation. The KF is of great importance for enhancing the accuracy of dynamic system measurements, while ML, through regression and ANN, is key for the prediction of tower top displacement. These methods are central to the discussed approaches, providing a comprehensive framework for system state prediction.

2.3.1 Kalman Filter

The KF is an effective algorithm for estimating a system's state based on one or more inputs introduced by Kalman (1960). The filter operates in two phases: prediction and update. In the prediction phase, it forecasts the current state and its uncertainty. Upon receiving new measurements, the KF updates these predictions through a weighted average, prioritizing more certain estimates. This recursive nature makes the KF highly effective in real-time and dynamic systems.

The KF equations used for the prediction step are described in Equations 2.20, where $\hat{\mathbf{x}}_{k|k-1}$ is the predicted state at time step k given measurements up to time step $(k-1)$, $\mathbf{A}$ is the state transition matrix that represents the dynamics of the system, $\hat{\mathbf{x}}_{k-1|k-1}$ is the previous state estimate at time step $(k-1)$, $\mathbf{B}$ is the control input matrix (if applicable) that relates the control input $\mathbf{u}_k$ to the state, $\mathbf{P}_{k|k-1}$ is the predicted state covariance at time step k given measurements up to time step $(k-1)$, $\mathbf{P}_{k-1|k-1}$ is the previous state covariance at time step $(k-1)$, and $\mathbf{Q}$ is the process noise covariance matrix, containing the standard deviation of each individual measurement and no cross axis covariance, that represents the uncertainty in the prediction step.

Prediction Equations:

$$\begin{aligned}\hat{\mathbf{x}}_{k|k-1} &= \mathbf{A}\hat{\mathbf{x}}_{k-1|k-1} + \mathbf{B}\mathbf{u}_k \\ \mathbf{P}_{k|k-1} &= \mathbf{A}\mathbf{P}_{k-1|k-1}\mathbf{A}^T + \mathbf{Q}\end{aligned} \tag{2.20}$$

The update equations are described in Equations 2.21, where $\mathbf{y}_k$ is the innovation or measurement residual, which represents the difference between the actual measurement $\mathbf{z}_k$ and the predicted measurement based on the state estimate, $\mathbf{H}$ is the measurement matrix that maps the state space to the measurement space, $\mathbf{S}_k$ is the innovation covariance, which represents the uncertainty in the measurement, $\mathbf{R}_k$ is the measurement noise covariance matrix that represents the uncertainty in the measurement, $\mathbf{K}_k$ is the Kalman gain, which determines the amount of correction applied to the predicted state based on the measurement, $\hat{\mathbf{x}}_{k|k}$ is the updated state estimate at time step k given the latest measurement, $\mathbf{P}_{k|k}$ represents the updated state covariance at time step k, and $\mathbf{I}$ is the identity matrix.

Update Equations:

$$\begin{aligned}\mathbf{y}_k &= \mathbf{z}_k - \mathbf{H}\hat{\mathbf{x}}_{k|k-1} \\ \mathbf{S}_k &= \mathbf{H}\mathbf{P}_{k|k-1}\mathbf{H}^T + \mathbf{R}_k \\ \mathbf{K}_k &= \mathbf{P}_{k|k-1}\mathbf{H}^T\mathbf{S}_k^{-1} \\ \hat{\mathbf{x}}_{k|k} &= \hat{\mathbf{x}}_{k|k-1} + \mathbf{K}_k\mathbf{y}_k \\ \mathbf{P}_{k|k} &= (I - \mathbf{K}_k\mathbf{H})\mathbf{P}_{k|k-1}\end{aligned} \tag{2.21}$$

For more comprehensive insights into the practical application of a KF, see Welch et al. (1995). The application of the KF in the context of this study is further elaborated in Publication 2, where it is used to enhance the accuracy of the developed measurement system.

2.3.2 Machine Learning

AI, especially ML is already gaining significant influence in almost all areas of modern life. It has emerged in retail, education, autonomous vehicles, healthcare, agriculture, social media, and chatbots (Sharma and Garg, 2021), to name just a few applications. It is present in our daily lives and interacts with humankind. A pioneer work in AI proposes the simplest neuron model (MCP) to represent Boolean functions (McCulloch and Pitts, 1943).

In the field of wind energy, diverse AI applications can be found. Maron et al. (2022) studies highlights of AI for anomaly detection in SCADA data, focusing on evaluating key components like generators, converters, and gearboxes. This method is effective in correlating operational data with potential faults and downtimes. Barahona et al. (2017) offers another approach, deriving operating regimes from SCADA data and establishing a framework for accumulating damage over time. Furthermore, Marugán et al. (2018) categorizes AI applications in wind energy into four major areas: forecasting, design optimization, fault detection, and control optimization, with a strong emphasis on wind forecasting and fault detection in components like gearboxes and blades. Movsessian et al. (2021) introduces a novel ANN-based method for damage detection in wind turbine blades, employing continuous monitoring and advanced mathematical techniques for assessing vibrational data.

In fact, AI consist of many more sub-fields than just ANN. Usually, AI is described with the subdomains ML, DL, and NLP (Mahalle et al., 2023). Often, CV and robotics are also added as subdomains (Grillmeyer, 1998), although they might fit into the other existing subdomains.

Figure 2.8 illustrates the subdomains and their relation to each other. ML and NLP can be seen as subdomains of AI, whereas DL can be a subdomain of either ML or NLP.

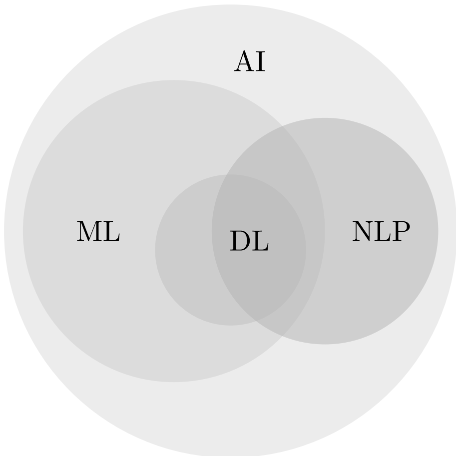

Figure 2.8: Building blocks ML, DL, and NLP of AI.

Building a model based on observations as a hypothesis about the real-world and software to solve problems is called ML (Russell and Norvig, 2021) and forms the basis of the hype around AI (Jung, 2022). Machine learning can be subdivided into Supervised, Unsupervised, and Reinforcement Learning (Greiner et al., 2022). Supervised and Unsupervised Learning form one big discipline, while Reinforcement Learning can be seen as a separate field, and represents a continual learning problem where an agent's goal is to efficiently maximize a long term reward (Abel et al., 2023) rather than relying on a static dataset with labeled or unlabeled data, where the focus is on learning from pre-existing data rather than actively interacting with an environment to form its learning process. Due to major advances in fields like DL, Reinforcement Learning is getting less attention and its application focuses on very specific fields such as industrial processes and energy management systems. In industry, its applications include operational decision-making in industrial processes (Liu et al., 2024), and additive manufacturing, as discussed by Mohammadi et al. (2024) and Parisi et al. (2023). In relation to energy management systems, Reinforcement Learning is used in managing battery electric vehicles (He et al., 2024), improving energy efficiency in

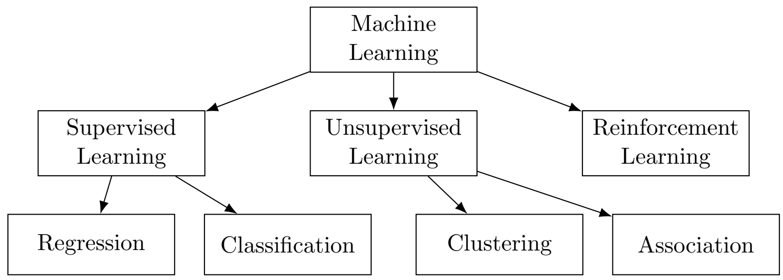

Figure 2.9: Overview of ML concepts and applications.

buildings (Kang et al., 2024), and enhancing smart city infrastructures (Ordouei et al., 2024).

Figure 2.9 illustrates ML, the subdomains, and selected methods. Mixed forms of concepts and methods also exist. Very common Supervised Learning techniques are regression algorithms, where a function is approximated, and classifications, where a data point label is predicted. On the other side, clustering, where unlabeled data is put together, and associations, where relationships between features shall be discovered, are widespread techniques used in unsupervised learning. Another widespread field of ML is formed by ANNs, which simulates the mechanism of learning in biological organisms (Aggarwal, 2023). This section focuses on methods used throughout this work to understand the theory behind the applied techniques. It will provide fundamentals of regression algorithms of different characterizations (linear and polynomial), but also a special form of ANN, the LSTM, will be introduced in more detail.

Regression:

In ML, regression is a central element across various methods. A regression function aims to correspond to the mean of a dependent variable based on one or more independent variables and explains the relationship between inputs and outputs (Sammut, 2017). The simplest form of regression represents a linear regression that explains a linear relationship between the independent variable x and the dependent variable Y. The univariate linear regression is given in Equation 2.22, where β_0 represents the intercept and β_1 represents the slope, respectively. ε represents the error term of the dependent variable Y.

$$\hat{Y}_i = \beta_0 + \beta_1 x_i + \varepsilon_i, \quad i = 1, \ldots, n \tag{2.22}$$

To fit non-linear models, a polynomial regression (a special form of multiple linear regression) can be performed, where the polynomial degree has to be chosen to prevent both under- and overfitting. Equation 2.23 represents the generalized polynomial regression function, where β_0 represents the intercept, β_i describes the coefficients, and ε represents the error term.

$$\hat{Y}_i = \beta_0 + \sum_{i=1}^{n} \beta_i x_i^i + \varepsilon_i \tag{2.23}$$

A good representation of the fit of a regression model is given by the SSE, as described in Equation 2.24 (Phillips, 2021), where minimized values stand for a good fit.

$$SSE = \sum_{i=1}^{n} (Y_i - \hat{Y}_i)^2 \tag{2.24}$$

A very commonly used method to minimize the SSE for both linear and polynomial regression which estimates the regression model parameters is the OLS. The corresponding coefficient estimates in regression can be represented as Equation 2.25 shows.

$$\hat{\beta} = (\mathbf{X}^T \mathbf{X})^{-1} \mathbf{X}^T Y \tag{2.25}$$

Here, $\hat{\beta}$ denotes the vector of estimated coefficients, $\mathbf{X}$ is the matrix of input data, and Y is the vector of observed values.

Artificial Neural Networks:

ANNs are fundamental to the field of machine learning. They are computational models inspired by the human brain's structure and function. At their core, neural networks consist of layers of interconnected nodes, or *neurons*, each performing simple computations. A neuron consists of an input, weight, bias, and an activation function. The most common types of neurons are perceptron and sigmoid neurons. (Calin, 2020c) A single-layer neural network is considered the simplest form and provides a clear illustration of the neural network concept. It can be understood as a linear regression model under a certain light. This network comprises an input layer and an output layer without any hidden layers, making it suitable for modeling linear relationships between inputs and outputs (Bishop and Bishop, 2024).

The model takes a set of input features $x = \{x_1, x_2, ..., x_n\}$, and each feature is associated with a weight $w = \{w_1, w_2, ..., w_n\}$. The output Y is then computed as a weighted sum of the inputs, often with an added bias term b, as shown in Equation 2.26:

$$Y = \sum_{i=1}^{n} w_i x_i + b \tag{2.26}$$

The network *learns* by adjusting the weights w and bias b to minimize the difference between the predicted output and the actual values, typically using a loss function (see Section 2.3.2) like MSE or MAE and an optimization algorithm (see Section 2.3.2) such as SGD or Adam. A visualized representation of the single neutron representing a linear regression model is depicted in Figure 2.10, where the inputs for weight w and bias b are illustrated on the left and the output Y is illustrated on the right side.

Simple single-layer neural networks lay the foundation for more complex architectures. Multilayer networks, or deep neural networks, extend this concept by introducing one or more hidden layers between the input and output layers. Each layer consists of neurons that apply non-linear transformations to the inputs, enabling the network to learn more complex, non-linear relationships (Goodfellow

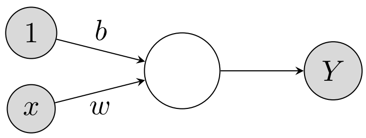

Figure 2.10: Single neuron expressing a linear regression model ($i = 1$).

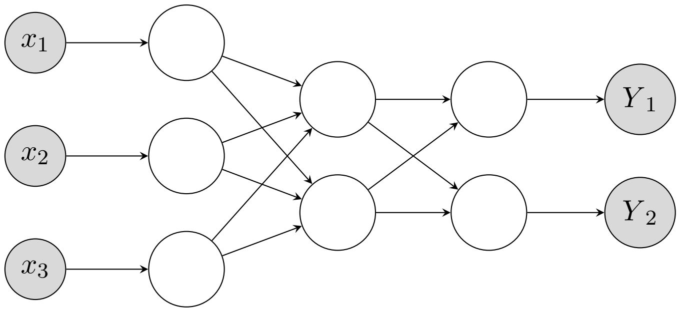

Figure 2.11: Basic structure of a multi-layer neural network with three input features, two network outputs, and one hidden layer.

et al., 2016). The evolution from single-layer to multi-layer networks allows significant advancement in the machine learning field for developing sophisticated models capable of tackling a wide range of complex tasks such as image recognition and natural language processing (LeCun et al., 2015). A multi-layer neural network is represented in Figure 2.11, where x_1, x_2, and x_3 represent the input for the input layer and Y_1 and Y_2 represent the output of the output layer. The hidden layer interconnects the input and output layers.

A typical multi-layer neural network processes the input through successive layers, with the output of one layer serving as the input for the next. Layers are denoted with superscripts (l), where the index represents the layer the synapse feds into (Calin, 2020c). The output of the final layer forms the overall output of the network. The computation in a two-layer neural network (one hidden layer) is represented with the Equations 2.27, where H represents the output of the hidden layer, f is the activation function, $w^{(1)}$ and $w^{(2)}$ are the weights for the hidden layer and output layer, respectively, and $b^{(1)}$ and $b^{(2)}$ are the biases for the hidden layer and output layer, respectively.

$$\begin{aligned} H &= f(w^{(1)}x + b^{(1)}) \\ Y &= w^{(2)}H + b^{(2)} \end{aligned} \tag{2.27}$$

Further developed types of neural networks are RNN and LSTM.

RNN are a class of neural networks that are particularly effective in processing sequences of data. Unlike traditional feedforward neural networks, RNN have internal memory and can maintain information in *hidden* layers through loops, allowing them to exhibit temporal dynamic behavior. This makes RNN suitable for tasks where context and sequence matter, such as language modeling and speech recognition (Manaswi, 2018). One of the foundational works in the development of RNN, particularly regarding the training algorithms, especially describing backpropagation is published from Rumelhart et al. (1986). During backpropagation of long sequences, multiplication of many values significantly less than 1 or multiplication of many large values greater than 1 leads to vanishing or exploding gradients, causing the RNN to train very slowly (Manaswi, 2018). RNN therefore struggle to learn long-term memories (Zucchet and Orvieto, 2024).

LSTM networks are an extension of RNN designed to avoid the long-term dependency problem. They achieve this through a more complex internal structure in their hidden units, including components like input, output, and forget gates. These gates regulate the flow of information, making LSTM capable of learning which data to store, overwrite, or forget during processing. This characteristic enables LSTM to perform exceptionally well on tasks that require learning from long sequences of data, such as time series prediction or sequence generation. (Hochreiter and Schmidhuber, 1997)

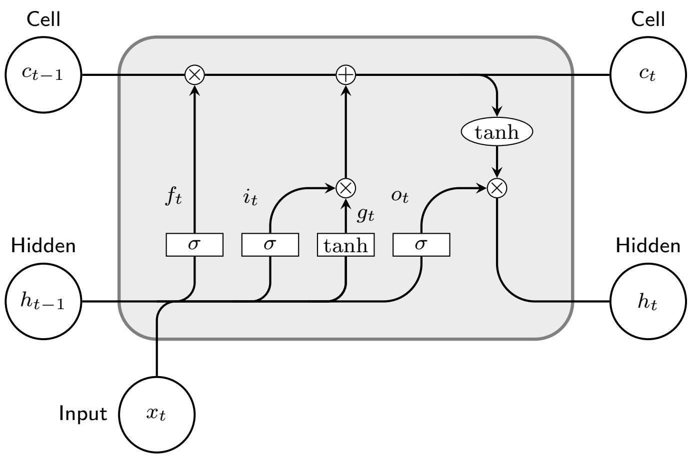

Figure 2.12: Simplified representation of an LSTM cell. Adapted from Sak et al. (2014) and Luo et al. (2021).

Equations 2.28 to 2.33 describe the functionality of an LSTM unit. The input gate i_t controls the flow of new information into the cell. Concurrently, the forget gate f_t regulates the extent to which a value remains in the cell. The cell gate g_t generates a vector of candidate values, providing potential updates to the cell state. This process allows the cell to store and manage both short-term and long-term information, represented by the cell state c_t. The output gate o_t influences the output activation of the LSTM cell. The hidden state h_t, is used for making predictions and is carried forward to the next time step. In these equations, the weights are symbolized by w, and the biases by b. The sigmoid activation function is denoted by σ, and the hyperbolic tangent activation function is represented by tanh. $\odot$ represents the element-wise product (Hadamard product). More information on activation functions can be found in detail by Goyal et al. (2020) and Calin (2020a).

$$i_t = \sigma(w_{ii}x_t + b_{ii} + w_{hi}h_{t-1} + b_{hi}) \tag{2.28}$$
$$f_t = \sigma(w_{if}x_t + b_{if} + w_{hf}h_{t-1} + b_{hf}) \tag{2.29}$$
$$g_t = \tanh(w_{ig}x_t + b_{ig} + w_{hg}h_{t-1} + b_{hg}) \tag{2.30}$$
$$o_t = \sigma(w_{io}x_t + b_{io} + w_{ho}h_{t-1} + b_{ho}) \tag{2.31}$$
$$c_t = f_t \odot c_{t-1} + i_t \odot g_t \tag{2.32}$$
$$h_t = o_t \odot \tanh(c_t) \tag{2.33}$$

Alongside the feed-forward prediction of the neural network, the training process in multi-layer networks involves backpropagation and gradient descent, allowing the network to adjust its weights and biases to minimize the loss function, improving prediction accuracy.

Loss Functions:

In ML, loss functions L, also known as cost functions, error functions, or objective functions J, play an important role in the training of models by quantifying the difference between the predicted values and observed values. In the training process, they provide a measure to optimize. A common loss function for regression tasks is the MSE, given by Equation 2.34, where Y_i is the observed value, $\hat{Y}_i$ is the prediction, and n is the number of samples.

Another common loss function is represented by the MAE, denoted in Equation 2.35, where the absolute value of $Y_i - \hat{Y}_i$ is summed up instead of the squared term in MSE. MAE is less sensitive to outliers as their weight less influences (Sewdien et al., 2020). For classification tasks, the CE loss, defined in Equation 2.36, where Y is the true class label and $\hat{Y}$ is the predicted probability of each class C, is widely used (Calin, 2020b).

$$L_{MSE}(Y, \hat{Y}) = \frac{1}{n}\sum_{i=1}^{n}(Y_i - \hat{Y}_i)^2 \tag{2.34}$$

$$L_{MAE}(Y, \hat{Y}) = \frac{1}{n}\sum_{i=1}^{n}|Y_i - \hat{Y}_i| \tag{2.35}$$

$$L_{CE}(Y, \hat{Y}) = -\sum_{c=1}^{C} Y_c \log(\hat{Y}_c) \tag{2.36}$$

The choice of the loss function is of high importance as it directly affects the model's ability to learn the underlying patterns in the data. A well-chosen loss function can lead to faster convergence and more accurate models. Furthermore, in complex scenarios such as deep learning, customized loss functions can be designed for specific data characteristics or the model's desired properties. Ehrig et al. (2020) introduces an asymmetric loss function used for predictive maintenance. This flexibility allows efficient training processes, adapting to different ML tasks.

Backpropagation:

The gradient of the loss function concerning the network's weights in neural network training can be computed using the fundamental backpropagation algorithm. It is essential for training feed-forward neural networks and more complex architectures like RNN and LSTM. Conceptually, backpropagation consists of a forward pass where input data is passed through the network to generate output, and a backward pass where the error (difference between predicted and actual output) is propagated back through the network to adjust the weights (Rumelhart et al., 1986).

The core of backpropagation is the chain rule used to compute the gradients in the repeated composition of functions (Aggarwal, 2023). For a neural network with layers denoted as $\mathcal{L}$, the gradient of the loss function E with respect to the weights $w^{(\mathcal{L})}$ in layer $\mathcal{L}$ is calculated as depicted in Equation 2.37.

$$\frac{\partial E}{\partial w^{(\mathcal{L})}} = \frac{\partial E}{\partial O^{(\mathcal{L})}} \cdot \frac{\partial O^{(\mathcal{L})}}{\partial w^{(\mathcal{L})}} \tag{2.37}$$

where $O^{(\mathcal{L})}$ represents the output of layer $\mathcal{L}$. The term $\frac{\partial E}{\partial O^{(\mathcal{L})}}$ represents the derivative of the error concerning the output, and $\frac{\partial O^{(\mathcal{L})}}{\partial w^{(\mathcal{L})}}$ is the derivative of the output concerning the weights. These derivatives are calculated for each layer, starting from the output layer and moving backward to the input layer.

By applying this algorithm iteratively and with a learning rate, the network learns to minimize the error, leading to improved model accuracy. The effectiveness of backpropagation in deep learning models, especially in conjunction with gradient descent optimization techniques, has been a significant factor in the advancements of neural network applications (Goodfellow et al., 2016).

Gradient Descent:

A first-order iterative optimization algorithm can be utilized for continuous functions instead of using OLS to minimize the SSE in a regression model. This method updates the parameters of a model, such as coefficients in regression or weights in ANN, by iteratively adjusting them in the opposite direction of the gradient of the cost function with respect to these parameters (Ruder, 2016).

$$\Theta_{i+1} = \Theta_i - \eta \nabla_{\Theta_i} J(\Theta_i) \tag{2.38}$$

In Equation 2.38, Θ denotes the model's parameters, η represents the learning rate, controlling the step size in the minimization process, and $\nabla_\Theta J(\Theta)$ signifies the gradient of the cost function J with respect to Θ. The learning rate η is crucial as it influences the convergence speed towards the minimum; a large rate may cause rapid convergence and potential overshooting, while a small rate may lead to a slow convergence process.

Gradient descent algorithms are available in various forms, such as Batch Gradient Descent, Stochastic Gradient Descent, and Mini-batch Gradient Descent. These differ in the amount of data used to calculate the gradient of J. Larger data sets significantly increase computational demands. Sequential algorithms like Stochastic Gradient Descent, which process one data point at a time, offer improved computational efficiency but can complicate convergence (Sammut, 2017). An enhanced variant, Mini-batch Gradient Descent, updates parameters for every n sample, striking a balance between computational efficiency and stable convergence. (Ruder, 2016)

Furthermore, the initialization of the parameter vector Θ plays a role in the convergence of Gradient Descent. Different initialization strategies can lead to varying optimization paths, influencing the speed and the quality of convergence to the optimal solution.

In this work, the computationally efficient algorithm *Adam* for non-stationary problems with very noisy and sparse gradients is used (Kingma and Ba, 2014).

3 Additional Experiment: Tower Displacement Estimation

The following experiment concludes the findings of Publication 1, Publication 2, and Publication 3. This work proposes an approach to estimate the tower top displacement by means of a trained LSTM network using either acceleration measurements and SCADA data or by using just one of the data sources to make it a more flexible solution. The training exclusively employs highly accurate RTK data, which accounts for approximately 10 to 20 % of the measured data, to ensure precise prediction. The aim is to evaluate whether the model can approximate displacement in scenarios where only low-quality data are available or where RTK measurements are missing, thereby demonstrating the potential for an RTK-independent method for tower displacement estimation.

3.1 Background

In Publication 1, the dynamic displacement of the wind turbine tower is investigated. Three different approaches of vibration-based displacement in the frequency domain, RTK data, and external forces based simulated displacement are compared. The result showed that the dynamic displacement's amplitude and phase align. This can be seen as a proof of concept for determining dynamic displacement using RTK data.

As shown by Botz (2022), RTK data strongly depend on the data quality and can underlie static displacement drifts over time. Usually, RTK data provide insight into the overall data quality with a fixed solution or a float solution status directly indicating the expected quality (Valente et al., 2020). Furthermore, the number of satellites available and the AR can be used to estimate the quality of the provided data. In addition, the standard deviation of the triangulation solution in three spatial directions is provided. Repeatability and static precision are essential for achieving accurate long-term RTK measurements and for training ANN, which requires large data sets. Several studies have addressed the accuracy of static RTK measurements. For instance, Baybura et al. (2019) report a difference of static measurements with a baseline of 10 km of 2.5 *cm*, while Gumilar et al. (2019) concludes an error accuracy of up to 0.8 *cm* for short baselines.

Currently deployed measurement techniques, such as LDV, are unsuitable for long-term monitoring, and methods like RTK lack the reliability required to monitor tower deflection permanently. The neural network trained on only high-accuracy RTK data shall close this gap in SHM of WT.

3.2 Design of Experiments

The data set used for training spans 90 days, from 2023-11-17 to 2024-02-14. This period includes measurements under both partial and nominal load operations.

During the season from October to April in Germany, capacity factors typically exceed 0.3 and are approximately twice as high as those observed during the rest of the year, as reported by Kaspar et al. (2019). As illustrated in Figure 3.1 (a), the wind distribution during this time shows a predominant wind direction from southwest to northwest. The wind rose categorizes wind speeds into five groups: below cut-in speed [0.0 : 4.0), partial load with rotor speed below rated speed [4.0 : 8.0), partial load at rated rotor speed [8.0 : 12.0), at rated power output [12.0 : 25.0), and above cut-out speed > 25. To achieve optimal training results, it is essential to ensure that the data set includes all possible operational states to capture the full variability of the system's behavior. Additionally, fine-tuning and balancing the data set to address any imbalances or biases can significantly enhance the model's performance and generalizability.

Additionally, Figure 3.1 (b) presents a bar plot showing the distribution of operational states during the period. *Idle* (0.58 %) refers to times when the wind speed was below the cut-in threshold, *Partial Load* (64.66 %) to periods with power output below the rated power, and *Rated Power* (23.32 %) to operation at rated power output. Downtime, where the cut-in wind speed is exceeded but the turbine is not operating, accounted for only 0.44 % of the time and is considered negligible. Component protection, occurring at wind speeds above 25 m/s, was not observed in the data set.

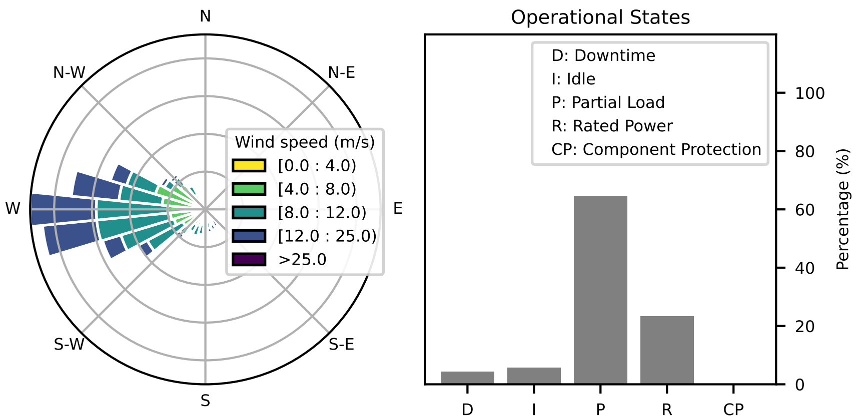

(a) (b)

Figure 3.1: Wind rose and operational states of the wind turbine during period 2023-11-17 to 2024-02-14.
(a) Wind rose to show wind speeds categorized into five groups: below cut-in speed [0.0 : 4.0), partial load with rotor speed below rated speed [4.0 : 8.0), partial load at rated rotor speed [8.0 : 12.0), at rated power output [12.0 : 25.0), and above cut-out speed > 25.
(b) Operational states of the wind turbine in the data set: Downtime: 0.44 %, Idle: 0.58 %, Partial Load: 64.66 %, Rated Power: 23.32 %, Component Protection: 0.00 %.

A comprehensive data pipeline needs to be developed to prepare the training data. Figure 3.2 shows a simplified chart that depicts the way from raw data to training data.

Data from the DAQ and the SCADA system is unified by resampling to a unified sampling rate of 10 Hz. For the DAQ data, a low pass filtering and the sensor characteristics are applied before the resampling. Parts of the data treatment

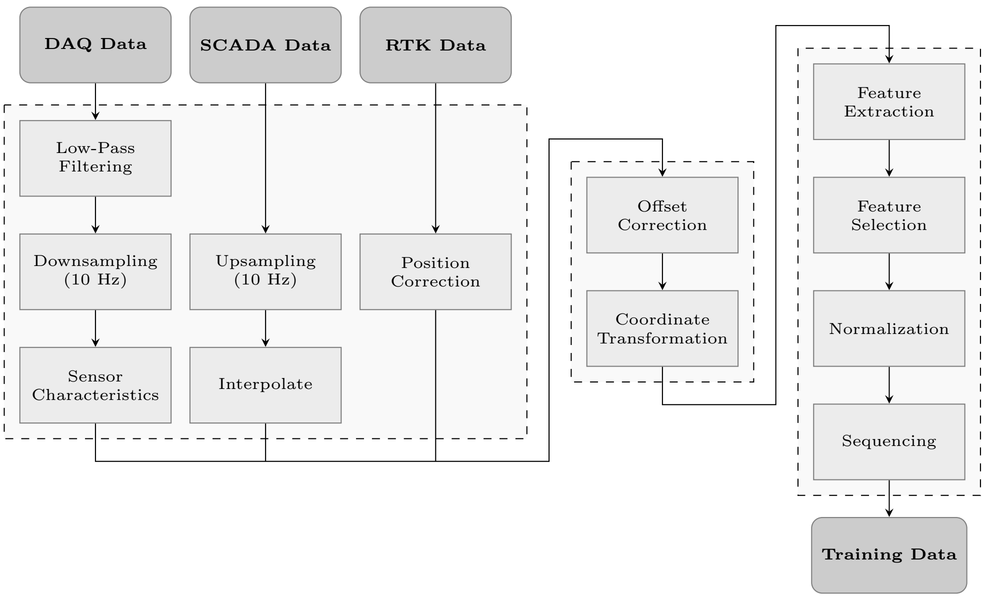

Figure 3.2: Data pipeline from measured data of various sources to sequential training input (Left: Creation of unified format; Center: Sensor-specific data pre-processing; Right: Preparation of training data).

were developed in the student project *"Merging of measurement data from various Structural Health Monitoring systems for further analysis"* (Horváth, 2023). The SCADA data is interpolated after resampling to fill the corresponding *NaN*[1] values that can't be handled in the training data. Interpolation schemes reach from simple linear interpolation over cubic splines (Qiangqiang et al., 2014) to fixed-gradient backward interpolation (Rupfle et al., 2022). Afterward, sensor-specific data pre-processing is performed where offset adjustments and coordinate transformations are applied. This process is based on the data derived from the BSA and RSA, developed in Publication 3. The final preparation of the training data consists of several steps to form the necessary high-quality sequential data. To produce accurate training results, directional features of the measured data are extracted. Vector decomposition of the power output and wind speed data (P and v, denoted as x; Yaw angle denoted as ϕ) is performed using Equations 3.1.

$$\begin{aligned} x_E &= x \cdot \sin(\phi) \\ x_N &= x \cdot \cos(\phi) \end{aligned} \tag{3.1}$$

To ensure efficient training and to reduce the presence of outliers, a feature selection process detailed in Table 3.1 is developed. An important factor in determining the accuracy of RTK data is the quality flag (q), where 1 indicates a fixed solution status, where the integer ambiguity is properly resolved. Further insights into the quality flag used in *RTKLIB* can be found in the work of Takasu and Yasuda (2009). Equally important are the standard deviations (σ) of triangulation in the East (E), North (N), and Up (U) spatial directions. Additionally, the AOD (t_{AOD}) is constrained to guarantee consistent correction data from the base station. The AR is also widely used as a quality indicator in

[1] *NaN* (Not a Number) represents undefined or unrepresentable numerical values, often used to indicate missing data in numerical computations.

GNSS applications (Teunissen and Verhagen, 2008). The displacement (s) limits are set to exclude implausible values. For SCADA data, the power output (P), wind speed (v_w), changes in yaw angle ($\Delta\phi$), and pitch angle (λ) are confined to ranges typical of normal operational conditions. Similarly, acceleration data from DAQ is restricted to values observed under standard operational scenarios. In summary, the selected *Min* and *Max* values ensure both the proper operation of the system and the exclusion of data of poor quality. The use of poor quality data or the use of data with errors would have a negative impact on the training result.

Feature / Label	Unit	Min	Max
q	–	1	1
σ_E	m	0	0.02
σ_N	m	0	0.02
σ_U	m	0	0.03
t_{AOD}	s	0	5.0
AR	–	3	999.0
P	kW	0	3000
v	m/s	0	30
λ	deg	-2	90
$\Delta\phi$	deg/s	-0.6	0.6
a_E	m/s^2	-1	1
a_N	m/s^2	-1	1
s_E	m	-1.5	1.5
s_N	m	-1.5	1.5

Table 3.1: Feature selection thresholds for LSTM training data.

Normalization of data is essential for training machine learning models. It prevents biases in features with large value ranges compared to those with smaller scales (Asesh, 2022). Normalization ensures equal importance for each variable in the model's learning process. Efficient training of models also depends on data normalization. Scaling data to a similar range accelerates the training process (Nayak et al., 2013). A common approach is to scale features to fit within a $[-1, 1]$ range.

$$x' = 2 \times \frac{x - x_{\min}}{x_{\max} - x_{\min}} - 1 \tag{3.2}$$

In Equation 3.2, x represents the original feature value. The terms $x_{\min}$ and $x_{\max}$ are the minimum and maximum values of the feature. The result, x', is the normalized value. For features like power output and wind speed, normalization limits are set symmetrically around zero. Table 3.2 lists the minimum and maximum values used for normalizing key features and labels according to 3.2.

Feature/Label	Unit	Min Value	Max Value
P_E	kW	-3000	3000
v_E	m/s	-30	30
a_E	m/s^2	-1	1
s_E	m	-1.5	1.5

Table 3.2: Min and Max values for normalization of features & labels.

In the sequencing process depicted in Figure 3.2, the data set undergoes feature selection, resulting in gaps. The data set is segmented into consecutive, high-quality data chunks to address this. Each segment is then independently transformed into sequential input for the LSTM network. Only segments longer than the predefined sequence length, either 40, 70, or 100 samples, are used for sequencing. This criterion ensures uniform sequence sizes, which is important for the model's consistency and performance. Segments that do not meet this length requirement are excluded, as the LSTM network require data of identical sequence length for training

Three models using acceleration data, SCADA data, and both acceleration and SCADA data are employed. Due to the highly imbalanced wind direction distribution, the models are trained and evaluated using only east-west-directional data. The specific features and labels used in each model are outlined in Table 3.3.

Model	**Features**	**Label**
ACC-only	a_E	s_E
SCADA-only	P_E, v_E	s_E
ACC+SCADA	a_E, P_E, v_E	s_E

Table 3.3: Employed models and corresponding features & labels.

Regarding the LSTM model's specifications, various network configurations were tested to optimize training outcomes. The models were trained with different numbers of hidden layers (ranging from 1 to 3) and varying hidden layer sizes (12, 25, and 75 units). Additionally, the models were trained with varying sequence lengths to investigate the impact of long-term dependencies on training efficacy. This approach aims to determine the optimal network architecture and data input length for accurate and efficient model performance. Each model and network configuration is trained for 200 epochs to ensure convergence for all models and to maintain consistency, although networks with smaller hidden sizes tend to converge much faster than models with larger hidden sizes. The models are trained with a batch size of 64, that was found to offer the smallest trade-off between computational efficiency and prevention of overfitting. Note that different batch sizes might produce the same results. Batch size shall be determined experimentally before training. The learning rate is set to $\eta = 0.0005$ with a scheduler applying a reduction factor 0.6 at epochs 10, 20, 40, 75, 100, and 150, allowing the models to converge to minima.

The test data set consists of 9 days of (2024-02-15 to 2024-02-23) RTK quality requirements are met in 17.95 % of the period. The data sets wind distribution and operational state distribution are depicted in Figure 3.3. A proper length of the test data set of 10% of the training data ensures test data to provide a wide variety of operational states.

3.3 Results

To optimize the LSTM network architecture, the three different model configurations *ACC+SCADA*, *ACC*, and *SCADA* were tested with different hidden size of 75, 25, and 12 units. A comparison of the loss per trained epoch is visualized in Figure 3.4 and indicates the overall performance of the trained models. All models are trained 200 epochs to ensure comparability between each other and to minimize training anomalies such as sudden loss drop, overfitting, plateaus, or turning points.

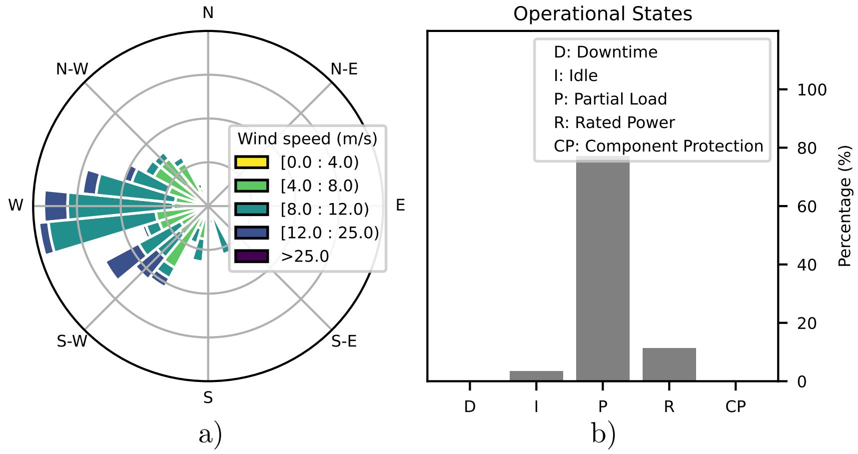

Figure 3.3: Wind rose and operational states of the wind turbine during period 2023-02-15 to 2024-02-23.
a) Wind rose to show wind speeds categorized into five groups: below cut-in speed [0.0 : 4.0), partial load with rotor speed below rated speed [4.0 : 8.0), partial load at rated rotor speed [8.0 : 12.0), at rated power output [12.0 : 25.0), and above cut-out speed > 25.
b) Operational states of the wind turbine in the data set: Downtime: 0.02 %, Idle: 3.55 %, Partial Load: 77.13 %, Rated Power: 14.42 %, Component Protection: 0.00 %.

It can be observed that, in general, the loss of the *ACC+SCADA* model outperforms the *ACC* and *SCADA* model. Also, the general loss gets smaller with increasing hidden size. Especially in the case of the *ACC* model, the loss shows outliers, while they are less intense when incorporating SCADA data as model features. This is mainly due to the highly dynamic characteristics of the acceleration data, which prevent correlation of the static component and tend to overfit.

In the analysis of LSTM models, it is observed that a greater hidden size yields a smaller training loss. However, improved performance is associated with a smaller hidden size for the validation data set. Models with hidden sizes of 75, 25, and 12 units were evaluated, with the model of 12 units showing the lowest standard deviation in performance. This finding contrasts the training loss data, which suggests superior performance for models with larger hidden sizes.

Figure 3.5 illustrates the performance of the validation data set. Notably, models with a smaller hidden size show a slightly more concentrated error distribution. Furthermore, the error plots reveal an increase in outliers and spikes as the hidden size grows, indicating a strong overfitting tendency in models with a hidden size of 75 units. Conversely, the model with a hidden size of 12 units demonstrates a significantly reduced occurrence of spikes compared to the model with a hidden size of 75 units, as seen especially between 350 kS and 400 kS i subplot (b), suggesting a more stable performance in subplot (f).

Considering the optimal model architecture with a hidden size of 12 units, further exploration with varying numbers of layers and sequence lengths is performed. Figure 3.6 presents the results from training *ACC+SCADA* models, as

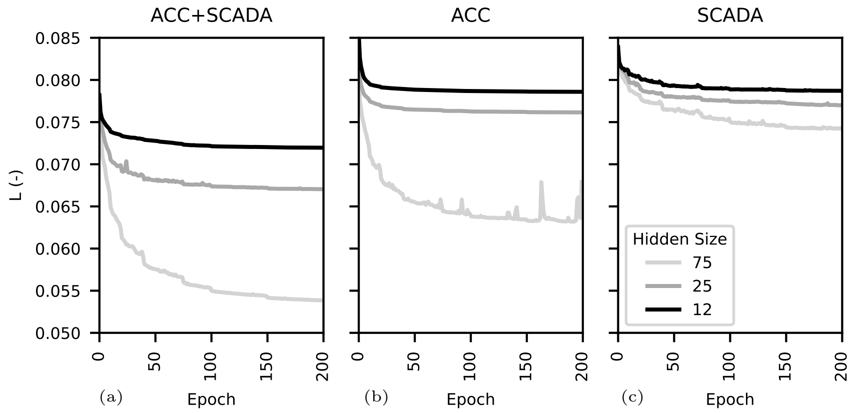

Figure 3.4: Training loss of *ACC+SCADA*, *ACC*, and *SCADA* models with varying hidden size.

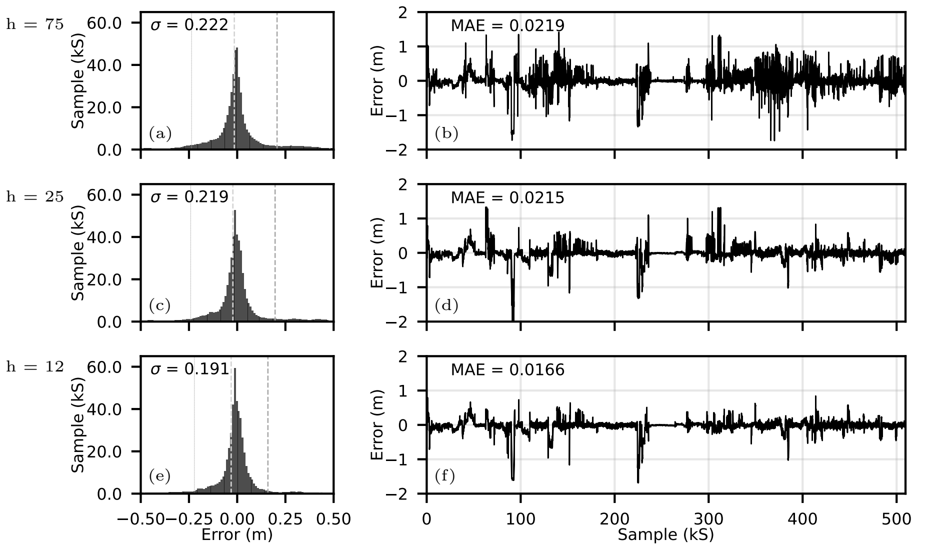

Figure 3.5: Error distribution (a, c, e) and prediction error (b, d, f) of *ACC* models with hidden size 75 (a, b), 25 (c, d), and 12 (e, f).

they show the highest potential in predicting tower displacement accurately. Sequence lengths are evaluated from 40 to 100 time steps, and layer numbers range from 1 to 4 hidden layers.

An extended sequence length is observed to enhance loss reduction, likely due to the time dependency in the time series data. Furthermore, increasing the number of hidden layers decreases the training loss, suggesting a more accurately fitting model. Unlike models with increased hidden sizes, those with more layers but reduced complexity demonstrate improved training outcomes. It is also noted that higher hidden sizes or layer numbers lead to longer training times and higher computational demands.

Figure 3.7 shows an overfitting issue in models with large hidden sizes and systematic and implausible deviations of the RTK based displacement (s). These deviations are largely attributed to ambiguity fix errors, the long baseline of 6 039 m, and the rover's elevated position at 304 m above the base station.

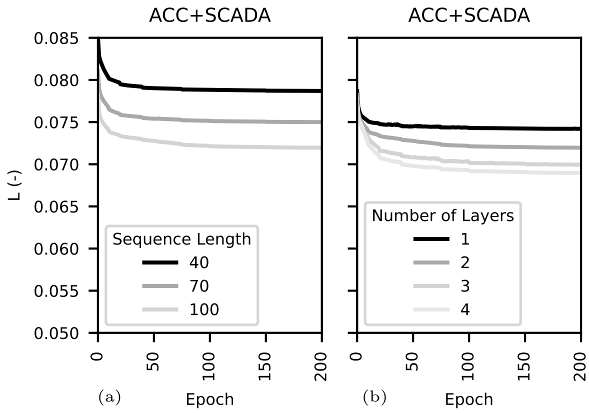

Figure 3.6: Training loss of *ACC+SCADA* model with varying sequence length and number of layers.

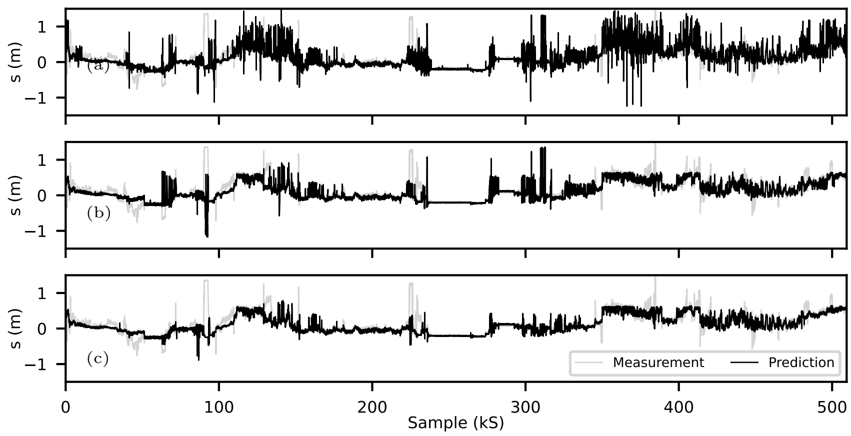

Figure 3.7: Model performance with validation data set of *ACC* models with hidden size (h) 75 (a), 25 (b), and 12 (c).

Table 3.4 details the training and validation losses for the *ACC+SCADA*, *ACC*, and *SCADA* models, using the epoch with the lowest loss.

Training losses decrease with increased hidden size, while validation losses rise, indicating overfitting in more complex models. Moreover, adding more layers lowers training loss but elevates validation loss. Conversely, shorter sequence lengths increase loss in both training and validation, suggesting a loss of critical data information.

The findings from Table 3.4 suggest that reducing model complexity significantly enhances precision, while shorter sequences, though reducing computational burden, lead to higher overall losses due to insufficient data usage.

To provide a detailed view of the model performance, one of the largest validation data segments from 2024-02-20 06:42:49 to 2024-02-20 06:54:19, encompassing 690 s of high-quality data, is visualized in Figure 3.8.

This period shows consistent data reliability, characterized by RTK quality indicators: $q = 1$, $\sigma_E = 0.009\,\mathrm{m}$, $\sigma_N = 0.011\,\mathrm{m}$, $\sigma_U = 0.010\,\mathrm{m}$, $t_{AOD} = 0.748\,\mathrm{s}$,

Model	**Architecture**	Epoch	$\mathbf{L_t}$ $(-)$	$\mathbf{L_v}$ $(-)$
ACC+SCADA	t100-h75-l2	198	0.04475	0.07482
ACC	t100-h75-l2	191	0.05007	0.07239
SCADA	t100-h75-l2	193	0.07226	0.06982
ACC+SCADA	t100-h25-l2	192	0.06492	0.06606
ACC	t100-h25-l2	170	0.07293	0.05860
SCADA	t100-h25-l2	196	0.07626	0.06766
ACC+SCADA	t100-h12-l2	199	0.07080	0.05712
ACC	t100-h12-l2	198	0.07601	0.05760
SCADA	t100-h12-l2	187	0.07833	0.06490
ACC+SCADA	t100-h12-l1	195	0.07359	0.05535
ACC+SCADA	t100-h12-l3	194	0.06834	0.06297
ACC+SCADA	t100-h12-l4	198	0.06731	0.06399
ACC+SCADA	t40-h12-l2	198	0.07797	0.06320
ACC+SCADA	t70-h12-l2	198	0.07407	0.05869

Table 3.4: Training and validation loss (L) of trained LSTM networks. (Architecture nomenclature: Sequence length - t; hidden size - h; number of layers: l).

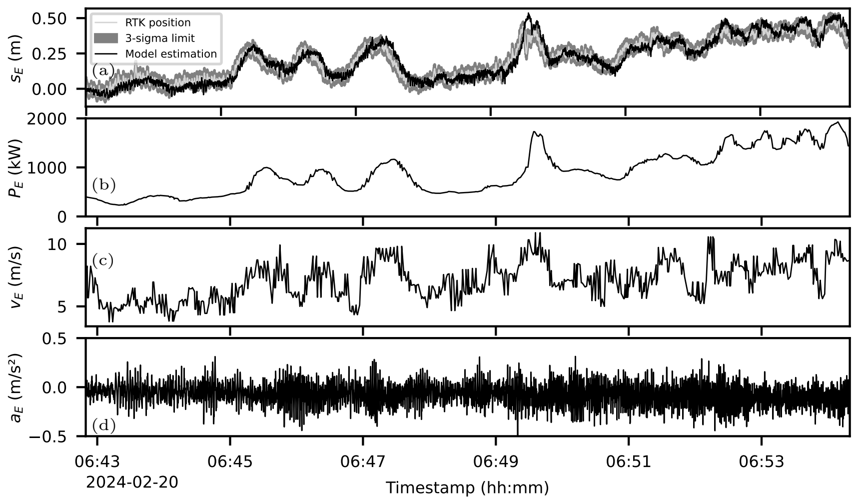

Figure 3.8: Detailed estimated displacement s_E (a), power output P_E (b), wind speed v_E (c), and acceleration a_E (d) of *ACC+SCADA* model (t100-h12-l2) of the selected period from 2024-02-20 06:42:49 to 2024-02-20 06:54:19.

$AR = 6.79$. The *ACC+SCADA* model, depicted in part (a) of the figure, demonstrates precise static and dynamic displacement of weight-induced bending, dynamic load-induced displacement, and excited natural frequencies caused by blade passing and turbulence. subfigure (b) shows the turbine's power output aligning very well with the lower dynamic components of the predicted displacement. The more dynamic wind speed in (c) also shows the tendency of the predicted displacement superimposed with wind gusts, which are exciting natural frequencies of the turbine, and the acceleration data in (d) best details the highly dynamic components of the turbine's motion.

Reduced models *ACC* and *SCADA* are shown in Figure 3.9 (b, c) with the *ACC+SCADA* model (a) as reference.

It indicates that although acceleration data seem to contain only highly dynamic components, the acceleration feature contains all the information necessary for representing the triplet of static displacement, dynamic load, and natural frequencies of the turbine. Using power output and wind speed only leads to less fitting natural frequencies but can accurately track dynamic load-induced displacements. As can be observed from Table 2.1, SCADA data has an event-driven sample rate $f_s <= 1\,\text{Hz}$. Although this complies with the Nyquist Theorem $f_s \geq 2 \cdot f_{\max}$ for the first bending Eigenfrequency of 0.27 Hz, resolution seems too low for accurately resolving the high dynamic. However, turbine operators and manufacturers may have access to higher-resolution data, which could mitigate this limitation and improve dynamic analysis.

For further validation of the applied techniques and models, modal analysis was conducted on data from 2024-02-21 08:45:00 to 2024-02-21 14:00:00, as evaluated in Figure 3.10. This interval is selected due to its constant wind speed $v_W = 4.58\,\text{m/s}$ with a standard deviation of $\sigma_v = 0.91\,\text{m/s}$ over a long period of 315 min. For a clear separation of the natural frequencies, it is important to maintain identical operating conditions with preferably minimal turbulence.

A study from Partovi-Mehr et al. (2022) found, that changes in operational and environmental conditions influence both the modal properties and damping ratios of the first bending Eigenfrequency of WT towers. The average power output of $P = 152.02\,\text{kW}$ indicates mostly turbine idle conditions with a very constant rotor speed of $\omega = 7.23\,1/\text{min}$ and standard deviation of $\sigma_\omega = 0.46\,1/\text{min}$, ensuring excitation of the turbines natural frequencies.

Table 3.5 provides a summary of the key operational parameters wind speed (v_w), power output (P), yaw angle (ϕ), and rotor speed (ω_R) during the analyzed period.

The presented plots reveal the excitation of the first two bending frequencies, $f_1 = 0.275\,\text{Hz}$ and $f_2 = 1.08\,\text{Hz}$, across all data sets. The RTK displacement and TMM predictions also capture blade passing frequencies, $p_1 = 0.117\,\text{Hz}$ and $p_3 = 0.350\,\text{Hz}$. However, p_1 exhibits relatively lower amplitudes in the acceleration reference, possibly due to sensor frequency response limitations. Conversely,

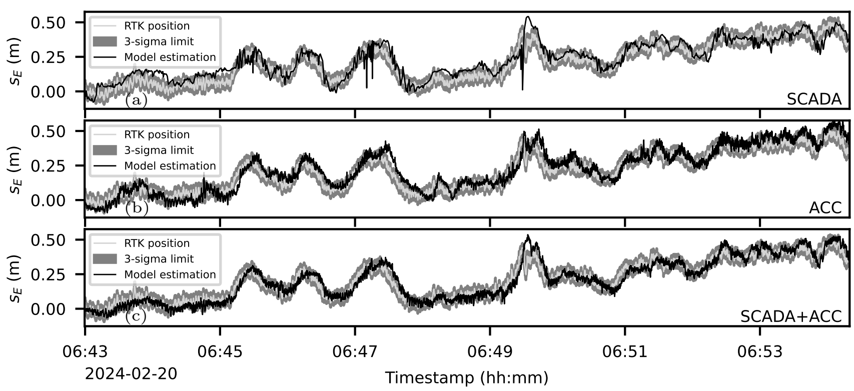

Figure 3.9: Detailed estimated displacement s_E of *ACC+SCADA* (a), *ACC* (b), and *SCADA* (c) with network architecture $t100$-$h12$-$l2$ of the selected period from 20.02.2024 06:42:49 to 20.02.2024 06:54:19.

	$\boldsymbol{v}$ (m/s)	$\boldsymbol{P}$ (kW)	$\boldsymbol{\phi}$ (deg)	$\boldsymbol{\omega}$ (1/min)
μ	4.58	152.02	246.91	7.23
σn	0.91	100.83	6.39	0.46

Table 3.5: Population mean μ and standard deviation σ of operational parameters in the modal analysis data set.

for the frequency f_2, the RTK displacement shows notably lower amplitudes. In addition to these identified frequencies, the data sets indicate the presence of other blade-related vibrational modes, such as flap and edgewise movements.

The TMM's ability to resolve both the lower frequency blade passing mode p_1 and the higher frequency mode f_2 proves the effectiveness of using LSTM networks for data fusion. This approach combines RTK and acceleration data to take advantage of the strengths of each measurement type, resulting in a more comprehensive frequency analysis.

The trained models, based on tower fixed coordinates representing the east direction and predominantly exposed to wind from west direction, might be directionally biased. This potential limitation in accurately predicting tower displacement for varying wind directions can be mitigated by incorporating acceleration data from the TMM in nacelle fixed coordinates.

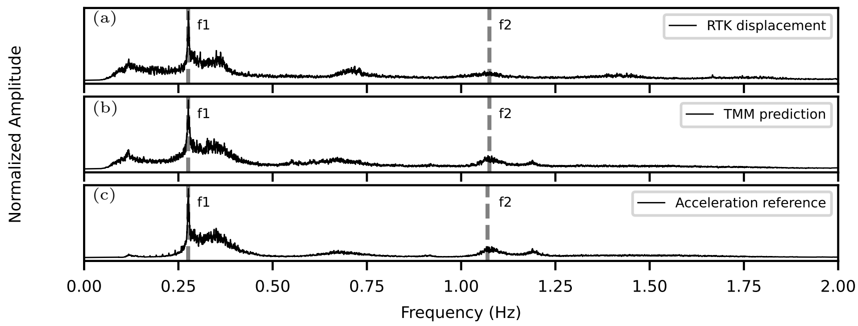

Figure 3.10: Frequency spectra of the RTK-based displacement (a), the TMM predicted displacement (b), and the acceleration data (c) as reference. Network architecture $t100$-$h12$-$l2$ of the period from 2024-02-21 08:45:00 to 2024-02-21 14:00:00.

Such an approach promises to make the models more robust against wind direction variability, potentially reducing data imbalances, overfitting, and static prediction errors. However, this approach introduces complexities when integrating RTK data, available in local tangent plane coordinates, projecting a North/East plane to the surface (Leick et al., 2015). Specifically, any misalignment of the RTK antenna relative to the turbine's vertical axis could lead to inaccuracies during nacelle rotation. Ideally, positioning the antenna along the tower's vertical axis could minimize such errors. However, this may increase multipath signal reflection issues due to the rotor being closer to the antenna.

4 Discussion

During this work, a literature review of possible damages to supporting structures of wind turbines was performed, considering critical and non-critical damages. It was found that most critical damages influence the stiffness and Young's modulus and, therefore, the natural frequencies and the load response of the supporting structures of wind turbines. Apart from fatigue due to cyclic load, connecting elements were critical for failure. While crack formation in welding, flanges, and bolts is challenging to detect in early states, missing pretension of tendons in the case of a hybrid tower design directly influences the tower's natural frequencies and is, therefore, detectable and quantifiable.

However, relying entirely on natural frequencies as indicators carries risks. Quasi-static structural responses cannot be tracked with Eigenfrequencies. Therefore, a method to estimate the tower top displacement with high static and dynamic precision is needed to be able to rely completely on it.

Considering measurement techniques that can be applied easily and used with minimal effort excludes measurements such as DIC, LDV, and TLS (Artese and Nico, 2020, Helming et al., 2021, Jonscher et al., 2023, Schill and Eichhorn, 2016), making it necessary to fuse data of high static precision with data of high dynamic precision. Using RTK, acceleration measurements, and optionally additional SCADA data, respectively, was found in this study to overcome these challenges.

After data gathering, a comprehensive data pre-processing depicted in Section 3.2 must be performed to ensure high data integrity. It is essential to adjust the sensor offsets precisely, which poses a great challenge when sensors are installed on a wind turbine subject to weight-induced and load-induced tower bending. The developed adjustment methods in Rupfle et al. (2024) (Publication 3) RSA, USA, and BSA aim to provide machine learning solutions for a fast initial adjustment using RSA, and data-driven approaches for uniaxial sensor and biaxial sensors using USA and BSA.

RSA uses a full 360-degree rotation of the nacelle, during which the weight of the nacelle and rotor causes the tower to bend in sync with the yaw angle. This movement generates a sinusoidal pattern in the measured data, including acceleration, RTK, tilt, and strain. These patterns can be analyzed to determine sensor offsets, orientations, and relative sensitivities. USA and BSA are methods that benefit from a broad variety of operational states (power output and yaw angle) of the wind turbine. The accuracy of the analysis methods relies heavily on the range of operational states included, as the turbine's centered position (no tower bending or displacement) is derived from the measured data, either in a uniaxial direction or through biaxial sensors.

A proper sensor adjustment including offset correction and orientation determination ensures that the TMM can fuse RTK and acceleration data with high accuracy. The first approach utilizing a KF for data fusion uses a state-space model consisting of equations of motion to estimate the optimal system state.

The results gathered in Rupfle et al. (2025) Publication 2 summarize fused results of the KF approach, showing stabilized static position data and outlier-filtered, denoised dynamic displacement measurements.

The method heavily relies on the accuracy and availability of RTK data. In contrast to other well-established measurement techniques, RTK is not a fail-safe technique as it relies on the line of sight of signals and is influenced by tropospheric & ionospheric conditions, multipath issues from the rotor, and stable connection of correction data input.

To address the RTK data availability and quality issue, a neural network, implemented as LSTM is deployed to predict the displacement using acceleration, power output, and wind speed data. The presented model is trained on a set of data spanning 90 days of recordings with the main wind direction ranging from South-West to North-West. Instead of deploying data imbalance measures, training was only performed with data of West-East axis. Acceleration data was therefore transformed into T coordinates and power output and wind speed vectors were decomposed into their respective east and north components. For reliable training, only RTK data with fixed solution status, low standard deviation, and high AR was included.

Training of a series of LSTM networks is performed to determine the best-performing network architecture and combination of network inputs. It is found that lower network complexity of small hidden size outperformed higher hidden size which showed overfitting and spiking issues. The input sequence length directly influences the prediction accuracy as short sequences contain less time-dependent state information. It was also found that acceleration data contains information from both static and dynamic displacements. In contrast, input from SCADA data can not reconstruct the dynamic displacement due to the low sampling rate $f_s <= 1\,\mathrm{Hz}$. The combination of acceleration and SCADA data provides a robust and outlier minimized network input capable of accurately predicting the tower top displacement.

Training in nacelle fixed coordinates FA/SS can significantly improve direction-dependent data imbalance. Additionally, operational condition imbalances can be diminished by resampling techniques, oversampling the turbine's minor operational states, or by deploying focal loss (Lin et al., 2020) to network training to further balance the training data. A further training result improvement can be achieved by using the findings from Rupfle et al. (2025) Publication 2 as training labels to provide smoothed and outlier-reduced training data with precise phase and frequency content.

Building on the results for displacement prediction, a key consideration is the systems scalability across identical turbines operating in comparable wind class conditions. Pre-trained models for time-series are investigated in Ma et al. (2024) and can be fine-tuned to be employed at different sites in various turbine and tower types. Using high-resolution SCADA data allows for scalability of a SCADA-only model to track the load history of a wind park to calculate RUL as a key enabler for lifetime extension of repowering according to Botz (2022), Botz et al. (2020), Loew et al. (2019), Osterminski and Gehlen (2018). Accurate RUL estimation for specific tower components such as transition pieces or specific segments significantly benefits from the involvement of modal shape functions of the 1^{st} and 2^{nd} bending mode to accurately determine the underlying curvature and bending moments acting on the structure. Mode shape identification can be performed using measured acceleration data. It is possible to determine the mode shapes using single-point measurement. Still, the accuracy significantly increases with involving at least a second measurement at a tower height representing the 2^{nd} bending mode well.

For simplification, generic mode shapes from cantilever beams or rigid body structures can be utilized (Vallabhaneni and Maity, 2011). It is further possible to extract mode shapes with short-term TLS measurements (Dilek et al., 2019) and DIC (Lin et al., 2021) or to use well-established mode shapes from reference turbines such as *NREL* 5 MW *offshore* (Jonkman et al., 2009). Utilizing mode shapes and displacement data enables modal expansion without employing FEM (Iliopoulos et al., 2017). A study from Rzepka and Ziaja (2024) shows damage detection capabilities of mode shape changes of cantilever beams using DIC and concludes, that displacement field changes can approximate localization damage.

Usage of displacement data and mode shape information can be utilized to perform simulations of simple and computationally efficient 2-DOF models with well-established tools like *openFAST* (Jonkman, 2013) (*BeamDyn*, *ElastoDyn*), *YAMS* (Branlard and Geisler, 2022), and *HAWC2*, presented in Larsen and Hansen (2007).

Displacement predicting ANNs enable the prediction of the true system state and allows for anomaly detection based on static and dynamic displacement values using Bayesian models (Nguyen and Goulet, 2019), independent component analysis (Liu et al., 2020), Gaussian mixture models (Hasegawa et al., 2020), or by predictive POD curves (Mendler et al., 2023).

Although the system's design is intended to work as a stand-alone solution, further acceleration sensor to identify mode shapes would not only allow for initial mode shape assessment through SSI for RUL estimation. Still, it would also enable damage detection and localization through changes in mode shapes (Janeliukstis et al., 2017, Pandey et al., 1991, Tejada, 2009, Zhao et al., 2016).

The TMM utilizes an MQTT based real-time environment capable of transmitting data to an unlimited number of clients. The real-time connection was tested up to a sample rate $f_s = 20\,\text{Hz}$ without showing signs of increasing latency. Cimdins et al. (2021) reports a maximum achievable sample rate of $f_s = 5000\,\text{Hz}$. The system can be operated as a standalone system or connected to a cloud solution, enabling MQTT message exchange with a NoSQL database, allowing direct access to real-time and historical data. RUL estimating modules interact directly with the database to compute damage equivalents of structural parts which are subsequently added to the database. Damage equivalents are computed continuously or on demand. The digital shadow provided by these methods can be accessed using visualization tools such as *Grafana* (Chakraborty and Kundan,

2021) and *ThingsBoard* (Henschke et al., 2020), making it a user-interactable environment.

The greatest potential for reducing sources of uncertainties in the methods are data quality improvements. RTK data are very sensitive to satellite signal quality and antenna positioning. Incorrectly fixed integer carrier phase ambiguities may result in large positioning errors (Verhagen, 2015) and off-axis antenna positioning leads to a direction-dependent drift of the measured position. Correction functions of the form $x' = x_{offs.} \cos(\Theta) - y_{offs.} \sin(\Theta)$ and $y' = x_{offs.} \sin(\Theta) + y_{offs.} \cos(\Theta)$, respectively, might lead to additional uncertainties and shall be avoided wherever possible. In contrast to the off-axis issue, an antenna position in the tower axis leads to multi-path reflections originating from the rotor blades. Furthermore, a long baseline leads to a loss in correction accuracy and poses the risk of static drifts. A study from Janos et al. (2022) sees the antenna as a critical component of low-cost receivers, due to the noticeable degradation in positioning accuracy and low signal-to-noise ratio.

5 Conclusion

This work elaborates on SHM methods for supporting structures of WT. The main focus lies on the assessment of tower top displacement and the development of measurement solutions, including hardware and a corresponding holistic environment that can assess structural health as a basis for RUL determination, detection & localization of damage, and the detection of anomalies.

"*Investigation of the Measurability of Selected Damage to Supporting Structures of Wind Turbines*" (Publication 1) laid the foundation for the research problem addressed. The damage scenarios of supporting structures of WTs were investigated and the necessity of monitoring static and dynamic deflection in addition to pure frequency analysis was identified. The investigation of dynamic displacement in time and frequency domain found that the present measurement technique is able to accurately capture the structural dynamics.

Within the work, possible damages were evaluated to assess knowledge of the influences different damages have on the structure. Critical damage found is for example missing pretension in tendons and degradation of reinforced concrete. The main findings of the publication can be described as follows:

- Critical damages influence the natural frequencies and mode shapes of the structure and are accessible with acceleration and tower displacement measurements.
- Directional dependent data of natural frequencies, stiffness, and damping can be used to localize structural changes.
- Acceleration data poses great potential in computing dynamic displacement in time and frequency domain, but cannot be used alone to calculate static displacement.

In a study by Botz et al. (2020), remaining useful life (RUL) was evaluated using stress values derived from strain measurements. However, it was found that the resulting estimates were too high to be realistic. This work elaborates on an approach to precisely determine tower top displacement that can provide the foundation for more accurate RUL determination. Instead of strain measurements, the tower deflection or displacement shall be used to determine stress in the material. A realistic RUL assessment based on displacement data is only possible incorporating static and dynamic values of a structure. Assessment of static displacement using conventional methods in time or frequency domain poses difficulties due to an error drift. Therefore, static displacement must be assessed using different measurement techniques.

In "*Development of a Minimalistic Smart Sensor System for Motion Measurement of Wind Turbine Towers*" (Publication 2), a data fusion approach utilizing a KF and acceleration and RTK data was developed, that allows static displacement calculation besides the dynamic displacement calculation.

- RTK shows great long-term stability in static displacement measurements and can provide dynamic displacement within the sub-centimeter level.
- Tower top displacement can be assessed using RTK measurements.
- Availability of high quality RTK data is very limited due to tropospheric and ionospheric environmental aspects.
- Data fusion of acceleration and RTK data to assess tower top displacement can be achieved using a KF, combining high dynamic of acceleration measurements with high static precision of RTK data, but heavily relies on the RTK signal quality.
- Data integrity of all measurement data relies on a precise sensor adjustment.

The method was tested on a hardware platform specifically developed for this purpose forming a first prototype of the TMM. The approach significantly improves the measurement data in terms of accuracy. The method eliminates the displacement drift associated with purely vibration based displacement calculations. A major drawback of the method is the need of the availability of high quality RTK data and sensor adjustment issues of the input data. In order to ensure accurate measurement data, sensor adjustments need to be carried out. As WT are not in a state of equilibrium when shut down, the sensor adjustments need to be carried out under operation or under reproducible conditions.

"*Operational Sensor Adjustment for Structural Health Monitoring Systems in Wind Turbines using Machine Learning*" (Publication 3) introduces three methods RSA, USA, and BSA for sensor adjustment, orientation determination, and long-term sensitivity tracking using uni- and biaxial sensor data for post-installation adjustment and for the use with more comprehensive operational data:

- RSA is utilized for initial adjustment immediately post-installation for determining offsets and orientations.
- USA is utilized for a more comprehensive adjustment of a single sensor axis using operational data in positive and negative directions of the sensor axis.
- BSA is utilized for biaxial sensors using operational data of two perpendicular sensor axes without the need to include yaw angle measurements.

The methods significantly improve sensor adjustment and provide the foundation for continuous monitoring applying enhanced techniques that use static and dynamic displacement data sources. RTK data as label and measurement data such as acceleration data and SCADA data as features is deployed to train a ML model that additionally enhances data availability and accuracy.

"*Soft real-time framework for Structural Health Monitoring of wind turbine supporting structures*" (Publication 4) elaborates on the functionality and connectivity of the software for the TMM and develops a real-time capable environment that utilizes MQTT for data transfer and a database for data storage.

Additionally, "*Analysis of Icing on Wind Turbines by Combined Wireless and Wired Acceleration Sensor Monitoring*" (Publication 5) investigates icing of rotor blades. Frequency analysis is utilized to estimate ice mass on rotor blades and underlines the importance of an accurate representation of the frequency spectra.

Besides the associated and additional publications, Chapter 3 elaborates on a further development of the TMM utilizing the aforementioned methods and findings. A LSTM network is deployed and trained on high quality RTK data input data. This allows precise prediction of static and dynamic tower top displacement even under absence of RTK data and thus overcomes the aforementioned availability issue and can be described as follows:

- Utilizing an LSTM network to train the tower top displacement based on acceleration and SCADA data enhances the availability and accuracy of the result.
- RTK data is only necessary for training of the LSTM network.
- Prediction of the tower displacement is then made using only the features the LSTM is trained on.
- Training data is indicative of at least one feature of: Acceleration, wind speed, power output, inclination, strain, wind direction.
- Additionally, the following features can be supplemented and may further improve prediction accuracy: Temperature, dew point, humidity, freezing altitude, precipitation.

In Chapter 3, the training features are limited to acceleration, power output, and wind speed, simplifying both the model complexity and the training process. Incorporating additional features leads to a more complex input structure and significantly increases training duration and the computational resources required. Additionally, the more complex input structure requires more training data to be able to learn an appropriate behavior and to reduce overfitting issues. To enhance generalizability of the trained model, training data sources can be various WT of very similar structures and characteristics. It is also possible to provide a pre-trained model based on a broad variety of WT structures and to fine-tune the model to a specific WT.

The developed method can be applied to tasks ranging from anomaly detection in a single turbine to monitoring an entire wind park and estimating the remaining service life of turbines. Generalizability and adaptability are key aspects to be addressed in future research. To ensure generalizability across turbine types, it is recommended to equip multiple identical WTs in a wind park with the same measurement setup. Cross-validation at the park level should be performed using training data from several turbines.

For scalability studies, training models in the FA/SS direction is recommended. This approach simplifies the training process and enhances generalizability. However, for detailed monitoring of individual turbines, such as for damage detection and localization, training on E/N data instead of FA/SS data is preferable. This allows the model to capture direction-dependent differences in behavior and characteristics. The performed experiments showed overall excellent results and lead to the following conclusions:

- Prediction of tower displacement using a trained LSTM outperforms input data and increases availability due to use of more robust measurement techniques.
- The method allows for scalability, enabling the use of this method in wind parks with minimal measurement setups or even without additional instrumentation installed in further wind turbines.

- Displacement prediction from LSTM network combines the strengths of both acceleration and RTK measurements in resolving the observed frequency spectrum.
- Tower top displacement can be extrapolated to any tower height using modal expansion or well-established simulation tools using a 2-DOF model.
- Accurately predicted frequency spectra that allow for anomaly detection
- Modal shape assessment allows damage detection and localization
- Extrapolation of tower top displacement allows RUL estimation deploying state of the art methods.

In conclusion, future research to explore scalability at both the turbine and park levels, as well as across various turbine types can be carried out. Additionally, the performance of the methods in tower-fixed directions versus nacelle directions requires further evaluation to determine the relative advantages and disadvantages of each configuration. In addition, the use of sensors at multiple locations can lead to improvements in determining the mode shapes and can be further investigated. Finally, larger data sets, potentially including multiple turbines, will enable the evaluation of additional training features to further increase overall model performance and to investigate potential pre-training methods.

The dissertation's findings extend into practical applications, resulting in a patent application, submitted on the 11.10.2024. The patent describes a method for determining the spatial position of parts of infrastructure elements, specifically wind turbine towers. The method combines multiple data sources to monitor both static and dynamic behavior accurately. The invention includes a method for monitoring the infrastructure element, a method for training the data model, a data processing apparatus, and a computer software including a computer readable storage medium.

The patent claims are based on the findings of the associated and additional publications of this dissertation.

Acknowledgement

This dissertation was funded by the *German Federal Ministry for Economic Affairs and Climate Action* through the projects *MISTRALWIND* under grant number 0325795 and *IM Wind* under grant number ZF4561204DB9, as well as supported by the *TUM International Graduate School of Science and Engineering (IGSSE)*.

I would like to thank *Max Bögl Wind AG* and *Siemens Gamesa Renewable Energy* for granting access to the test facility and providing invaluable expertise during numerous measurement campaigns.

My special thanks go to the entire *IM Wind* project team, particularly Dr.-Ing. Robert Diemer and Markus Nowack, for their intense support. I am also grateful to Dr.-Ing. Altuğ Emiroğlu for his generous knowledge transfer and modeling expertise, and to Bernhard Wondra for the close collaboration and tireless work on the wind turbine. Many thanks to Dr.-Ing. Max Botz for the valuable preliminary work and excellent introduction to the subject. I extend my gratitude to Prof. Dr.-Ing. Christian Große for many unforgettable memories, especially during our time in Egypt. I am equally thankful to all my colleagues there, with special mention to Johannes Scherr for his motivation, thesis revision, and close friendship.

Finally, I wish to thank Dra. Cecilia Smoglie and Patricio Neffa for their mentorship and support during my time in Buenos Aires.

References

Abdullahi, A., Bhattacharya, S., Li, C., Xiao, Y., and Wang, Y. (2022). Long term effect of operating loads on large monopile-supported offshore wind turbines in sand. *Ocean Engineering*, 245:110404.

Abel, D., Barreto, A., Van Roy, B., Precup, D., van Hasselt, H. P., and Singh, S. (2023). A definition of continual reinforcement learning. In Oh, A., Naumann, T., Globerson, A., Saenko, K., Hardt, M., and Levine, S., editors, *Advances in Neural Information Processing Systems*, volume 36, pages 50377–50407. Curran Associates, Inc.

Aggarwal, C. (2023). *Neural Networks and Deep Learning: A Textbook*. Springer Cham.

Ahn, Y. W., Kim, D., and Dare, P. (2006). Local Tropospheric Anomaly Effects on gps rtk Performance. In *Proceedings of the 19th International Technical Meeting of the Satellite Division of The Institute of Navigation (ION GNSS 2006)*, pages 1925–1935.

Alonso-Martinez, M., Adam, J. M., Alvarez-Rabanal, F. P., and del Coz Díaz, J. J. (2019). Wind turbine tower collapse due to flange failure: FEM and DOE analyses. *Engineering Failure Analysis*, 104:932–949.

Artese, S. and Nico, G. (2020). TLS and GB-RAR Measurements of Vibration Frequencies and Oscillation Amplitudes of Tall Structures: An Application to Wind Towers. *Applied Sciences*, 10(7):2237.

Asesh, A. (2022). Normalization and Bias in Time Series Data. In *Digital Interaction and Machine Intelligence*, Lecture Notes in Networks and Systems, pages 88–97. Springer, Cham.

Barahona, B., Hoelzl, C., and Chatzi, E. (2017). Applying Design Knowledge and Machine Learning to scada Data for Classification of Wind Turbine Operating Regimes. In *2017 IEEE Symposium Series on Computational Intelligence (SSCI)*. IEEE.

Baybura, T., Tiryakioğlu, I., Uğur, M. A., Solak, H. I., and Şafak, Ş. (2019). Examining the Accuracy of Network RTK and Long Base RTK Methods with Repetitive Measurements. *Journal of Sensors*, 2019:1–12.

Bishop, C. M. and Bishop, H. (2024). *Deep Learning: Foundations and Concepts*. Springer.

Botz, M. (2022). *Structural Health Monitoring der Tragstruktur von Windenergieanlagen*. PhD thesis, Technische Universität München.

Botz, M., Emiroglu, A., Osterminski, K., Raith, M., Wüchner, R., and Große, C. (2020). Überwachung und Modellierung der Tragstruktur von Windenergieanlagen. *Beton Stahlbetonbau*, 115(5):342–354.

Botz, M., Oberländer, S., Raith, M., and Grosse, C. (2016). Monitoring of Wind Turbine Structures with Concrete-steel Hybrid-tower Design. In *8th European Workshop on Structural Health Monitoring (EWSHM 2016)*.

Botz, M., Raith, M., Emiroglu, A., and Grosse, C. U. (2017a). Monitoring of Wind Turbine Structures Using Stationary Sensors and Short-term Optical Techniques. In *Structural Health Monitoring 2017*, Lancaster, PA. DEStech Publications, Inc.

Botz, M., Zhang, Y., Raith, M., and Pinkert, K. (2017b). Operational Modal Analysis of a Wind Turbine during Installation of Rotor and Generator. In *7th International Operational Modal Analysis Conference (IOMAC)*, pages 224–227.

Bracke, S. (2024). *Reliability Engineering: Data analytics, modeling, risk prediction*. Springer Berlin Heidelberg, Berlin, Heidelberg.

Branlard, E. and Geisler, J. (2022). A symbolic framework to obtain mid-fidelity models of flexible multibody systems with application to horizontal-axis wind turbines. *Wind Energy Sciience*, 7(6):2351–2371.

Branlard, E., Giardina, D., and Brown, C. S. D. (2020). Augmented kalman filter with a reduced mechanical model to estimate tower loads on a land-based wind turbine: a step towards digital-twin simulations. *Wind Energy Science*, 5(3):1155–1167.

Brincker, R. and Ventura, C. (2015). *Introduction to Operational Modal Analysis*. John Wiley & Sons, Ltd, Nashville, TN.

Calin, O. (2020a). Activation functions. In *Deep Learning Architectures: A Mathematical Approach*, pages 21–39. Springer, Cham.

Calin, O. (2020b). Cost functions. In *Deep Learning Architectures: A Mathematical Approach*, pages 41–68. Springer, Cham.

Calin, O. (2020c). *Deep Learning Architectures: A Mathematical Approach*. Springer, Cham.

Chakraborty, M. and Kundan, A. P. (2021). *Monitoring Cloud-Native Applications*. APress, Berlin, Germany, 1 edition.

Chou, J.-S., Ou, Y.-C., and Lin, K.-Y. (2019). Collapse mechanism and risk management of wind turbine tower in strong wind. *Journal of Wind Engineering and Industrial Aerodynamics*, 193(103962):103962.

Cimdins, M., John, F., and Hellbrueck, H. (2021). Flexible Data Acquisition with LoRaWAN and MQTT for Small and Medium-sized Enterprises. In *Mobile Communication - Technologies and Applications; 25th ITG-Symposium*, pages 1–6.

Civera, M. (2021). *Vibration-based Assessment of Structural Changes in the Linear and Nonlinear Response of Mechanical Structures for Aerospace Applications*. PhD thesis, Politecnico di Torino.

Civera, M. and Surace, C. (2021). A comparative analysis of signal decomposition techniques for structural health monitoring on an experimental benchmark. *Sensors (Basel)*, 21(5):1825.

Civera, M. and Surace, C. (2022). Non-Destructive Techniques for the Condition and Structural Health Monitoring of Wind Turbines: A Literature Review of the Last 20 Years. *Sensors (Basel)*, 22(4):1627.

Cooley, J. W. and Tukey, J. W. (1965). An Algorithm for the Machine Calculation of Complex Fourier Series. *Mathematics of computation*, 19(90):297–301.

Crespi, N., Drobot, A. T., and Minerva, R., editors (2023). *The Digital Twin*. Springer International Publishing.

Dai, K., Huang, Y., Gong, C., Huang, Z., and Ren, X. (2015). Rapid seismic analysis methodology for in-service wind turbine towers. *Earthq. Eng. Eng. Vib.*, 14(3):539–548.

Dai, K., Sheng, C., Zhao, Z., Yi, Z., Camara, A., and Bitsuamlak, G. (2017). Nonlinear response history analysis and collapse mode study of a wind turbine tower subjected to tropical cyclonic winds. *Wind and Structures*, 25(1):79–100.

Dilek, A. U., Oguz, A. D., Satis, F., Gokdel, Y. D., and Ozbek, M. (2019). Condition monitoring of wind turbine blades and tower via an automated laser scanning system. *Engineering Structures*, 189:25–34.

Ehrig, L., Atzberger, D., Hagedorn, B., Klimke, J., and Dollner, J. (2020). Customizable Asymmetric Loss Functions for Machine Learning-based Predictive Maintenance. In *2020 8th International Conference on Condition Monitoring and Diagnosis (CMD)*. IEEE.

Esakkirajan, S., Veerakumar, T., and N Subudhi, B. (2024). *Digital Signal Processing*. Springer Singapore.

Feliciano, J., Cortina, G., Spear, A., and Calaf, M. (2018). Generalized analytical displacement model for wind turbine towers under aerodynamic loading. *Journal of Wind Engineering and Industrial Aerodynamics*, 176:120–130.

García Márquez, F. P. and Peinado Gonzalo, A. (2021). A Comprehensive Review of Artificial Intelligence and Wind Energy. *Archives of Computational Methods in Engineering*, 29(5):2935–2958.

Geiss, C. T. and Grosse, C. U. (2018). A concept for a holistic risk-based operation and maintenance strategy for wind turbines. In *Safety and Reliability–Safe Societies in a Changing World*, pages 539–546. CRC Press.

Geiss, C. T., Kinscherf, S., Decker, M., Romahn, S., Botz, M., Raith, M., Wondra, B., Grosse, C. U., Osterminski, K., Emiroglu, A., Bletzinger, K.-U., Obradovic, D., and Wever, U. (2017). The Mistralwind Project—Towards a Remaining Useful Lifetime Analysis and Holistic Asset Management Approach for More Sustainability of Wind Turbine Structures. In *11th International Workshop on Structural Health Monitoring*. Stanford University.

Germanischer Lloyd (2007). Germanischer Lloyd Guidelines IV - Part 6. Guideline for the Certification of Offshore Wind Turbines.

Goodfellow, I., Bengio, Y., and Courville, A. (2016). *Deep Learning.* MIT Press.

Goyal, M., Goyal, R., Venkatappa Reddy, P., and Lall, B. (2020). Activation functions. In *Deep Learning: Algorithms and Applications*, pages 1–30. Springer International Publishing, Cham.

Granacher, J., Nguyen, T.-V., Castro-Amoedo, R., and Maréchal, F. (2022). Overcoming decision paralysis—A digital twin for decision making in energy system design. *Applied Energy*, 306:117954.

Greiner, R., Berger, D., and Böck, M. (2022). *Analytics und Artificial Intelligence: Datenprojekte mehrwertorientiert, agil und nachhaltig planen und umsetzen.* Springer Fachmedien Wiesbaden.

Grillmeyer, O. (1998). Artificial intelligence. In *Exploring Computer Science with Scheme*, pages 411–474. Springer, New York, NY.

Grosse, C. (2012). Non-destructive testing and continuous monitoring: Modern tools for performance assessment and life time prognosis of structures. In *Concrete Repair, Rehabilitation and Retrofitting III.* Taylor & Francis.

Grosse, C. U., Ohtsu, M., Aggelis, D. G., and Shiotani, T., editors (2022). *Acoustic Emission Testing.* Springer Tracts in Civil Engineering. Springer Cham, 2 edition.

Grundkötter, E. and Melbert, J. (2021). Precision blade deflection measurement system using wireless inertial sensor nodes. *Wind Energy*, 25(3):432–449.

Gumilar, I., Bramanto, B., Rahman, F. F., and Hermawan, I. M. D. A. (2019). Variability and Performance of Short to Long-Range Single Baseline RTK GNSS Positioning in Indonesia. *E3S Web of Conferences*, 94:01012.

Haney, M. M., Power, J., West, M., and Michaels, P. (2012). Causal Instrument Corrections for Short-Period and Broadband Seismometers. *Seismological Research Letters*, 83(5):834–845.

Harris, F. J. (1978). On the Use of Windows for Harmonic Analysis with the Discrete Fourier Transform. *Proceedings of the IEEE*, 66(1):51–83.

Hasegawa, T., Ogata, J., Murakawa, M., Kobayashi, T., and Ogawa, T. (2020). Adaptive training of vibration-based anomaly detector for wind turbine condition monitoring. *International Journal of Prognostics and Health Management*, 8(2).

Hassanien, A. E., Darwish, A., and Snasel, V., editors (2022). *Digital Twins for Digital Transformation: Innovation in Industry.* Springer Cham.

He, H., Meng, X., Wang, Y., Khajepour, A., An, X., Wang, R., and Sun, F. (2024). Deep reinforcement learning based energy management strategies for electrified vehicles: Recent advances and perspectives. *Renewable and Sustainable Energy Reviews*, 192:114248.

Helming, P., von Freyberg, A., Sorg, M., and Fischer, A. (2021). Wind Turbine Tower Deformation Measurement Using Terrestrial Laser Scanning on a 3.4 MW Wind Turbine. *Energies*, 14(11):3255.

Henschke, M., Wei, X., and Zhang, X. (2020). Data Visualization for Wireless Sensor Networks Using ThingsBoard. In *2020 29th Wireless and Optical Communications Conference (WOCC)*. IEEE.

Hernandez-Estrada, E., Lastres-Danguillecourt, O., Robles-Ocampo, J. B., Lopez-Lopez, A., Sevilla-Camacho, P. Y., Perez-Sariñana, B. Y., and Dorrego-Portela, J. R. (2021). Considerations for the structural analysis and design of wind turbine towers: A review. *Renewable and Sustainable Energy Reviews*, 137(110447):110447.

Hochreiter, S. and Schmidhuber, J. (1997). Long Short-Term Memory. *Neural Computation*, 9(8):1735–1780.

Horváth, B. (2023). Merging of measurement data from various structural health monitoring systems for further analysis. Bachelor's thesis, Technical University of Munich.

IEC (2019). IEC 61400-1: Wind turbines - Part 1: Design requirements. International Standard.

Iliopoulos, A., Weijtjens, W., Van Hemelrijck, D., and Devriendt, C. (2017). Fatigue assessment of offshore wind turbines on monopile foundations using multi-band modal expansion. *Wind Energy*, 20(8):1463–1479.

Ivanov, T. and Pergolesi, M. (2020). The impact of columnar file formats on SQL-on-hadoop engine performance: A study on ORC and parquet. *Concurrency and Computation*, 32(5).

Janeliukstis, R., Rucevskis, S., Wesolowski, M., and Chate, A. (2017). Experimental structural damage localization in beam structure using spatial continuous wavelet transform and mode shape curvature methods. *Measurement (Lond.)*, 102:253–270.

Janos, D., Kuras, P., and Łukasz Ortyl (2022). Evaluation of low-cost RTK GNSS receiver in motion under demanding conditions. *Measurement*, 201:111647.

Jonkman, J. (2013). The New Modularization Framework for the FAST Wind Turbine CAE Tool. In *51st AIAA Aerospace Sciences Meeting including the New Horizons Forum and Aerospace Exposition*, Reston, Virigina. American Institute of Aeronautics and Astronautics.

Jonkman, J., Butterfield, S., Musial, W., and Scott, G. (2009). Definition of a 5-MW Reference Wind Turbine for Offshore System Development. Technical report, NREL.

Jonscher, C., Helming, P., Märtins, D., Fischer, A., Bonilla, D., Hofmeister, B., Grießmann, T., and Rolfes, R. (2023). Dynamic displacement measurement of a wind turbine tower using accelerometers: tilt error compensation and validation. *Wind Energy Science Discussions*, 2023:1–21.

Jung, A. (2022). *Machine Learning: The Basics*. Springer Singapore.

Kalman, R. E. (1960). A New Approach to Linear Filtering and Prediction Problems. *Journal of Basic Engineering*, 82(1):35–45.

Kang, H., Jung, S., Kim, H., Jeoung, J., and Hong, T. (2024). Reinforcement learning-based optimal scheduling model of battery energy storage system at the building level. *Renewable and Sustainable Energy Reviews*, 190:114054.

Kapoor, S., Cantrell, E., Peng, K., Pham, T. H., Bail, C. A., Gundersen, O. E., Hofman, J. M., Hullman, J., Lones, M. A., Malik, M. M., Nanayakkara, P., Poldrack, R. A., Raji, I. D., Roberts, M., Salganik, M. J., Serra-Garcia, M., Stewart, B. M., Vandewiele, G., and Narayanan, A. (2023). REFORMS: Reporting Standards for Machine Learning Based Science.

Kaspar, F., Borsche, M., Pfeifroth, U., Trentmann, J., Drücke, J., and Becker, P. (2019). A climatological assessment of balancing effects and shortfall risks of photovoltaics and wind energy in germany and europe. *Advances in Science and Research*, 16:119–128.

Khazaee, M., Derian, P., and Mouraud, A. (2022). A comprehensive study on structural health monitoring (shm) of wind turbine blades by instrumenting tower using machine learning methods. *Renewable Energy*, 199:1568–1579.

Kingma, D. P. and Ba, J. (2014). Adam: A Method for Stochastic Optimization. *CoRR*, abs/1412.6980.

Kritzinger, W., Karner, M., Traar, G., Henjes, J., and Sihn, W. (2018). Digital twin in manufacturing: A categorical literature review and classification. *IFAC-PapersOnLine*, 51(11):1016–1022.

Larsen, T. and Hansen, A. (2007). *How 2 HAWC2, the user's manual*. Number 1597(ver. 3-1)(EN) in Denmark. Forskningscenter Risoe. Risoe-R. Risø National Laboratory.

LeCun, Y., Bengio, Y., and Hinton, G. (2015). Deep learning. *Nature*, 521(7553):436–444.

Lee, Y.-L., Barkey, M. E., and Kang, H.-T. (2014). *Metal Fatigue Analysis hHandbook*. Butterworth-Heinemann, Woburn, MA.

Leick, A., Rapoport, L., and Tatarnikov, D. (2015). Geodesy. In *GPS Satellite Surveying*, chapter 4, pages 129–206. John Wiley & Sons, Ltd.

Lin, T.-Y., Goyal, P., Girshick, R., He, K., and Dollár, P. (2020). Focal loss for dense object detection. *IEEE Transactions on Pattern Analysis and Machine Intelligence*, 42(2):318–327.

Lin, Y.-C., Chiang, C.-H., Yu, C.-P., Kumar, D., and Hsu, K.-T. (2021). Application of DIC method to modal vibration study for structure health monitoring of WT tower. *International Journal of Applied Science and Engineering*, 18:1–9.

Liu, C., Wang, Y., Yang, C., and Gui, W. (2024). Multimodal Data-Driven Reinforcement Learning for Operational Decision-Making in Industrial Processes. *IEEE/CAA Journal of Automatica Sinica*, 11(1):252–254.

Liu, Y. and Ishihara, T. (2015). Fatigue Failure Accident of wind turbine tower in Taikoyama Wind Power Plant. *EWEA2015, Paris, France (November, 2015).*

Liu, Y., Yeoh, J. K. W., and Chua, D. K. H. (2020). Deep Learning–Based Enhancement of Motion Blurred UAV Concrete Crack Images. *J. Comput. Civ. Eng.*, 34(5):04020028.

Loew, S., Obradovic, D., and Bottasso, C. L. (2019). Direct Online Rainflow-counting and Indirect Fatigue Penalization Methods for Model Predictive Control. In *2019 18th European Control Conference (ECC)*. IEEE.

Luo, J., Zhang, Z., Fu, Y., and Rao, F. (2021). Time series prediction of COVID-19 transmission in America using LSTM and XGBoost algorithms. *Results in Physics*, 27:104462.

Ma, Q., Liu, Z., Zheng, Z., Huang, Z., Zhu, S., Yu, Z., and Kwok, J. T. (2024). A survey on time-series pre-trained models. *IEEE Transactions on Knowledge and Data Engineering*, 36(12):7536–7555.

Ma, Y., Martinez-Vazquez, P., and Baniotopoulos, C. (2019). Wind Turbine Tower Collapse Cases: A Historical Overview. *Institution of Civil Engineers. Proceedings. Structures and Buildings*, 172(8):547–555.

Mahalle, P. N., Shinde, G. R., Ingle, Y. S., and Wasatkar, N. N. (2023). *Data Centric Artificial Intelligence: A Beginner's Guide*. Springer Singapore.

Manaswi, N. K. (2018). Rnn and lstm. In *Deep Learning with Applications Using Python : Chatbots and Face, Object, and Speech Recognition With TensorFlow and Keras*, pages 115–126. Apress, Berkeley, CA.

Maron, J., Anagnostos, D., Brodbeck, B., and Meyer, A. (2022). Artificial intelligence-based condition monitoring and predictive maintenance framework for wind turbines. *Journal of Physics: Conference Series*, 2151(1):012007.

Marugán, A. P., Márquez, F. P. G., Perez, J. M. P., and Ruiz-Hernández, D. (2018). A survey of artificial neural network in wind energy systems. *Applied Energy*, 228:1822–1836.

McCulloch, W. S. and Pitts, W. (1943). A Logical Calculus of the Ideas Immanent in Nervous Activity. *The Bulletin of Mathematical Biophysics*, 5(4):115–133.

Mendler, A., Döhler, M., and Grosse, C. U. (2023). Predictive probability of detection curves based on data from undamaged structures. *Structural Health Monitoring*.

Miner, M. A. (1945). Cumulative Damage in Fatigue. *Journal of Applied Mechanics*, 12(3):A159–A164.

Mohammadi, M., Kouzani, A. Z., Bodaghi, M., Long, J., Khoo, S. Y., Xiang, Y., and Zolfagharian, A. (2024). Sustainable Robotic Joints 4D Printing with Variable Stiffness Using Reinforcement Learning. *Robotics and Computer-Integrated Manufacturing*, 85:102636.

Mosiej, R. (2023). Automation of a script for downloading SCADA data via a programming interface. Bachelor's thesis, Technical University of Munich.

Movsessian, A., García Cava, D., and Tcherniak, D. (2021). An artificial neural network methodology for damage detection: Demonstration on an operating wind turbine blade. *Mechanical Systems and Signal Processing*, 159(107766):107766.

Musial, W. D. and Butterfield, C. (1997). Using partial safety factors in wind turbine design and testing. *National Renewable Energy Laboratory (U.S.)*. Golden, Colorado.

Nayak, S. C., Misra, B. B., and Behera, H. S. (2013). Impact of Data Normalization on Stock Index Forecasting. In *International Journal of Computer Information Systems and Industrial Management Applications*.

Nguyen, L. H. and Goulet, J.-A. (2019). Real-time anomaly detection with bayesian dynamic linear models. *Structural Control and Health Monitoring*, 26(9).

Olabi, A. G., Wilberforce, T., Elsaid, K., Sayed, E. T., Salameh, T., Abdelkareem, M. A., and Baroutaji, A. (2021). A Review on Failure Modes of Wind Turbine Components. *Energies*, 14(17):5241.

Oliveira, G., Magalhães, F., Cunha, Á., and Caetano, E. (2018). Continuous dynamic monitoring of an onshore wind turbine. *Engineering Structures*, 164:22–39.

Ordouei, M., Broumandnia, A., Banirostam, T., and Gilani, A. (2024). Optimization of energy consumption in smart city using reinforcement learning algorithm. *International Journal of Nonlinear Analysis and Applications*, 15(1).

Osterminski, K. and Gehlen, C. (2018). Echtzeitmodellierung der Ermüdung von Windenergieanlagentürmen. In *59. Forschungskolloquium und 6. Jahrestagung des DAfStb*.

Ozbek, M. and Rixen, D. J. (2013). Operational modal analysis of a 2.5 MW wind turbine using optical measurement techniques and strain gauges. *Wind Energy*, 16(3):367–381.

Pal, S. K., Mishra, D., Pal, A., Dutta, S., Chakravarty, D., and Pal, S. (2022). *Digital Twin – Fundamental Concepts to Applications in Advanced Manufacturing*. Springer Cham.

Pandey, A. K., Biswas, M., and Samman, M. M. (1991). Damage detection from changes in curvature mode shapes. *Journal of Sound and Vibration*, 145(2):321–332.

Parisi, F., Sangiorgio, V., Parisi, N., Mangini, A. M., Fanti, M. P., and Adam, J. M. (2023). A new concept for large additive manufacturing in construction: tower crane-based 3D printing controlled by deep reinforcement learning. *Construction Innovation*, 24(1):8–32.

Partovi-Mehr, N., Branlard, E., Bajric, A., Liberatore, S., Hines, E. M., and Moaveni, B. (2022). Sensitivity of Modal Parameters of an Offshore Wind Turbine to Operational and Environmental Factors: A Numerical Study. Technical report, National Renewable Energy Lab.(NREL), Golden, CO (United States).

Phillips, J. M. (2021). Gradient descent. In *Mathematical Foundations for Data Analysis*, page 125–142. Springer, Cham.

Puruncajas Maza, B. (2024). *Detection and diagnosis of faults and damage in wind turbines*. PhD thesis, Universitat Politècnica de Catalunya.

Qiangqiang, S., Huijun, Q., and Meng, C. (2014). Transmitting Systems Dynamics in SCADA using Uneven Sampling/ Cubic Spline Interpolation based Data Compression. *The Open Electrical & Electronic Engineering Journal*, 8(1):544–551.

Rabczuk, T. and Bathe, K.-J., editors (2023). *Machine Learning in Modeling and Simulation: Methods and Applications*. Springer Cham.

Raith, M., Grosse, C. U., and Kränkel, T. (2015). Pullout Experiments on Bonded Anchors Monitored via Acoustic Emission Techniques. In *31st Conference of the European Working Group on Acoustic Emission (EWGAE)–We*, volume 3, pages 1–6.

Rooij, R. (2001). *Terminology, Reference Systems and Conventions*. Duwind.

Ruder, S. (2016). An overview of gradient descent optimization algorithms. *ArXiv*, abs/1609.04747.

Rumelhart, D. E., Hinton, G. E., and Williams, R. J. (1986). Learning representations by back-propagating errors. *Nature*, 323(6088):533–536.

Rupfle, J., Emiroglu, A., and Grosse, C. U. (2022). Investigation of the Measurability of Selected Damage to Supporting Structures of Wind Turbines. *Journal of Physics: Conference Series*, 2151(1):012008.

Rupfle, J. and Grosse, C. U. (2023). Soft real-time framework for Structural Health Monitoring of wind turbine supporting structures. In *International Conference on NDE 4.0*, Berlin, Germany. .

Rupfle, J., Neffa, P., and Grosse, C. (2025). Development of a minimalistic smart sensor system for motion measurement of wind turbine towers. In Kohl, H., Seliger, G., Dietrich, F., and Mur, S., editors, *Sustainable Manufacturing as a Driver for Growth*, pages 774–781, Cham. Springer Nature Switzerland.

Rupfle, J., Wondra, B., and Grosse, C. U. (2023). Long-Term Multiple Sensor Monitoring of a Hybrid Tower Wind Turbine – Lessons Learned. In *Lecture Notes in Civil Engineering*, pages 539–549. Springer, Cham.

Rupfle, J., Wondra, B., and Nowack, M. (2024). Operational Sensor Adjustment for Structural Health Monitoring Systems in Wind Turbines. *Research and Review Journal of Nondestructive Testing (ReJNDT)*.

Russell, S. and Norvig, P. (2021). *Artificial Intelligence, Global Edition A Modern Approach*. Pearson Deutschland.

Rzepka, A. and Ziaja, D. (2024). Using the DIC Technique in Damage Detection for a Cantilevered Composite Beam. *Research and Review Journal of Nondestructive Testing (ReJNDT)*.

Sak, H., Senior, A., and Beaufays, F. (2014). Long Short-Term Memory Based Recurrent Neural Network Architectures for Large Vocabulary Speech Recognition. *arXiv*.

Sammut, C. (2017). *Encyclopedia of Machine Learning and Data Mining*. Springer New York, NY.

Schill, F. and Eichhorn, A. (2016). Investigations of low-and high-frequency movements of wind power plants using a profile laser scanner. In *Proceedings of the 3rd Joint International Symposium on Deformation Monitoring (JISDM)*.

Sepasgozar, S. M. E. (2021). Differentiating Digital Twin from Digital Shadow: Elucidating a Paradigm Shift to Expedite a Smart, Sustainable Built Environment. *Buildings*, 11(4):151.

Sewdien, V., Preece, R., Torres, J. R., Rakhshani, E., and van der Meijden, M. (2020). Assessment of critical parameters for artificial neural networks based short-term wind generation forecasting. *Renewable Energy*, 161:878–892.

Sharma, L. and Garg, P. (2021). *Artificial Intelligence: Technologies, Applications, and Challenges*. Chapman and Hall/CRC.

Singh, M., Fuenmayor, E., Hinchy, E., Qiao, Y., Murray, N., and Devine, D. (2021). Digital Twin: Origin to future. *Applied System Innovation*, 4(2):36.

Smyrnaios, M., Schn, S., and Liso, M. (2013). Multipath Propagation, Characterization and Modeling in GNSS. In *Geodetic Sciences - Observations, Modeling and Applications*. InTech.

Takasu, T. and Yasuda, A. (2009). Development of the low-cost RTK-GPS receiver with an open source program package RTKLIB. In *International symposium on GPS/GNSS*, volume 1, pages 1–6. International Convention Center Jeju Korea Seogwipo-si, Republic of Korea.

Tejada, A. (2009). A Mode-Shape-Based Fault Detection Methodology for Cantilever Beams. Technical report, CR-2009-215721: NASA.

Teunissen, P. J. G. and Verhagen, S. (2008). GNSS Ambiguity Resolution: When and How to Fix or not to Fix? In *VI Hotine-Marussi Symposium on Theoretical and Computational Geodesy*, pages 143–148, Berlin, Heidelberg. Springer.

Theisen, J. (2023). Design and implementation of a central data collection and visualization system for a multi sensor wind turbine monitoring system. Bachelor's thesis, Technical University of Munich.

Traphan, D., Herráez, I., Meinlschmidt, P., Schlüter, F., Peinke, J., and Gülker, G. (2018). Remote surface damage detection on rotor blades of operating wind turbines by means of infrared thermography. *Wind Energy Science*, 3(2):639–650.

Valente, D. S. M., Momin, A., Grift, T., and Hansen, A. (2020). Accuracy and precision evaluation of two low-cost RTK global navigation satellite systems. *Computers and Electronics in Agriculture*, 168(105142):105142.

Vallabhaneni, V. and Maity, D. (2011). Application of Radial Basis Neural Network on Damage Assessment of Structures. *Procedia Engineering*, 14:3104–3110.

Verhagen, S. (2015). GNSS ambiguity resolution and validation. In *Encyclopedia of Geodesy*, pages 1–4. Springer, Cham.

Wagg, D. J., Worden, K., Barthorpe, R. J., and Gardner, P. (2020). Digital Twins: State-of-the-Art and Future Directions for Modeling and Simulation in Engineering Dynamics Applications. *ASCE-ASME Journal of Risk and Uncertainty in Engineering Systems, Part B: Mechanical Engineering*, 6(3).

Wang, T. and Liu, Z. (2021). Digital Twin and Its Application for the Maintenance of Aircraft. In *Handbook of Nondestructive Evaluation 4.0*. Springer, Cham.

Welch, G., Bishop, G., et al. (1995). An Introduction to the Kalman Filter. *Proc. Siggraph Course*, 8.

Wielgosz, P., Kashani, I., and Grejner-Brzezinska, D. (2005). Analysis of Long-Rang Network RTK during Severe Ionospheric Storm. *Journal of Geodesy*, 79(9):524–531.

Wondra, B., Botz, M., and Grosse, C. U. (2016). Wireless monitoring of structural components of wind turbines including tower and foundations. *Journal of Physics: Conference Series*, 753:072033.

Wondra, B., Rupfle, J., Emiroglu, A., and Grosse, C. U. (2023). Analysis of Icing on Wind Turbines by Combined Wireless and Wired Acceleration Sensor Monitoring. In Rizzo, P. and Milazzo, A., editors, *European Workshop on Structural Health Monitoring*, pages 143–155. Springer, Cham. .

Zahid, F. B., Ong, Z. C., and Khoo, S. Y. (2020). A review of operational modal analysis techniques for in-service modal identification. *Journal of the Brazilian Society of Mechanical Sciences and Engineering*, 42(398).

Zhao, B., Xu, Z., Kan, X., Zhong, J., and Guo, T. (2016). Structural Damage Detection by Using Single Natural Frequency and the Corresponding Mode Shape. *Shock and Vibration*, 2016:1–8.

Zieger, T., Nagel, S., Lutzmann, P., Kaufmann, I., Ritter, J., Ummenhofer, T., Knödel, P., and Fischer, P. (2020). Simultaneous identification of wind turbine vibrations by using seismic data, elastic modeling and laser doppler vibrometry. *Wind Energy*, 23(4):1145–1153.

Zimmermann, S. (2022). Implementation of a real-time data analysis environment in matlab/ simulink. Bachelor's thesis, Technical University of Munich.

Zucchet, N. and Orvieto, A. (2024). Recurrent neural networks: vanishing and exploding gradients are not the end of the story.

List of Related Publications

Publication 1

Rupfle, J., Emiroglu, A., & Grosse, C. U. (2022). Investigation of the Measurability of Selected Damage to Supporting Structures of Wind Turbines. In *Journal of Physics: Conference Series* (Vol. 2151, Issue 1, p. 012008). IOP Publishing. https://doi.org/10.1088/1742-6596/2151/1/012008

Publication 2

Rupfle, J., Neffa, P., & Grosse, C. (2025). Development of a Minimalistic Smart Sensor System for Motion Measurement of Wind Turbine Towers. In: Kohl, H., Seliger, G., Dietrich, F., Mur, S. (eds) Sustainable Manufacturing as a Driver for Growth. GCSM 2023. *Lecture Notes in Mechanical Engineering. Springer, Cham.* https://doi.org/10.1007/978-3-031-77429-4_86

Publication 3

Rupfle, J., Wondra, B., & Nowack, M. (2024). Operational Sensor Adjustment for Structural Health Monitoring Systems in Wind Turbines. Frontiers in Nondestructive Testing and Evaluation: Academic Insights (2022/23). *Research and Review Journal of Nondestructive Testing (ReJNDT).* Vol. 2. https://doi.org/10.58286/30175

Additional Related Publications

Rupfle, J., & Grosse, C. U. (2023). Soft real-time framework for Structural Health Monitoring of wind turbine supporting structures. International Conference on NDE 4.0, 24-27 October 2022 in Berlin, Germany. https://www.ndt.net/?id=27668

Wondra, B., Rupfle, J., Emiroglu, A., & Grosse, C. U. (2022). Analysis of Icing on Wind Turbines by Combined Wireless and Wired Acceleration Sensor Monitoring. In *Lecture Notes in Civil Engineering* (pp. 143–155). Springer International Publishing. https://doi.org/10.1007/978-3-031-07254-3_15

Publication 1: Investigation of the Measurability of Selected Damage to Supporting Structures of Wind Turbines

Rupfle, J., Emiroglu, A., & Grosse, C. U. (2022). Investigation of the Measurability of Selected Damage to Supporting Structures of Wind Turbines. In *Journal of Physics: Conference Series* (Vol. 2151, Issue 1, p. 012008). IOP Publishing. `https://doi.org/10.1088/1742-6596/2151/1/012008`

This study investigates the measurability of specific damage types in hybrid wind turbine towers consisting of a prestressed concrete section with a steel upper part. Two failure cases are central. Missing pretension of tendons and fatigue-related reduction of Young's modulus in reinforced concrete. These damages affect the tower's stiffness, natural frequencies, damping, and mode shapes, making them potentially detectable through condition monitoring.

A comprehensive measurement setup was implemented on a test facility, combining acceleration sensors, strain gauges, fiber-optic systems, tilt sensors, an RTK module, and seismometers across different tower levels. Data from these sensors, particularly during UCEs, are synchronized and calibrated. Dynamic displacements are calculated through frequency-domain integration of acceleration data, while static forces, separated into mass- and thrust-induced components, are derived from strain measurements and used as input for simulations.

A FE simulation model replicates the tower's behavior, including realistic material properties and prestressing effects. Virtual sensors within the model generate comparable datasets for both undamaged and damaged states. Parametric studies simulate tendon relaxation and concrete fatigue, revealing measurable frequency shifts, especially at advanced damage stages.

The results show that the enhanced sensor configuration captures direction-dependent stiffness changes and enables detection of prestress loss and concrete degradation. The methodology's reproducibility, validated by comparing vibration-based, RTK-based, and force-based simulations, supports its suitability for predictive maintenance. This can extend inspection intervals, reduce downtime, and improve wind turbine availability.

The author conceived the idea, developed the theory, and performed almost all of the measurements and analyses. Moreover, the author designed the experiments and analytical methods and processed the experimental data. The author interpreted and discussed the results, drafted the original manuscript, applied comments, and wrote the final version of the manuscript.

Author Contribution: Conceptualization, Methodology, Software, Data Curation, Investigation, Formal analysis, Writing - Original Draft, Writing - Review & Editing, Visualization.

WindEurope Electric City 2021 IOP Publishing
Journal of Physics: Conference Series **2151** (2022) 012008 doi:10.1088/1742-6596/2151/1/012008

Investigation of the Measurability of Selected Damage to Supporting Structures of Wind Turbines

J Rupfle[1], A Emiroglu[2], C U Grosse[1]

[1] Chair of Non-destructive Testing, Technical University of Munich, Franz-Langinger-Str. 10, 81245 Munich

[2] Chair of Structural Analysis, Technical University of Munich, Arcisstr. 21, 80333 Munich

E-mail: `johannes.rupfle@tum.de`, `grosse@tum.de`

Abstract. The present work deals with a measurability study of damage to supporting structures of wind turbines. The examined hybrid tower consists of a prestressed concrete part with an attached steel section on top. Principal focus is on developing a data preprocessing and analysis concept aiming to investigate the measurability of the two selected failure cases *missing pretension of tendons* and *fatigue based change of Young's modulus in reinforcement concrete*. A simulation deduced out of real world mass and thrust forces provides a comparison with measured data based tower displacements, natural frequencies and mode shapes. The measurability of given deviations is investigated by means of virtual sensors, derived from the measurement setup of a test facility measuring acceleration, velocity, displacement and strain on different positions of the wind turbine tower, aiming the development of detection methods of such cases of damage for condition monitoring systems. The simulation input can be given by strain-based external forces or vibration-based displacements.

1. Introduction

Condition Monitoring has established itself in the past years as an instrument for damage detection. The project *IM Wind* as well as the previous project *MISTRALWIND* are focused on long-term monitoring of wind turbines [1]. The present work is concerned with measurement techniques for the detection of damage to the supporting structures of wind turbines. Using a construction plan and statics based model, the measurability of missing pretension of tendons and fatigue based change of Young's modulus in reinforcement concrete as failure cases influencing Eigenfrequencies, damping values and mode shapes is discussed.

A comprehensive literature research and reflected discussions with experts led to a number of possible damages to supporting structures of wind turbines. An overview of all considered damages is given in figure 1. In case of the within the framework of the project equipped hybrid tower, damage is mainly concentrated on connecting elements [2] [3]. A group of experts around the IM Wind Project carried out a final selection of the damage cases to be considered in the evaluation.

As the hybrid tower consists of a prestressed concrete part, tendons are used to avoid stress in reinforcement concrete to avoid damage. The pretensioning force is adjusted with a hydraulic

WindEurope Electric City 2021 IOP Publishing
Journal of Physics: Conference Series **2151** (2022) 012008 doi:10.1088/1742-6596/2151/1/012008

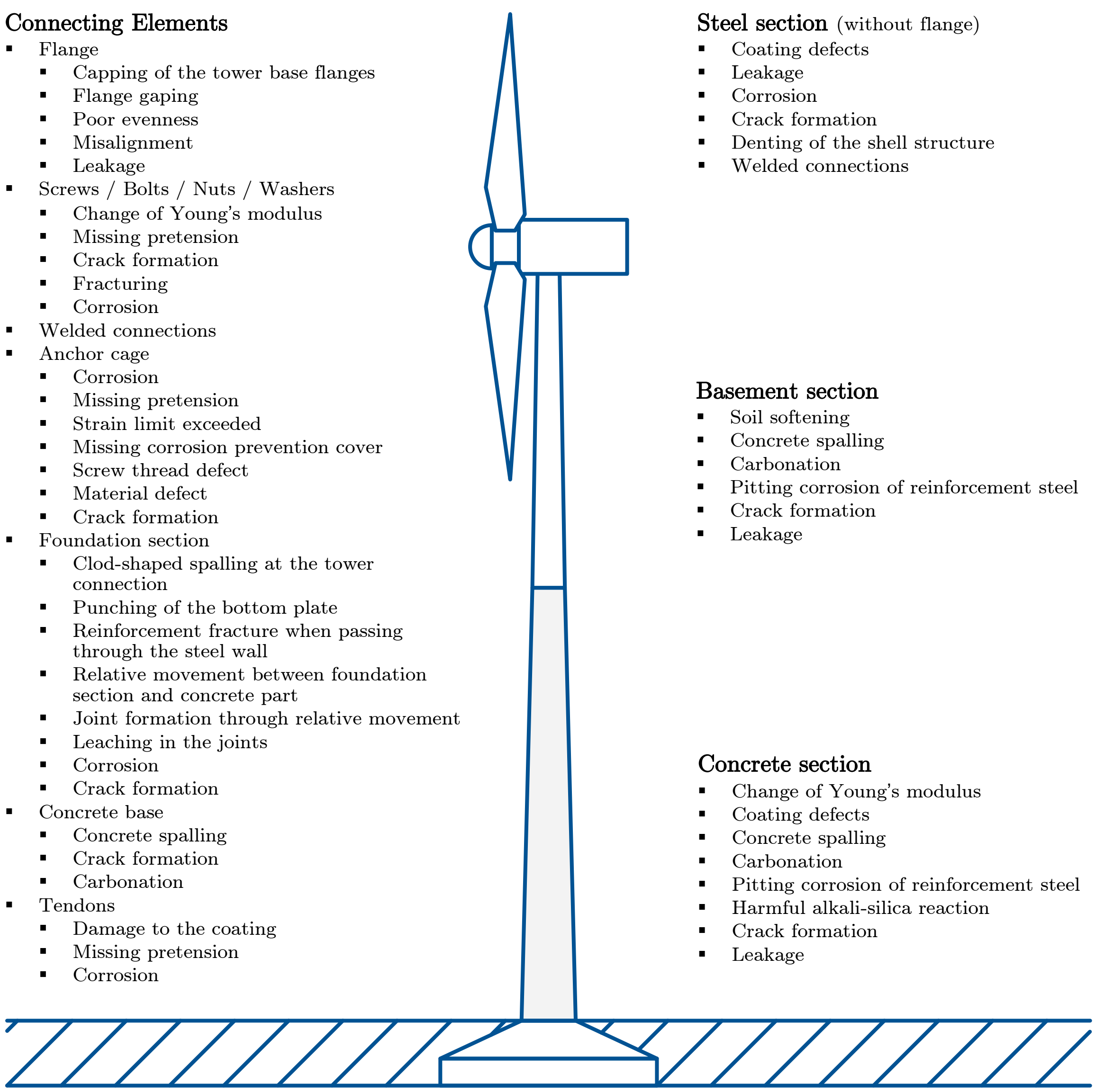

Figure 1. Possible damage considered in the evaluation process divided into subsections.

press and must be checked at regular intervals. Since a missing prestressing force will have a direct effect on the overall stiffness of the tower, it can be assumed that this can be recorded by measuring techniques.

Furthermore, degradation of reinforced concrete is investigated. As examined by Musiał [4] and Owen [5], the Young's modulus of reinforced concrete can be determined by measuring the Eigenfrequencies. Vibrational data can be used to monitor small changes in stiffness of reinforced concrete associated with slow degradation under cyclic load.

To gain knowledge about the measurability of damage in form of a reduced prestressing force, acceleration measurements of an equipped wind turbine are compared to simulation data based on mass and thrust forces derived from strain measurements combined with Supervisory Control and Data Acquisition (SCADA) data.

WindEurope Electric City 2021 IOP Publishing
Journal of Physics: Conference Series **2151** (2022) 012008 doi:10.1088/1742-6596/2151/1/012008

An essential element of the presented data preprocessing procedure is the Untwisting Cable Event (UCE) of a wind turbine. In this event, the twisted cable bundle in the tower of the turbine is untwisted to prevent damage. This specific condition is used to calibrate and synchronize measurement equipment.

2. Measurement Setup

The test facility is equipped with a variety of different measurement instruments to allow testing and validation of various approaches to a condition monitoring system and to investigate their accuracy. The sensors are distributed over five levels from the foundation up to the top of nacelle. All sensor axes are converted to a tower-fixed cylindrical coordinate system x-y-z by means of composed elemental rotations with an intrinsic sequence X-Y'-Z''.

The main concept of the condition monitoring system is based on acceleration measurements, distributed over a height from 0 m to 139 m. They are complemented by strain gauges at heights of 81 m and 139 m, which are paired with temperature sensors. In addition to the strain gauges, a fiber optic measurement system with a total of eleven distributed strain and temperature sensors is located in the tower base area. A further seismometer is also located in the tower base. Tilt sensors are installed in the tower base and at a height of 139 m. In addition, a Real Time Kinetic (RTK) module is located on top of the nacelle, which provides a maximum resolution in the centimeter range and data with a sampling rate of 14 Hz. As the MISTRALWIND project shows, the Eigenfrequencies of the tower as well as from the rotor blades and influences of the rotor speed can be determined using measured data and used for further analysis [6]. The investigation of Botz et al. shows stabilization diagrams of different states of the turbine during a maintenance event. Stable poles are identified and their deviation during the maintenance event are analyzed. The setup is used for long-term monitoring of the structure and serves many research groups as a data basis for their investigations.

To better understand the movements of the tower, it is useful to be able to specify the displacement over the tower height. This cannot be precisely achieved based on acceleration measurements alone, since the double integration of the measured data represents an initial value problem and offset leads to accumulation of integration error. Values of the unknown function at a given point in the domain can be made available by additional sensors. For future research, RTK module on top of the nacelle can be used to provide an estimation of the displacement of nacelle and can be supplemented by a tilt sensor located near the upper acceleration sensor at 139 m. Knowing the displacement and inclination, the accelerometer can be complemented precisely at this point. Figure 2 illustrates the first four bending mode shapes of the tower, that can be observed using accelerometers. The first bending mode can be determined by one single accelerometer as there is an antinode located at the top of the tower. The second, third and fourth bending modes have nodes around the top location of the tower which makes it difficult to detect them with a single sensor.

3. Data Processing

In order to assess the measurability of damage, it is required to carry out an analysis with a real world load spectrum. Main focus of this section is on the challenges associated with the derivation of a load spectrum and the methods used to address them. A general workflow is developed that allows for data-driven simulation of damage cases. An approach is presented that separates the tower displacement calculation into three distinct components. The basic approach is the calculation of dynamic tower displacement using vibrational data. The application of ultra low frequency vibrational sensors with an ultra low noise density of 0.7 µg/Hz to 1.2 µg/Hz enables the determination of even lower frequency measurements up to the first bending

WindEurope Electric City 2021 IOP Publishing
Journal of Physics: Conference Series **2151** (2022) 012008 doi:10.1088/1742-6596/2151/1/012008

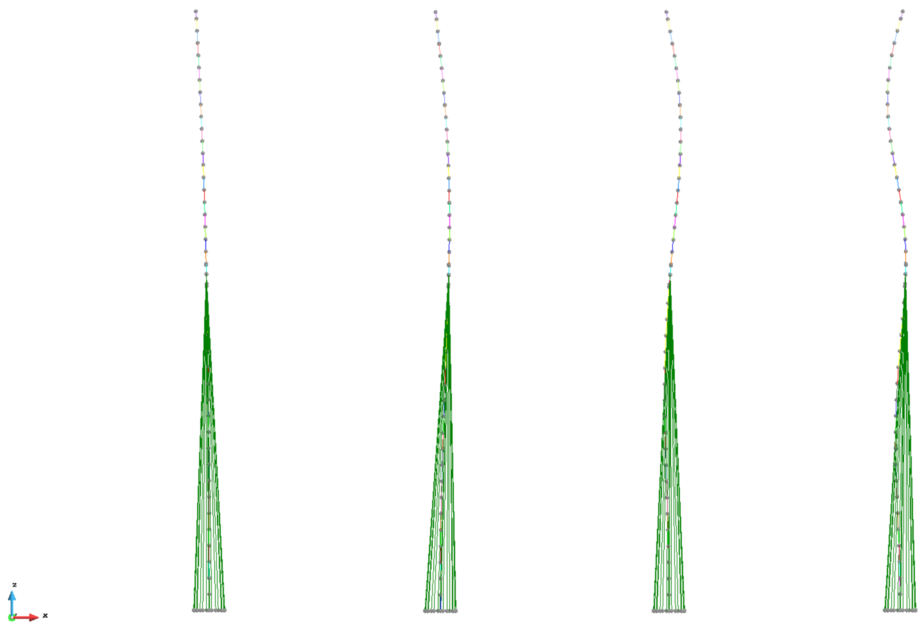

Figure 2. First four bending mode shapes of the tower finite element model.

eigenfrequency at around 0.27 Hz and a further combined natural frequency around 0.23 Hz. Furthermore, the static displacement of the tower, separated into mass induced and thrust force based displacement, is obtained from processed strain measurement data.

Figure 3 depitcs the seperation of static and dynamic displacements at 0.1 Hz which is below all known Eigenfrequencies of this specific wind turbine. To the extent known, below the first natural bending frequency of the tower, only resulting eigenmodes are found, which originate from the rotor speed in operation [6]. As the speed range lies within 7 RPM to 14 RPM, corresponding natural frequencies vary within a range of 0.11 Hz and 0.23 Hz.

In the present research work, the calculation of forces and displacement is based entirely on acceleration and strain measurements and is dealt with in section 3.3 and 3.4. An additional improvement through sensor data fusion is part of future research. An overview of possible combinations is given in section 3.5.

Furthermore, this section covers the required data pre-processing in form of measurement system synchronization in 3.1 and measurement based sensor calibration in 3.2.

3.1. Synchronization

Synchronization of datasets from different sources is an important task for further analysis. Centralized, real-time data gathering with a unique timestamp is always strongly recommended. Application Programming Interfaces (API) of state-of-the-art measurement systems provide for real time data exchange at extremely high sampling rates. If no direct communication is possible, data must be synchronized using alternative techniques. Network Time Protocol (NTP) synchronization is a wide spread and robust method. A further improvement with accuracies up to sub-microsecond range [7] and minimal network and local clock computing resources is the use of Precise Time Protocol (PTP). Independently operating systems require alternative methods such as corresponding measurement signals.

WindEurope Electric City 2021 IOP Publishing
Journal of Physics: Conference Series **2151** (2022) 012008 doi:10.1088/1742-6596/2151/1/012008

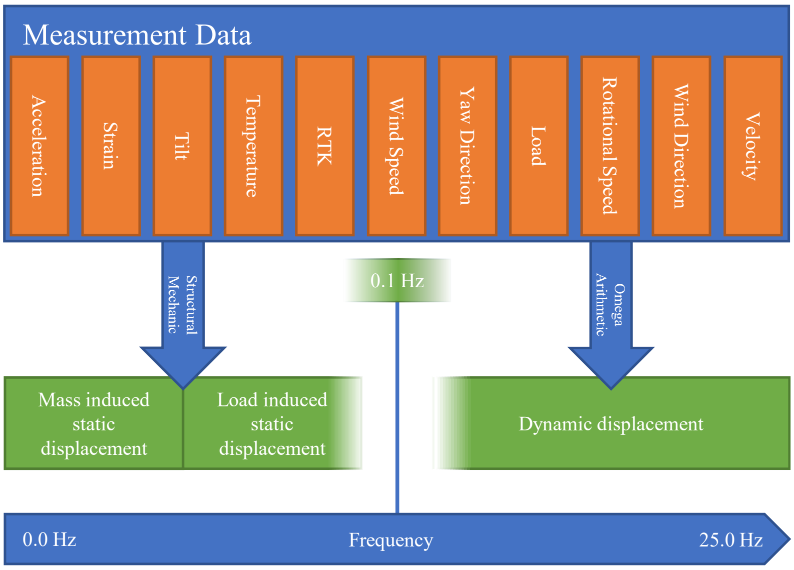

Figure 3. Data processing workflow

Due to the just recently established data interface between SCADA system and the edge controller, historical data requires alternative synchronization, since the timestamps diverge significantly at some points.

Using UCEs with their high repeatability results in precisions ranging up to milliseconds, depending on all other influencing factors. The yaw system of the test facility consists of eight electric gear motors that induce high momentum to supporting structures that further induces high shear stress to the tower due to the large mass moment of intertia of the rotor. Analysis of measurement signals revealed, that shear strain sensors detect a unique pattern of yaw drives starting up. SCADA status messages indicate the exact start of a UCE and are therefore suitable for pattern recognition. A representative pattern, extracted from measurement data is used for recognition using cross-correlation. Due to a duration of the UCE of more than 660 seconds, the extracted pattern is 320 seconds long to ensure viability and precision of detection of start of nacelle movement.

Figure 4 (a) describes yaw direction during an UCE and expected position of extracted and pre-processed shear strain pattern at the beginning of nacelle movement. All strain data are filtered with a high pass filter with a cutoff frequency of 0.1 Hz. Figure 4 (b) shows the acutal position of nacelle movement start in measurement data indicated with a black vertical line. Figure 4 (c) illustrates the aligned position of shear strain pattern due to normalized cross-correlation function shown in figure 4 (d).

3.2. Measurement based sensor calibration and position determination

Because measurement accuracy is highly dependent on the sensor calibration, it is important to ensure proper calibration. A calibration certificate typically specifies sensitivity, frequency response, and offset of a sensor. This section demonstrates, as an example, the measurement-based recalibration of strain sensors using an UCE. The combined rotor and nacelle mass causes a static moment on the tower due to its center of gravity, resulting in strain that rotates with the nacelle position. During a UCE, the pitch angle is approximately 90°, allowing the assumption that the thrust force is low. If this is completely neglected because the wind speed is very low,

WindEurope Electric City 2021 IOP Publishing
Journal of Physics: Conference Series **2151** (2022) 012008 doi:10.1088/1742-6596/2151/1/012008

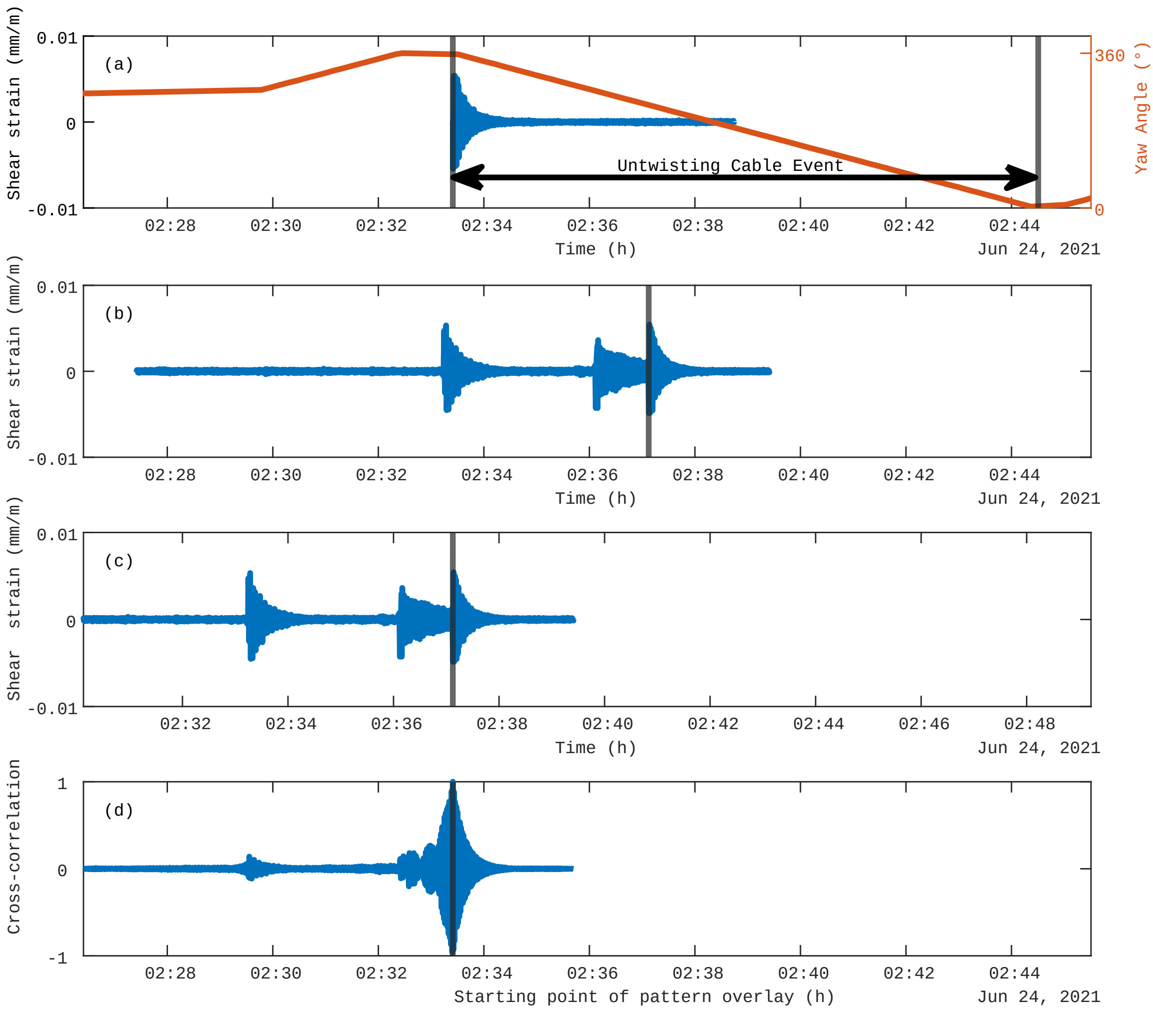

Figure 4. Data synchronization method using shear strain pattern recognition.
(a) Isolated and processed representative shear strain pattern of untwisting cable event (blue) and yaw angle (orange). Arrow indicates duration of UCE.
(b) Highpass filtered shear strain measurement. Horizontal line indicates start of UCE.
(c) Aligned shear strain measurement. Horizontal line indicates start of UCE.
(d) Normalized cross correlation of measurement data and representative pattern.

only static inertia forces impact the tower. The strain profile of a sensor is then represented by a sinusoidal function of the form represented by equation 1. The parameter indicate amplitude ($a = \frac{\epsilon_{max}-\epsilon_{min}}{2}$), period ($b = 1$, as period is equal to 2π), strain gauge position as phase ($c = \alpha$, related to a clockwise rotation from true north in radians) and strain offset ($d = \frac{\epsilon_{max}+\epsilon_{min}}{2}$).

$$f(\theta, a, b, c, d) = a * cos(b * \theta + c) + d \tag{1}$$

Applying curve fitting by means of sum of squared residuals (S) as given in equation 2, leads to strain data during an UCE and thus to parameters a to d by minimizing S as the residual is given by $r_i = f(t) - f(\theta, a, b, c, d)$. Optimization is then performed using a derivative-

WindEurope Electric City 2021 IOP Publishing
Journal of Physics: Conference Series **2151** (2022) 012008 doi:10.1088/1742-6596/2151/1/012008

free optimization algorithm. Figure 5 shows optimized model to an unprocessed real data set. Accuracy satisfies tolerance on function value of $1e^{-6}$.

The applied method can also be used to determine sensitivity, offset and position of accelerometers and tilt sensors as combined rotor and nacelle mass has a great influence on their horizontal axes as the influence of gravity is given by $sin(\alpha) * g$.

$$S = \sum_{i=1}^{n} (\epsilon(t) - f(\theta, a, b, c, d))_i^2 \tag{2}$$

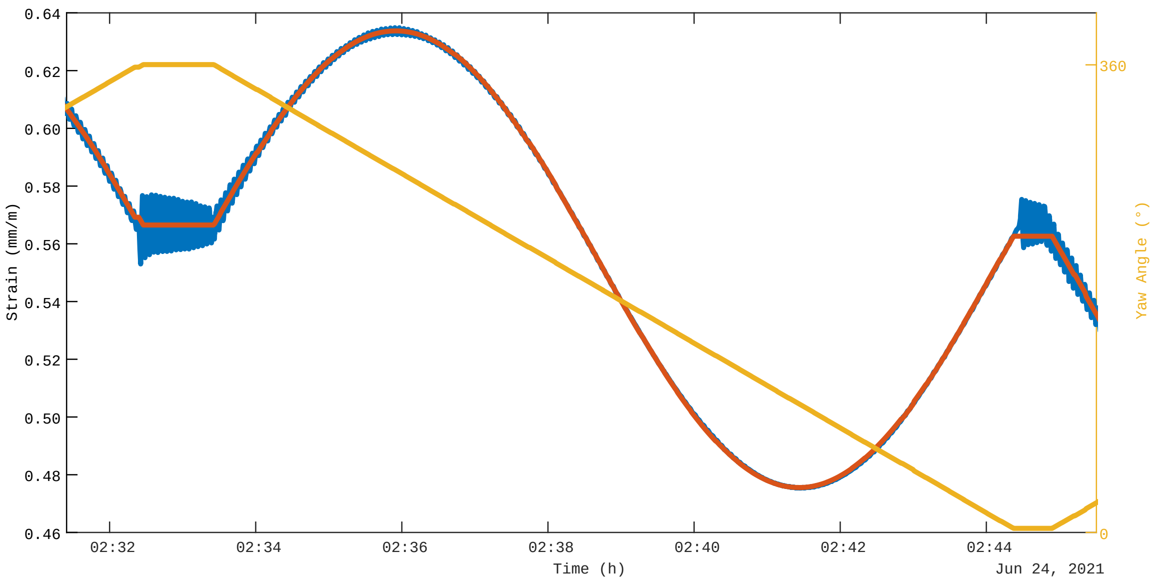

Figure 5. Comparison of unprocessed strain measurement (blue), optimized normal strain model (orange) with parameters $a = 0.079$, $b = 1.000$, $c = 81.053$ and $d = 0.555$ and yaw direction (yellow) during UCE.

3.3. Force calculation

Static forces (< 0.1 Hz) are calculated using strain measurements. The strain is considered separately as the strain due to mass and the strain due to the thrust of the wind turbine. The first can be modeled using the parameterized model from equation 1. Subtracting mass induced strain from measured strain values leads to thrust based strain values. Both static strain components are then used to pure bending moment as $M_b = E * \epsilon_R * S$, where E, ϵ_R and S are Young's modulus, strain and section modulus. Forces are calculated according to $F = \frac{M_b}{h}$, where h represents the distance of strain gauges from hub height.

3.4. Dynamic displacement calculation

Calculation of displacement through acceleration data can be performed time discrete using a cumulative trapezoidal numerical integration or can be performed as frequency domain integration. In terms of real and noisy data, integration in frequency domain tends to be the more precise and reliable way of calculating displacement from acceleration measurement in practical application as stated in [8]. Direct integration in time domain causes drifts due to

WindEurope Electric City 2021 IOP Publishing
Journal of Physics: Conference Series **2151** (2022) 012008 doi:10.1088/1742-6596/2151/1/012008

offset in acceleration or random noise. A method to overcome this issue is proposed by Yang [9] and estimates a mean of upper and lower envelope to correct data.

The present investigation focuses on integration in frequency domain. A general workflow of the application of omega arithmetic, as this method is also referred to, is described in [10]. The practical implementation of the algorithm is inspired by [11].

For the present data set, the frequency range between 0.1 Hz and 25 Hz is considered. Filter parameter of high pass filter to eliminate DC components are set to a stop band frequency of 0.1 Hz and a stop band attenuation of 80 dB. Moreover, a tapered cosine window with a coverage of 4 % of data set is applied.

3.5. Uncertainty quantification

In addition to the systematic and random errors that always appear, the measurements and analysis are subject to specific inaccuracies.

Synchronization of measurement data with SCADA data strongly depends on resolution of the yaw angle. Typically, SCADA data is not subject to a fixed cycle rate, but is event-triggered. As a result, the value is refreshed in response to a specified absolute or relative value change. With respect to synchronization, linear interpolation leads to unacceptable interpolation uncertainty. An interpolation scheme using previous values significantly reduces the error. Taking advantage of the fact that the yaw drives operate at a fixed speed, an advanced interpolation method can be applied. By determining the angular velocity of the nacelle using an UCE, a backwards interpolation with a fixed gradient can be implemented. Figure 6 compares different interpolation methods of low-resolution SCADA data. In the range from 12:47:15 to 12:47:45 it can be observed that both linear and previous value interpolation scheme differs from backwards interpolation scheme. Yaw drives rotate the nacelle constantly from 234° to 250° during this period rather than with interruptions as illustrated by other interpolation methods.

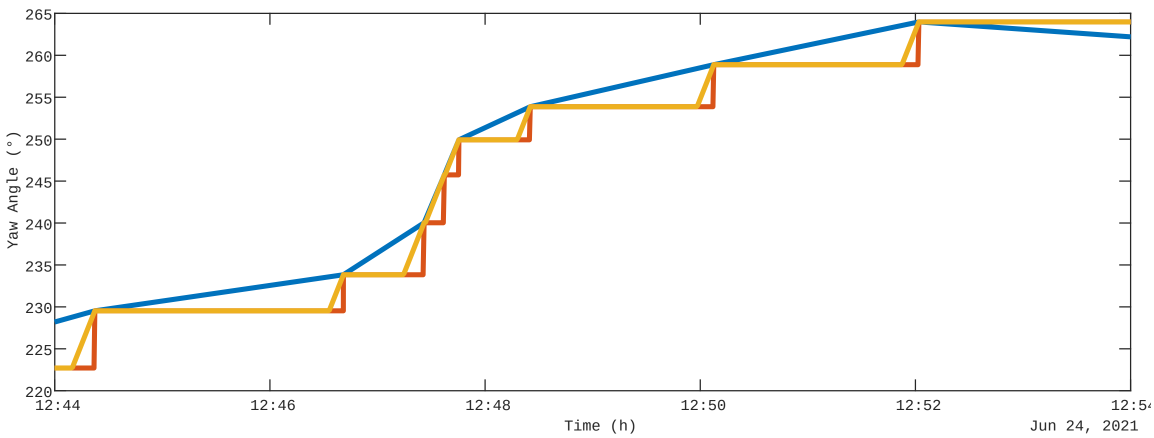

Figure 6. Comparison of untreated and linear interpolated yaw angle from SCADA data (blue), yaw angle using a previous value interpolation scheme (orange) and the developed backwards interpolation scheme with fixed gradient (yellow).

Due to tower bending mode shapes, accelerometer positions are influenced by tilt over time. The influence of tilt is given by $sin(\alpha)$ and is added to the respective horizontal axis. The compensation of these external influences by the respective sensor data alone is a challenging

WindEurope Electric City 2021 IOP Publishing
Journal of Physics: Conference Series **2151** (2022) 012008 doi:10.1088/1742-6596/2151/1/012008

task. Using the Z-axis of the sensor, which represents the vertical axis, the tilt of the sensor can be corrected only to a limited extent, since the change of the z-axis value due to the tilt angle is small $(1 - cos(\alpha))$ and is superimposed by noise. The ratio of the deviations in x/y and z direction is described by $\frac{sin(\alpha)}{1-cos(\alpha)}$. Figure 7 shows both normalized deviations and the resulting ratio. A tilt angle of 0.5° results in a deviation ratio of 229.2. This ratio, being large for small angles, and the superposition by noise do not allow correction of the sensor data by using the corresponding z-axis. Supplementing the influenced acceleration measurement with an inclination sensor, RTK or even both can significantly improve the acceleration and thus calculated displacement results.

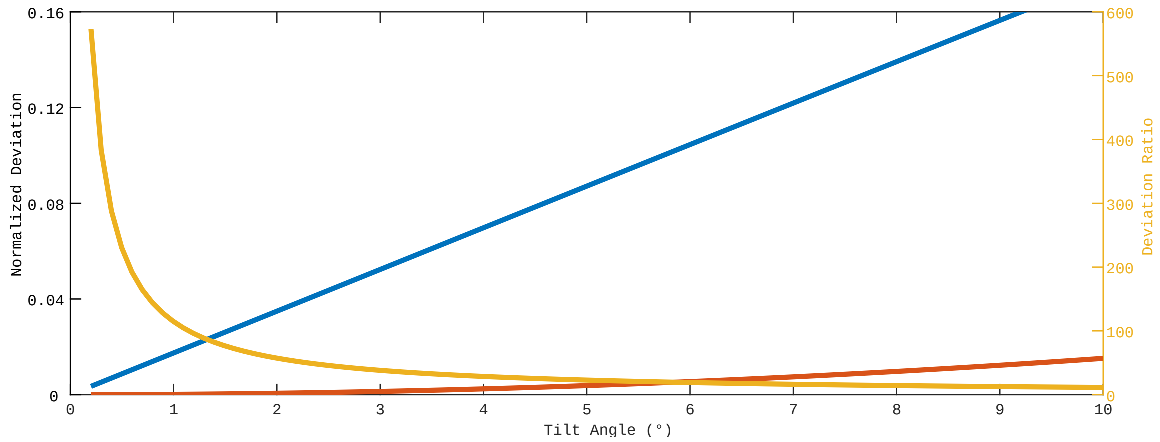

Figure 7. Resulting normalized deviations of x-y-axis (blue), z-axis (orange) due to tilt angle and resulting deviation ratio (yellow).

Furthermore, parametrization of the model developed in section 3.3 for mass induced strain determination is only as precise as wind influences can be excluded. Due to the applied curve fitting algorithm, short wind gusts only have a negligible influence. However, a constant wind has an effect on the parameter and particularly on d, i.e., the sensor offset, and thus influences the absolute calculated values. The number of usable UCEs is noticeably reduced by the fact that rotating winds triggering such an event are often associated with high air flow rates.

4. Simulation Model

The simulation model is achieved by first constructing a CAD model using linear geometrical entities for the simple representation of the tower geometry. Moreover, a Finite Element (FE) model is generated out of the prepared CAD model. The FE model contains cable elements that represent the tendons and beam elements for the modeling of the concrete and steel sections. In particular, one element per concrete and steel section is used. In addition, in order to represent the mass properties accurately, the material density at certain regions is adjusted, such as adapter piece, between the concrete and steel shaft as well as the rotor connection. This model serves as a simplification to the more detailed model that is created using shell and volume elements. The elasticity moduli of the individual reinforced concrete sections are determined by making use of the measured concrete dynamic elasticity modulus [12] and the rule of mixtures [13] in order to achieve a realistic material behavior and incorporate the effect of reinforcement steel.

WindEurope Electric City 2021 IOP Publishing
Journal of Physics: Conference Series **2151** (2022) 012008 doi:10.1088/1742-6596/2151/1/012008

Table 1. Trend of the first bending Eigenfrequency over fatigue lifetime (n) as a function of $S_{c,max} = [0.9, 0.5, 0.1]$ and $S_0 = 100\%$.

n	0.00	0.25	0.50	0.75	1.00
$f_{S_{c,max}=0.9}$	0.27477	0.27473	0.27416	0.27165	0.26452
$f_{S_{c,max}=0.5}$	0.27477	0.27477	0.27476	0.27390	0.20714
$f_{S_{c,max}=0.1}$	0.27477	0.27477	0.27477	0.27468	0.07748

A particular detail of the Eigenfrequency analysis is the incorporation of the prestresses that occur due to initial displacements that are resultants of self-weight and prestressing tendons. This can be achieved by computing the equilibrium state of the structure under the loading conditions and making use of the stiffness properties at the equilibrium state. The investigations on the initial displacement effects is investigated by Wüchner et al. in [14].

5. Failure Cases

Simulation of the two failure cases missing prestress of tendons *(case 1)* and degradation of reinforced concrete *(case 2)* is expected to result in a direction-dependent change in stiffness and damping of the whole structure. Eigenfrequencies, nodes and antinodes are expected to vary under new conditions.

A simulation with a real load spectrum is performed. The impact on the tower is recorded by measurement. The model is optimized by means of virtual sensors. After adjusting the parameters, simulation is carried out with manipulation of the tower to generate data of a damage case by means of virtual sensors.

Making use of the FE model, a selection of degradation and failure cases are considered and the eigenfrequencies of the tower structure are computed. The considered concrete material degradation cases can be listed as follows; relative fatigue lifetime $n = [0.25, 0.5, 0.75, 1.0]$, fatigue related maximum compressive stresses $S_{c,max} = [0.9, 0.5, 0.1]$. The effect of n as well as $S_{c,max}$ on the concrete elasticity modulus can be calculated using the relations from 3 [15].

$$\begin{aligned} E_c(n) &= E_{c28} * (1 - D_c(n)) \\ D_c(n) &= n^{a_c} * (1 - S_{c,max}) \\ a_c &= 26.5 - 25.0 * S_{c,max} \end{aligned} \tag{3}$$

where $E_c(n)$ is the elasticity modulus of the concrete at relative fatigue life time n, $D_c(n)$ is the concrete degradation coefficient and a_c is the exponent factor . In addition to the material degradation, the relaxation of the prestressing tendons are considered for four different cases; $S_0 = [100\%, 95\%, 90\%, 85\%]$. Table 1 shows that the initial bending eigenfrequency changes significantly towards the end of the service life. The effect is further intensified as $S_{c,max}$ decreases.

6. Conclusion

The enhanced sensor configuration can be used to determine natural frequencies by means of operational modal analysis, to determine stress states in real time and provides knowledge of direction dependent condition data of the whole structure and is thus qualified to perform a comprehensive condition monitoring for supporting structures of wind turbines.

The developed processing workflow provides direct simulation input on two different ways. On the one hand, the input can be provided by calculated static and dynamic forces at the

WindEurope Electric City 2021 IOP Publishing
Journal of Physics: Conference Series **2151** (2022) 012008 doi:10.1088/1742-6596/2151/1/012008

tower top, on the other hand, the direct input can be provided by calculated displacements. The simulation input can thus be generated based on two different measurement techniques. Comparison of both inputs serves as a validation of calculations, leads to a reconciliation of both methods and enables the continuous improvement of the techniques. Operational modal analysis revealed, that acceleration based eigenfrequencies and thrust force based simulated eigenfrequencies match each other.

Comparing vibration-based displacement, processed RTK data, and simulation data with strain measurement-based external force input, the results are remarkably reproducible. The simulation was performed with the updated beam model considering only the first bending natural frequency in two spatial directions. Figure 8 shows a period of time in which the turbine was switched off at medium wind speeds of approximately 4.4 m/s^2 and a wind direction of 315° (NW). Both acceleration and strain data indicate that only the first bending mode is excited during this period. Since the simulation time spanned a period of only 60 s, a settling time of 6 s is excluded from the analysis. The amplitudes and phases of the three independently calculated time series in Figure 8 (a) as well as the natural frequencies of Figure 8 (b) show broad agreement, so the described procedure is accurate enough and can be used for further studies.

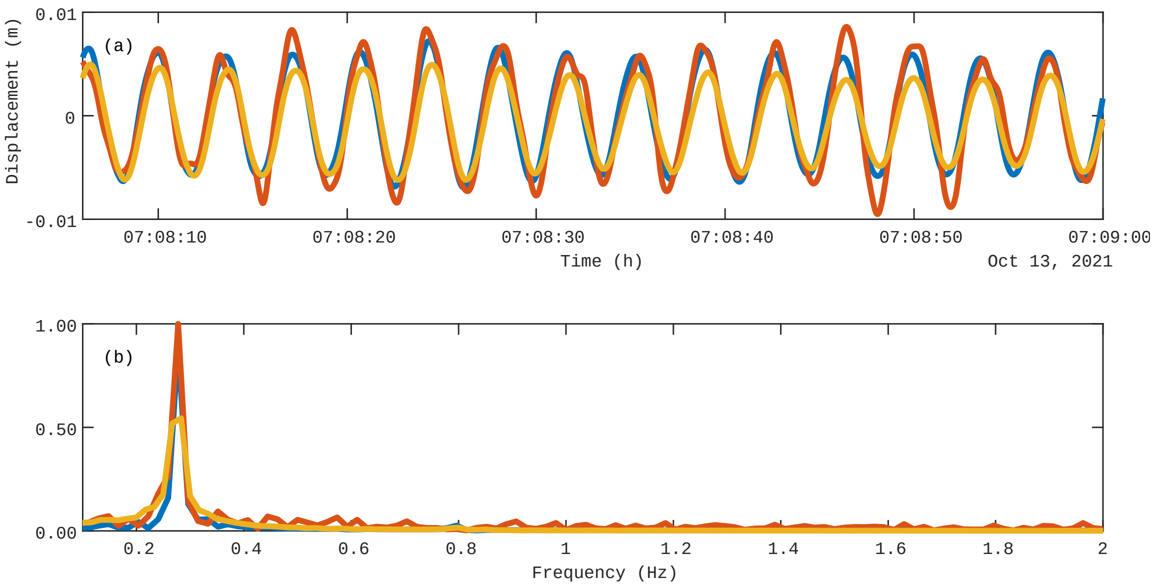

Figure 8. Comparison of dynamic displacement calculated using the three different approaches of vibration based displacement in frequency domain (blue), processed RTK data (orange), and external forces based simulated displacement (yellow)
(a) Comparison of time series.
(b) Normalized frequency spectra of the data sets with peaks at first bending Eigenfrequency of approximately 0.27 Hz.

Directional dependent data for stiffness, natural frequencies and damping can be used to determine pretensioning force of tendons and degradation of reinforced concrete and is able to extend regular maintenance intervals. This results in the capability to perform predictive maintenance, thus reducing downtime and increasing overall equipment effectiveness. A reduced

WindEuropeElectric City 2021 IOP Publishing
Journal of Physics: Conference Series **2151** (2022) 012008 doi:10.1088/1742-6596/2151/1/012008

sensor configuration can be used in future systems of condition monitoring for wind turbines to detect further damage and fatigue as well as to determine remaining service life which is part of further investigations within the project.

Acknowledgments
The authors would like to thank the German Federal Ministry for Economic Affairs and Energy for funding the project and Max Boegl and Siemens for providing access to the test facility and graduate student Alejandro Ramírez Piñero for data treatment and assistance during installation. The authors also gratefully thank the staff of Max Boegl for their support during installation of the measurement systems. Supported by TUM International Graduate School of Science and Engineering (IGSSE).

References

[1] Botz M, Emiroglu A, Osterminski K, Raith M, Wüchner R, Große C. Überwachung und Modellierung der Tragstruktur von Windenergieanlagen. Beton- und Stahlbetonbau. 2020 mar;115(5):342-54.
[2] Bellmer H. Schäden an Tragstrukturen für Windenergieanlagen. Schadenfreies Bauen. 2016.
[3] WindEnergie B. Umgang mit Schäden an Fundamenten von Windenergieanlagen. BWE Ratgeber. 2013.
[4] Musiał M, Grosel J. Determining the Young's modulus of concrete by measuring the eigenfrequencies of concrete and reinforced concrete beams. Construction and Building Materials. 2016 sep;121:44-52.
[5] Owen JS. Monitoring the Degradation of Reinforced Concrete Beams under Cyclic Loading. Key Engineering Materials. 2003 jul;245-246:307-14.
[6] Botz M, Zhang Y, Raith M, Pinkert K. Operational modal analysis of a wind turbine during installation of rotor and generator. In: 7th International Operational Modal Analysis Conference (IOMAC); 2017. .
[7] Astarloa A, Rodriguez M, Duran F, Jimenez J, Lazaro J. Synchronizing NTP Referenced SCADA Systems Interconnected by High-availability Networks. In: 2020 XXXV Conference on Design of Circuits and Integrated Systems (DCIS). IEEE; 2020. .
[8] Qihe L. Integration of Vibration Acceleration Signal Based on LabVIEW. Journal of Physics: Conference Series. 2019 nov;1345:042067.
[9] Yanli Yang DK Yanfei Zhao. Integration on acceleration signals by adjusting with envelopes. Journal of Measurements in Engineering. 2016;Vol. 4(Issue 2):p. 117-21.
[10] Jablonski A. Condition Monitoring Algorithms in MATLAB®. Springer International Publishing; 2021.
[11] E Cheynet. Converting acceleration to displacements records. Zenodo; 2020.
[12] Wondra B, Große CU, Raith M, Mayer T, Botz M. MISTRALWIND - Monitoring and inspection of structures at large wind turbines; Teilvorhaben Lehrstuhl für Zerstörungsfreie Prüfung, Arbeitspaket 4: Überwachungstopologie : Schlussbericht BMWi-Verbundprojekt : Laufzeit: 01.08.2015-31.07.2018. Report. 2018.
[13] Tam DKY, Ruan S, Gao P, Yu T. High-performance ballistic protection using polymer nanocomposites. In: Advances in Military Textiles and Personal Equipment. Elsevier; 2012. p. 213-37.
[14] Wüchner R, Osterminski K, Gehlen C, Emiroglu A, Bletzinger KU. Monitoring and inspection of structures at large wind turbines - MISTRALWIND, Teilvorhaben 5 - Lebensdauerakte Windenergieanlagentürme : Schlussbericht : Förderzeitraum 2015-2018. Report. 2019.
[15] Emiroglu A. Multiphysics simulation and CAD integrated shape optimization in fluid-structure interaction [Dissertation]. München: Technische Universität München; 2019.

Publication 2: Development of a Minimalistic Smart Sensor System for Motion Measurement of Wind Turbine Towers

Rupfle, J., Neffa, P., & Grosse, C. (2025). Development of a Minimalistic Smart Sensor System for Motion Measurement of Wind Turbine Towers. In: Kohl, H., Seliger, G., Dietrich, F., Mur, S. (eds) Sustainable Manufacturing as a Driver for Growth. GCSM 2023. *Lecture Notes in Mechanical Engineering. Springer, Cham.* https://doi.org/10.1007/978-3-031-77429-4_86

This study presents the development of a minimalistic smart sensor system for measuring wind turbine tower motion. The system combines high-resolution MEMS accelerometers, RTK positioning, and SCADA data to provide accurate motion monitoring using cost-effective, commercially available components. Installed on top of the nacelle, the setup captures dynamic response via acceleration and static position via RTK. A KF based state estimator fuses the data to enhance accuracy and avoid drift from acceleration integration.

The hardware consists of a single-board computer with modular connectivity, a three-axis MEMS accelerometer with a 20-bit ADC, and an RTK module providing sub-centimeter positioning and precise timestamps. The Python-based software framework includes a central data buffer, modular analysis functions, coordinate transformation between tower- and nacelle-fixed systems, automated offset calibration, data logger functionalities, and real-time data streaming via MQTT to a NoSQL database.

Prototype tests on a full-scale turbine show that fore-aft displacement correlates strongly with wind speed and power output, while side-side motion remains minimal. The system can be used for tower motion monitoring, damage detection, RUL assessment, and load estimation to extend the operating range under controlled conditions. Beyond wind turbines, the approach applies to other slender structures such as skyscrapers, antenna towers, bridges, and dams. Limitations are RTK sampling rate, dependency on correction data, and SCADA timing, which may be mitigated in future iterations with fallback sensors and enhanced filtering.

The author conceived the idea, developed the theory, and performed almost all of the measurements and analyses. Moreover, the author designed the experiments and analytical methods and processed the experimental data. The author interpreted and discussed the results, drafted the original manuscript, applied comments, and wrote the final version of the manuscript.

Author Contribution: Conceptualization, Methodology, Software, Data Curation, Investigation, Formal analysis, Writing - Original Draft, Writing - Review & Editing, Visualization.

Development of a Minimalistic Smart Sensor System for Motion Measurement of Wind Turbine Towers

Johannes Rupfle[1,2(✉)], Patricio Neffa[2], and Christian Grosse[1]

[1] Chair of Non-Destructive Testing, Technical University of Munich, Franz-Langinger-Str. 10, 81245 Munich, Germany
johannes.rupfle@tum.de

[2] Instituto Tecnológico de Buenos Aires, San Martín 202, 1004 Buenos Aires, Argentina

Abstract. The accurate measurement of wind turbine tower motion is crucial for assessing structural integrity, identifying damages, and estimating remaining useful life. In this study, the development of a smart sensor system is presented, which combines acceleration measurements, real-time kinematic measurements, and SCADA data to accurately determine the motion of slender structures. The proposed setup offers a cost-effective and easily deployable solution. Installed on the top of the wind turbine nacelle, the sensor system collects data to calculate the tower motion. Real-time kinematics measurements serve as correction input for a state estimator, to enhance accuracy and reliability. Data gathering and processing occur directly on the sensor node, allowing for efficient transfer. Test measurements on a wind turbine tower have demonstrated the effectiveness of the system for accurate motion measurements. Beyond wind turbine manufacturing, this sensor system holds potential for application in several domains, including tall buildings and bridges, where the detection of vibrational movements is valuable for structural health monitoring.

Keywords: sustainable manufacturing · life cycle assessment · smart sensor system · wind turbine tower motion · acceleration · real-time kinematic · damage assessment · remaining useful life · structural health monitoring · industry 4.0 · internet of things · sustainable development

1 Introduction

The rapid growth of wind energy as a sustainable power source has led to an increased demand for reliable and efficient wind turbine systems. The dynamic behavior of these tall structures, subjected to turbulent wind leads to tower vibrations and motion. Monitoring and analyzing tower motion is essential for assessing structural health, detecting potential damages, and estimating the RUL[1] of wind turbines, but may also allow extension of the overall operating range of the turbine.

[1] Remaining Useful life.

H. Kohl et al. (Eds.): GCSM 2023, LNME, pp. 774–781, 2025.
https://doi.org/10.1007/978-3-031-77429-4_86

Traditional methods for tower motion measurement involve the use of complex and expensive instrumentation, such as laser-based displacement sensors or inclinometers as in [1]. While these techniques provide accurate measurements, their high cost and limited scalability hinder their widespread implementation for large-scale wind farms. Therefore, there is a need for a cost-effective and easily deployable monitoring solution that can capture accurate and reliable tower motion data.

We propose the development of a minimalistic smart sensor system for motion measurement of wind turbine towers. The system leverages the advancements in RTK[2] positioning technology and high-resolution acceleration sensors to enable precise and continuous motion monitoring. RTK is a high-precision positioning technique that uses reference stations to provide real-time corrections to GPS5[3] signals. It achieves sub-centimeter-level accuracy by comparing satellite measurements with known reference positions. RTK is widely used in various industries for applications requiring precise and continuous positioning information, such as agriculture, construction, and autonomous vehicles. The integration of an RTK module ensures accurate static positioning, while the high-resolution acceleration sensors capture the dynamic response of the tower.

The key advantages of the proposed smart sensor system include its ease of deployment, cost-effectiveness, and compatibility with existing wind turbine infrastructure. By utilizing commercially available components and wireless communication, the system minimizes the installation and maintenance costs associated with traditional monitoring methods. The compact size and lightweight design of the sensors allow for straightforward integration into the wind turbine towers without significant modifications.

For efficient data acquisition and analysis, a custom software platform has been developed. The software synchronizes data logging but also provides more complex extraction of modal parameters, tower movement analysis, and feature extraction from SCADA6[4] events.

The contributions of this study lie in the development and validation of a minimalistic smart sensor system for motion measurement of slender structures. A prototype installed in a large-scale onshore wind turbine utilized as test facility [2] for several years provides the depicted measurement data in the course of this publication. The system provides a practical solution for sustainable manufacturing in the wind energy sector. Through continuous monitoring and analysis of tower motion, operators can make informed decisions regarding maintenance, repair, and optimization of wind turbine performance.

2 Methodology

The following section describes the concept of the smart sensor system and gives insight into the development of both hard- and software parts of the system.

[2] Real-Time Kinematics.
[3] Global Positioning System.
[4] Supervisory Control and Data Acquisition.

2.1 Sensor System Development

Platform selection: A single-board computer is used as the platform for the sensor system. This choice allows for flexibility and integration with various sensors and communication protocols. The system also provides both wired and wireless internet connection and extension modules for cellular networks. The system includes separate storage for the operating system and the file storage.

Utilization of a high-resolution sensor: A high-resolution 3-axis MEMS7[5] accelerometer is utilized. The sensor element has a built-in 20 bit ADC8[6] and a sensitivity range from ± 2 g to ± 8 g. The sensitivity of the digital output is 256, 000LSB9[7]/g. Both high-pass and low-pass filter options can be applied internally. The spectral density of noise is specified as 22.5 $\mu g/\sqrt{Hz}$. The sensor node also provides an integrated temperature sensor.

Integration of the RTK module: The RTK module provides precise positioning information and an accurate GPS timestamp that is used for synchronization purposes with potential additional systems. The sample rate is adjustable from 1 Hz to 14 Hz. Correction input can be either provided by a self-hosted base station or publicly available reference station networks.

2.2 Data Acquisition Development

Platform for data acquisition: The measurement systems data acquisition consists of a Python-based framework for the basic functional modules and the optional modules for extended analysis of the measured data, data logging, and transmission. It is intended, that the essential modules work independently from non-essential analysis modules to improve reliability.

Connectivity: The MEMS element and the RTK module of the measurement system are connected to the single-board computer via serial interfaces. The external data sources SCADA and environmental data are implemented via programming interfaces.

Implementation of external data: SCADA data such as yaw angle, rotor speed, blade angle, power output, wind speed, wind direction, and status text messages of the turbines control system are used to complement the data. A further approach is to implement weather forecast data such as wind, wind gusts, new snow, temperature, dew point, humidity, and freezing altitude into the database.

2.3 Features of the Software

The proposed software consists of a central data buffer that is fed with data from different sources. The flowchart after initialization is depicted in Fig. 1. Independent modules can

[5] Micro-Electro-Mechanical System.
[6] Analog Digital Converter.
[7] Least Significant Byte.

then access the data and are also able to return data to the buffer. Besides the state estimator module which is seen as an essential module of the software package, optional modules can be added to fulfill specific tasks such as extraction of modal parameters according to [3], or ice detection as it is developed in [4].

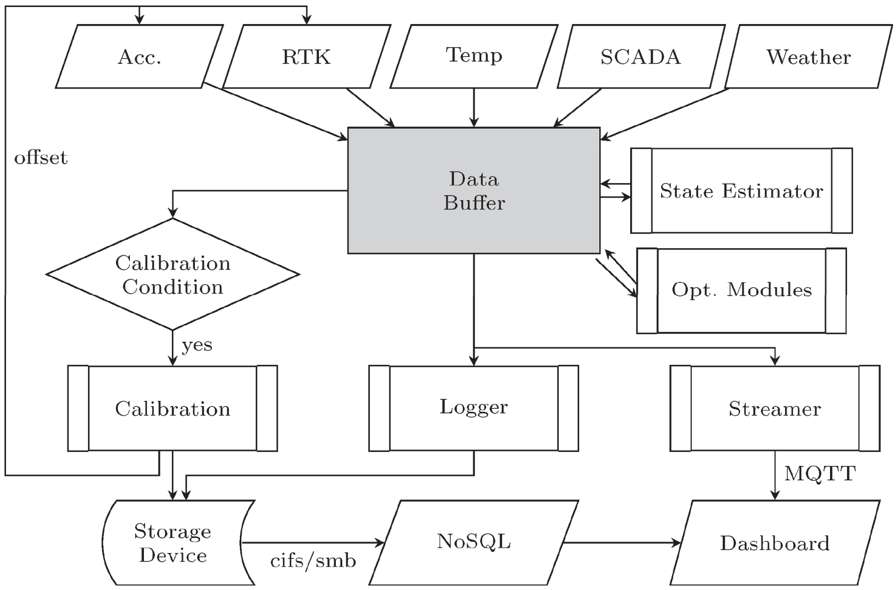

Fig. 1. Flow chart of proposed data acquisition and processing scheme.

Data acquisition with precise and unified timestamp: The clock of the system is given by the GPS module and is delivered with a precise time stamp with an accuracy of up to 30 ns, thus it is not necessary to have a real-time clock installed in the single-board computer.

State estimator: A state space model is a mathematical representation of the physical system, described by a set of differential equations known as the equations of motion. This model provides a foundation for fusing data from different measurements with different limitations to obtain a more precise estimation of the tower's state using a state estimator. The initial implementation of the state space model incorporates a Kalman filter as initially published by Kalman [5]. The Kalman filter is a recursive estimation algorithm widely used in control systems and signal processing. It optimally estimates the state of a system by combining predictions from a mathematical model (the state space model) and measurements.

Coordinate transformation: To be able to examine tower motion and modal features both in a tower fixed coordinate system but also in a nacelle fixed coordinate system, a continuous transformation between the coordinate systems is implemented. This allows for the examination of a subsequent module that analyzes direction-dependent variation of Eigenfrequencies. After simplification of the rotation matrix of the intrinsic sequence X–Y′–Z″ with the Tait-Bryan angles $\alpha = 180°$, $\beta = 0°$, and $\gamma = 0°$, respectively, the following rotation matrix $\mathbf{R}_{S\rightarrow N}$ as depicted in Eq. 1a results. For the intrinsic sequence

X–Y′−Z″ with the Tait-Bryan angles $\alpha = 0°$, $\beta = 0°$, and $\gamma = 270° - \phi$, where ϕ represents the yaw angle with positive angles for clockwise rotation from north direction, the rotation matrix $\mathbf{R}_{\mathrm{N}\to\mathrm{T}}$ as depicted in Eq. 1b results. Equally, the RTK data can be transformed into the nacelle coordinate system using the transposed rotation matrix $\mathbf{R}_{\mathrm{T}\to\mathrm{N}} = \mathbf{R}_{\mathrm{N}\to\mathrm{T}}$.

$$\mathbf{R}_{\mathrm{S}\to\mathrm{N}} = \mathbf{R}_{\mathrm{Z}}(\gamma)\mathbf{R}_{\mathrm{Y}}(\beta)\mathbf{R}_{\mathrm{X}}(\alpha)\begin{bmatrix} 1 & 0 & 0 \\ 0 & \cos(\alpha) & -\sin(\alpha) \\ 0 & \sin(\alpha) & \cos(\alpha) \end{bmatrix} = \begin{bmatrix} 1 & 0 & 0 \\ 0 & -1 & 0 \\ 0 & 0 & -1 \end{bmatrix} \tag{1a}$$

$$\mathbf{R}_{\mathrm{N}\to\mathrm{T}} = \mathbf{R}_{\mathrm{Z}}(\gamma)\mathbf{R}_{\mathrm{Y}}(\beta)\mathbf{R}_{\mathrm{X}}(\alpha) = \begin{bmatrix} \cos(\gamma) & -\sin(\gamma) & 0 \\ \sin(\gamma) & \cos(\gamma) & 0 \\ 0 & 0 & 1 \end{bmatrix} \tag{1b}$$

Automated offset determination and sensitivity tracking: Accurate measurement of wind turbine tower motion requires calibration of the sensor offset and orientation. The offset of MEMS accelerometers can arise from mechanical and electrical factors. The mechanical offset is caused by gap mismatch and residual stress, while the electrical offset is due to parasitic capacitance and electrical components [6]. Minimizing these influencing factors is crucial for precise data analysis. Additionally, determining the orientation of the sensor elements with high accuracy is essential. To achieve this, a calibration method utilizing the untwisting cable event is employed and will be discussed in future work. In [7] a method to determine both sensor offset values and relative sensitivity is proposed.

Data logger: The buffered data is logged on the local machine and securely transferred via MQTT10[8] to a central NoSQL11[9] database.

Real-time data stream: Utilization of MQTT enables real-time streaming of sensor data. This feature allows for integration with other systems and real-time motion monitoring. The MQTT performance is tested up to a sample rate of 20Hz which can be seen as the maximum RTK rate available on the market and sufficiently high resolved data for the expected Eigenfrequencies of up to 5.69Hz for the fourth bending Eigenfrequency of the tower as it was determined in [8].

Extraction of modal parameters: Modal parameters, such as natural frequencies and mode shapes, are extracted from the sensor data for structural analysis of the wind turbine tower. These parameters provide insights into the dynamic behavior and health condition of the tower. The extracted data can be clustered by operating ranges and directions to not only detect damage but also localize them.

3 Results

A measurement system prototype was installed at the tower top of the test facility with the GPS antenna on top of the nacelle.

[8] Message Queuing Telemetry Transport.
[9] Not only Structured Query Language.

Evaluation of displacement estimation: Fig. 2 presents measurement data (a–d) obtained from the RTK system (a, b) and the acceleration sensors (c, d) in the east (a, c) and north (b, d) directions. Subplots $Disp_x$ (e) and $Disp_y$ (f) illustrate the estimated displacement in the fore-aft and side-side directions of the nacelle, respectively. Subplots *Wind Speed* (g) and *Power Output* (h) display the wind speed and power output of the wind turbine. Notably, the fore-aft displacement of the turbine exhibits a direct correlation with the overall load on the tower, as evidenced by the similarities between the wind speed and power output curves and the fore-aft displacement curve in subplot $Disp_x$ (e). The power output corresponds to the thrust force leading to a tower displacement of the same order of magnitude. Conversely, the side-side displacement shows only minimal drift. Both displacement curves exhibit superimposed harmonics associated with the Eigenfrequencies of the tower and the rotor.

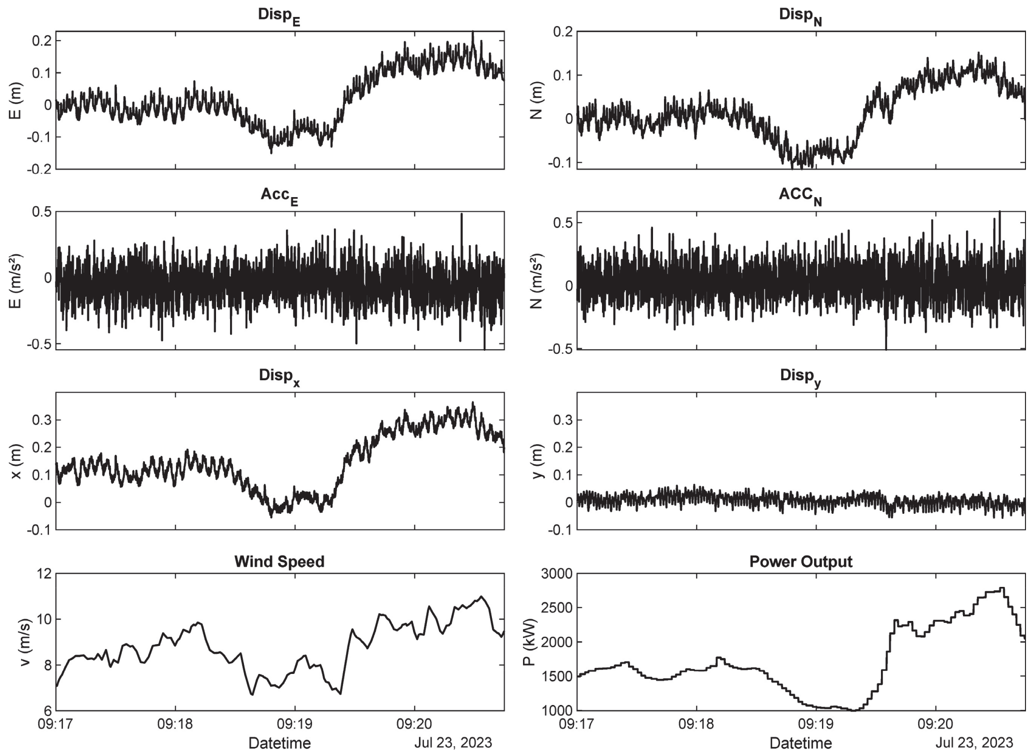

Fig. 2. Measurement results of both RTK (a, b) and acceleration (c, d) measurements and the estimated and rotated displacement in nacelle coordinates (e, f), compared with the wind speed (g) and power output (h).

Extension of operating range: An additional advantage of monitoring wind turbine tower motion lies in its potential to extend the operating range of the wind turbine. With precise estimation of the tension experienced by the tower under varying wind loads, the operational limits of the turbine can be expanded, provided that it remains within its structural safety limits. This increased flexibility allows the wind turbine to operate more efficiently across a wider range of wind speeds, leading to enhanced energy production and overall performance. As depicted in Fig. 2 (e), a notable rise in wind speed of approximately 3 m/s, from 7 m/s to 10 m/s, corresponds to an overall displacement of the tower of approximately 0.30 m. Both the static and dynamic displacements can then be employed as inputs for a finite element tower model, following the approach presented by Emiroglu et al. [9]. The resulting tensile stress can further be utilized as input for a rainflow counting algorithm, as previously developed in studies such as [10] and [11]. This comprehensive analysis enables a more accurate evaluation of the turbine's structural health and RUL.

4 Conclusion

The presented measurement system represents a significant advancement in accurately assessing tower motion. By employing a state estimator, the measurement system combines the dynamic displacement precision of acceleration measurement with the static accuracy of RTK data. Its superiority over purely vibration-based displacement calculations lies in the avoidance of drift resulting from the integration of acceleration values and thus enables precise determination of displacement of the tower.

Beyond its main use in monitoring tower motion, the system is capable of detecting damage and assessing RUL. Additionally, it can evaluate the initial state of turbines and monitor the construction phase, as resonance cases may occur at various stages of construction. Moreover, it facilitates estimation of the overall load on wind turbine supporting structures, allowing for an extended operating range under specific conditions where the cutout wind speed is already exceeded. The versatility of the system extends to various slender structures, such as skyscrapers, antenna towers, but also bridges, and dams. Its contributions can enhance structural integrity evaluation and sustainability in manufacturing. The usage of the system can vary from a single deployment in wind parks to an entire park, allowing for a better understanding of the turbine's target state and the detection of outliers.

Measured data provides reliable displacement values as long as a fixed solution of the RTK data is provided which relies on a stable internet connection for correction data and on tropospheric conditions. A loss of the fixed solution status results in a drift of the position data. This may be overcome in future iterations by considering the full covariance matrix of the RTK measurement.

The limited RTK sampling rate and event-triggered SCADA data, as well as the unavailability or low quality of RTK data, require imbalance measures. Firstly, the acceleration data can be adapted or downsampled to match the RTK data sampling frequency. In cases of unavailability, a mapped tilt sensor measuring the tower's top tilt can serve as a fallback system for static displacement. Furthermore, the Kalman filter can be enhanced to accommodate only the currently available data.

Acknowledgements. The authors express their gratitude to the AdV for providing the SAPOS data, which significantly contributed to the success of this research. Additionally, the authors extend their heartfelt appreciation to Prof. Dr.-Ing. Cecilia Smoglie, Director of Energy and Environment from the Instituto Tecnológico de Buenos Aires (ITBA) for her invaluable collaboration. The authors also acknowledge the TUM International Graduate School of Science and Engineering (IGSSE) for their support. Finally, special thanks to Ramzes Mosiej for his valuable contributions.

References

1. Kim K et al (2018) Structural displacement estimation through multi-rate fusion of accelerometer and RTK-GPS displacement and velocity measurements. Measurement 130:223–235
2. Botz M, Oberlander S, Raith M, Grosse C (2016) Monitoring of wind turbine structures with concrete-steel hybrid-tower design
3. Botz M, Zhang Y, Raith M, Pinkert M (2017) Operational modal analysis of a wind turbine during installation of rotor and generator
4. Wondra B, Rupfle J, Emiroglu A, Grosse CU (2022) Analysis of icing on wind turbines by combined wireless and wired acceleration sensor monitoring. Lecture notes in civil engineering. Springer International Publishing, pp 143–155
5. Kalman RE (1960) A new approach to linear filtering and prediction problems. Trans ASME–J Basic Eng 82:35–45
6. Dong X et al (2021) Research on decomposition of offset in MEMS capacitive accelerometer. Micromachines 12:1000
7. Rupfle J, Emiroglu A, Grosse C (2022) Investigation of the measurability of selected damage to supporting structures of wind turbines. J Phys Conf Ser 2151(1):012008
8. Botz M, Harhaus G, Grosse C (2019) Monitoring modal parameters and external loads of wind turbines for remaining useful life analysis
9. Emiroglu A et al (2017) Fe-modelling and analysis of a hybrid wind-turbine tower for fatigue analysis and remaining life-time prediction. In: WESC2017
10. Osterminski K, Gehlen C (2018) Echtzeitmodellierung der Ermüdung von Windenergieanlagentürmen
11. Loew S, Obradovic D, Bottasso CL (2019) Direct online rainflow-counting and indirect fatigue penalization methods for model predictive control. In: 2019 18th European control conference (ECC), pp 3371–3376

Publication 3: Operational Sensor Adjustment for Structural Health Monitoring Systems in Wind Turbines

Rupfle, J., Wondra, B., & Nowack, M. (2024). Operational Sensor Adjustment for Structural Health Monitoring Systems in Wind Turbines. Frontiers in Nondestructive Testing and Evaluation: Academic Insights (2022/23). *Research and Review Journal of Nondestructive Testing (ReJNDT)*. Vol. 2. https://doi.org/10.58286/30175

This work presents three automated methods for sensor offset and orientation adjustment in SHM systems for wind turbines. Accurate sensor alignment is critical for reliable measurements of loads, vibrations, and deflections, enabling tasks such as RUL estimation, anomaly detection, and fault identification. The methods were validated on a 3 MW wind turbine with a 142 m hub height and hybrid tower. Data from tilt, acceleration, strain, and environmental sensors were analyzed using ML techniques.

The RSA analyses a 360-degree nacelle rotation during downtime, using rotor weight-induced tower bending to fit a sinusoidal model. This yields sensor offset, orientation, and relative sensitivity. The USA applies polynomial regression on operational data from both positive and negative axis directions, determining offsets where thrust force compensates rotor mass-induced bending. The BSA extends USA to two axes, fitting bivariate polynomial or conic models to power–tilt surfaces without requiring specific yaw angles. It includes feature selection, Gaussian filtering, and outlier removal to improve RMSE and MAE.

Results show RSA is efficient post-installation but sensitive to wind influence. USA offers refined offsets if sufficient directional data exist. BSA is robust against incomplete directional coverage and achieved the lowest errors. The methods can be applied to other slender structures and thus improve sensor calibration, fault detection, and long-term drift monitoring in SHM applications.

Author Contribution: Conceptualization, Methodology, Software, Data Curation, Investigation, Formal analysis, Writing - Original Draft, Writing - Review & Editing, Visualization.

Research and Review Journal of Nondestructive Testing (ReJNDT) - ISSN 2941-4989 - www.ndt.net

Operational Sensor Adjustment for Structural Health Monitoring Systems in Wind Turbines

Johannes Rupfle[12], Bernhard Wondra[1], Markus Nowack[3]

[1] Chair of Non-destructive Testing, TUM School of Engineering and Design,
Technical University of Munich, Franz-Langinger-Str. 10, Munich, 81245, Germany
E-mail: johannes.rupfle@tum.de
[2] Instituto Tecnológico de Buenos Aires, San Martín 202, Buenos Aires, 1004, Argentina
[3] ASC GmbH, Ledererstraße 10, Pfaffenhofen, 85276 Germany

Abstract

The digitalization in structural engineering significantly amplified the importance of Structural Health Monitoring systems, especially in civil engineering and the renewable energy sector. Initially, after installation, a monitoring system needs to be adjusted. This paper presents three methods to adjust sensor offsets of tilt and acceleration in wind turbine towers. In the first method, we use an initiated 360-degree nacelle rotation and its unbalanced rotor weight-induced tower bending. In the second method, uniaxial operational data forms a database for a univariate regression. A third method uses a biaxial operational data set for a multivariate regression. The second and third approaches can be extended to any slender structure under environmental load. The presented workflow also allows for automated sensor orientation determination and fault detection due to long-term drift observation of sensor characteristics.

Keywords: Structural Health Monitoring, Condition Monitoring, Sensor Adjustment, Sensor Orientation, Wind Turbine, Wind Energy, Slender Structures, Machine Learning, Supervised Learning

1 Introduction

Sensor-based Structural Health Monitoring (SHM) is increasingly recognized in infrastructure, high-rise buildings, and renewable energy, particularly for dams and wind turbines. A key challenge in SHM is optimally adjusting sensors, as their initial state significantly affects data accuracy. In wind turbines, this task is complicated by rotor weight-induced tower bending, which occurs independently of and in opposition to wind loads.

Figure 1 illustrates a wind turbine's side view and the forces acting during idle (a), partial (b), and high partial to nominal load (c). In (a), a gravitational force F_g acts in front of the vertical tower axis and introduces a positive bending moment on the tower. In (b), a simplified thrust force F_t on the rotor hub fully compensates for the gravitational force, resulting in zero tower bending moment. In (c), a higher thrust force creates a negative bending moment. Typically, the combined center of gravity of rotor and nacelle remains in front of the vertical tower axis, introducing a positive bending moment that counteracts the thrust force-induced negative bending moment.

The state of equilibrium when sensor offsets are adjusted is unknown and can not be intentionally reproduced. Accurate and precise sensor data are fundamental to the success of SHM applications such as structural response analysis, load estimation, Remaining Useful Life (RUL) estimation, anomaly detection, damage identification, and sensor failure detection.

Three data-driven methods are developed for wind turbine support structures, adaptable to other contexts. These methods are thoroughly tested and validated on a 3 MW test facility with a hub height of 142 meters, featuring a hybrid tower design of 82-meter pre-stressed concrete and 60-meter steel section. The measurement setup consists of accelerometers, tilt sensors (see Figure 2, details in Section 3.1), a seismometer, strain gauges, temperature sensors, and a Real Time Kinematic (RTK) sensor.

Exploring RUL and accumulated damage to supporting structures of wind turbines is crucial for sustainable and cost-effective operation. Botz et al. [1] and Geiss [2] developed methods to analyze damage scenarios and RUL by monitoring acceleration and strain data, supported by numerical simulations. Geiss [2] concluded that in-field NDT inspections can reduce model uncertainties. Integration of monitoring and inspection techniques into a digital twin concept, as discussed by Grosse [3], highlights the comprehensive approach to enhance lifecycle and sustainability of such structures.

 https://doi.org/10.58286/30175

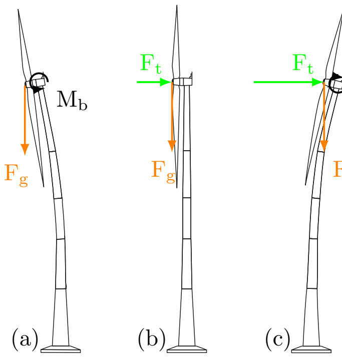

Figure 1: Forces acting on a turbine during idle (a), partial (b), and high partial to nominal load (c). [1]

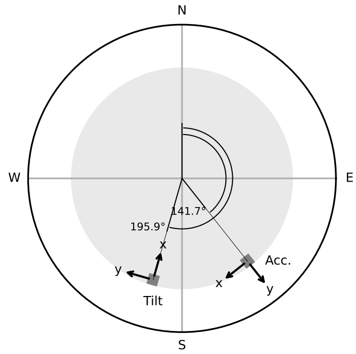

Figure 2: Sensor positions and orientations of tilt and acceleration sensors on 139 m tower height.

Challenges of long-term multiple sensor monitoring of a wind turbine and lessons learned are detailed by Rupfle et al. [4], emphasizing seven years of experience in data processing and integration into digital twin environments. Various studies address challenges in dynamic displacement calculation and frequency analysis in wind turbines. Botz et al. [1] and Botz et al. [5] focus on capturing dynamic displacements critical for turbine maintenance and RUL estimation. Similarly, Rupfle et al. [6] and Rupfle and Grosse [7] investigate challenges in measuring structural damages, emphasizing advanced measurement and data preprocessing techniques.

Studies by Rebelo et al. [8] and Loss et al. [9] stress the importance of accurately measuring and calibrating sensor data under operational conditions. Methods like tilt error compensation introduced by Jonscher et al. [10] and tower fatigue load modeling by Movsessian et al. [11] underscore the need for precise and reliable sensor data in SHM systems.

Studies also show that blade changes and damage can be detected using sensor systems in the tower. Khazaee et al. [12] and Kim et al. [13] demonstrate with numerical simulation that defective blades have a detectable effect on tower vibrations. Their analyses use the classifier CNN, which utilizes vibration time series amplitudes, discrete wavelet transformations, statistical feature functions, and operational modal analysis, respectively. Wondra et al. [14] explored the impact of blade icing on wind turbines by tower vibration measurements and showed influences on Eigenfrequencies and damping factors.

A study investigating high-rise buildings' static and dynamic response using strain sensors is presented by Oh et al. [15]. Wind tunnel tests were used to train an evolutionary radial basis function neural network to accurately predict strain responses based on wind speeds and directions. Shan et al. [16] reviews health monitoring systems and in-field testing of high-rise buildings. State-of-the-art applications on high-rise buildings involve accelerometers, strain gauges, anemometers, but also RTK sensors and thermometers. It is concluded that monitoring studies and projects in bridge and wind engineering are relatively more advanced so far. A study from Ghannadi and Kourehli [17] demonstrates that the slime mold algorithm combined with the modified total modal assurance criterion is highly effective for accurate damage detection in slender structures like the Canton Tower using vibration data, outperforming other optimization methods in terms of precision and reliability.

This work adheres to reporting standards outlined by Kapoor et al. [18] for research involving machine learning methods. It focuses on supervised learning techniques for sensor offset and orientation challenges, serving as the basis for accurate data analysis and structural analysis. In SHM applications, sensor data adjustment, and self-monitoring still pose a mostly unaddressed issue. Data-driven methods for sensor offset adjustment, orientation determination, sensitivity analysis and tracking, and long-term sensor data stability are developed to help enhance sensor data's usability and enable self-monitoring of sensors.

2 Methodology

Optimal sensor adjustment is crucial for efficient monitoring, allowing detailed load, vibration, and deflection analysis. The developed methodologies aim to provide solutions for wind turbines and other slender structures, focusing on data-intensive approaches.

[1]The illustration does not represent a mechanical state of equilibrium and only shows forces in Fore-Aft (FA) direction taken into consideration in this analysis. Illustrated tower bending is disproportionately.

Three methods are presented to provide automated optimal sensor adjustment techniques:

Rotational Sensor Adjustment (RSA): An approach based on the rotor weight-induced tower bending during an initiated 360-degree rotation at turbine downtime

Uniaxial Sensor Adjustment (USA): An uniaxial approach using operational data in positive and negative axis direction

Biaxial Sensor Adjustment (BSA): A biaxial method using operational data at partial load

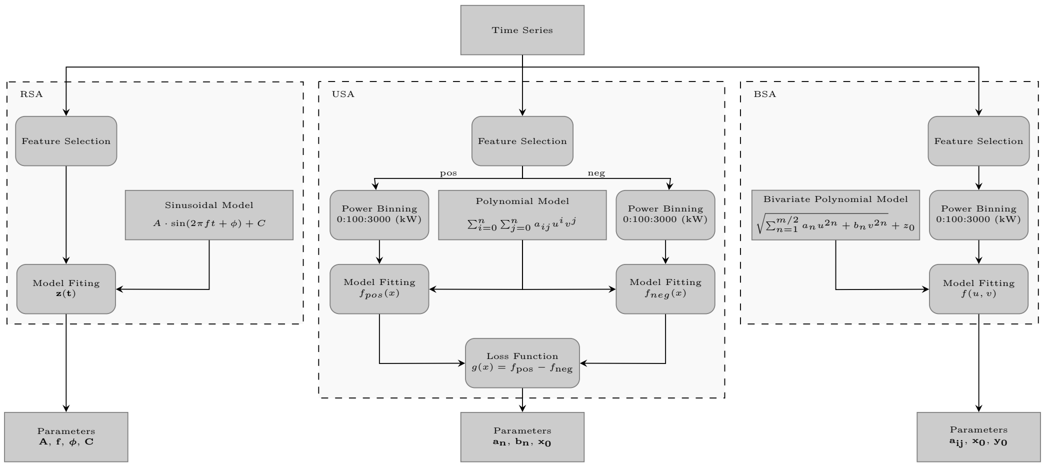

Figure 3: Flowchart of RSA, USA, and BSA for sensor adjustment.

A flowchart of the three developed methods is illustrated in Figure 3. A time series of measured data serves as input for the techniques. The subsequent feature selection process (see Section 3.3) is carried out for each individual method differently. For RSA, the fitting input is a time series of an initiated 360-degree rotation, while USA and BSA input are power-binned data. As USA treats data in positive and negative axis direction independently, an extra step incorporating a loss function is needed to extract the fitting parameters. The model selection for all methods is based on exploratory data analysis to summarize the main relationship between the features and the dependent variable.

2.1 Rotational Sensor Adjustment (RSA)

Yaw angle alignment to changing wind directions can twist the power cable loop between the nacelle and the turbine foundation. To untwist it, a 360-degree nacelle rotation is performed. The RSA method utilizes the rotor weight induced tower bending in FA direction for sensor adjustment purposes. This bending follows the FA direction during the nacelle rotation, inducing a sinusoidal amplitude in tower-fixed sensor data. This sinusoidal data is then fitted to a model (Equation 1), where $\mathbf{z(t)}$ is the sensor reading or dependent variable at time $\mathbf{t}$, $\mathbf{A}$ is the amplitude, $\mathbf{f}$ is the frequency, denoting the rotational speed of the nacelle rotation, $\boldsymbol{\phi}$ is the phase shift, representing the sensor axis orientation, and $\mathbf{C}$ is the vertical offset, indicating the constant sensor data offset.

$$z(t) = A \cdot \sin(2\pi ft + \phi) + C \tag{1}$$

The sinusoidal model captures the tower's periodic bending around its vertical axis during a 360-degree rotation. Here, $\mathbf{z(t)}$ represents sensor data over time. Although designed for time series analysis, the core relationship is between tilt and yaw angle rather than time.

2.2 Uniaxial Sensor Adjustment (USA)

USA uses load scenarios from different turbine operation states, combining rotor weight and thrust force-induced tower bending in positive and negative axis directions. Few data points are exactly on the positive and negative axes, so an angle tolerance of ± 8.11 deg ($\cos(\pm 8.11) \geq 0.99$) is allowed, with deviations in sensor values kept below 1 %.

The method assumes sensor amplitude correlates with power output. To fit a model to the imbalanced data set, the data is discretized and binned to exclude frequent operational states' influence. Mean values create a surface fitted to a model without distortion. 100 bins from 0 kW to 3000 kW are used for discretization.

All data points are aggregated into power output bins, as power output best correlates with the tower's load response. Using wind speed instead results in higher standard deviation due to variable rotor speed and pitch angle affecting thrust force. Functions in Equations 2 and 3 are regressed, where $\boldsymbol{f_{\mathrm{pos}}}$ is the positive sensor axis, $\boldsymbol{f_{\mathrm{neg}}}$ is the negative sensor axis, $\boldsymbol{a_n, a_{n-1}, \ldots, a_0}$ are the coefficients for the positive direction regression, and $\boldsymbol{b_n, b_{n-1}, \ldots, b_0}$ are the coefficients for the negative direction regression. The polynomial degree is chosen based on sensor characteristics and transfer function.

Polynomial fits can use a partial or full data set range. Partial ranges may fit better linearly, while full ranges risk overfitting. After fitting, a loss function $\boldsymbol{g(x)}$ is calculated in Equation 4, where $\boldsymbol{f_{\mathrm{pos}}}$ is the positive sensor axis, $\boldsymbol{f_{\mathrm{neg}}}$ is the negative sensor axis, $\boldsymbol{a_n, a_{n-1}, \ldots, a_0}$ are the coefficients for the positive direction regression, and $\boldsymbol{b_n, b_{n-1}, \ldots, b_0}$ are the coefficients for the negative direction regression. The two regression models are subtracted from each other, leading to a solution for the optimal sensor offset adjustment and precise zero tower bending power output value. Zero tower bending occurs when the thrust force compensates for the mass-induced bending moment.

$$f_{\mathrm{pos}}(x) = a_n x^n + a_{n-1} x^{n-1} + \ldots + a_1 x + a_0 \tag{2}$$

$$f_{\mathrm{neg}}(x) = b_n x^n + b_{n-1} x^{n-1} + \ldots + b_1 x + b_0 \tag{3}$$

$$g(x) = f_{\mathrm{pos}}(x) - f_{\mathrm{neg}}(x) = (a_n - b_n)x^n + (a_{n-1} - b_{n-1})x^{n-1} + \ldots + (a_1 - b_1)x + (a_0 - b_0) \tag{4}$$

2.3 Biaxial Sensor Adjustment (BSA)

To enhance the uniaxial method, the yaw angle in BSA is not limited to the axial directions but will handle the full 360-degree data set. As data below the zero tower bending threshold leads to distortion, a feature selection process excludes stand-still and low power output data from the analysis. To create a bivariate and parameterized model, a similar polynomial model of degree n is developed as depicted in Equation 5, when $\boldsymbol{f(u, v)}$ is the polynomial function of two variables, $\boldsymbol{u}$ and $\boldsymbol{v}$, $\boldsymbol{a_{ij}}$ are the coefficients of the polynomial, and $\boldsymbol{x_0}$ and $\boldsymbol{y_0}$ are the offsets for $\boldsymbol{x}$ and $\boldsymbol{y}$ respectively.

This flexible model fits various bivariate data, especially when the data's center or symmetry isn't at the origin. The method uses a second-degree bivariate polynomial with offsets, simplified to Equation 6, when $\boldsymbol{f(u, v)}$ is the polynomial function of two shifted variables, $\boldsymbol{u}$ and $\boldsymbol{v}$, and $\boldsymbol{a_{ij}}$ are the coefficients of the polynomial.

$$f(u, v) = \sum_{i=0}^{n} \sum_{j=0}^{n} a_{ij} \cdot u^i \cdot v^j; \qquad \text{with } u = x - x_0, \quad v = y - y_0 \tag{5}$$

$$f(u, v) = a_{00} + a_{10}u + a_{01}v + a_{20}u^2 + a_{11}uv + a_{02}v^2; \qquad \text{with } u = x - x_0, \quad v = y - y_0 \tag{6}$$

This simplifies the polynomial by centralizing it around the offsets x_0 and y_0, making analysis and curve fitting clearer. Fitting this model accurately defines sensor offset values and tracks sensor axis sensitivities. It also allows for predicting sensor data based on the model's fit within small operational ranges.

A refined model for lower power output values is developed, based on the conic and even polynomial in Equation 7, when $\boldsymbol{f(u, v)}$ is the polynomial function of two shifted variables, $\boldsymbol{u}$ and $\boldsymbol{v}$, $\boldsymbol{a_n}$ and $\boldsymbol{b_n}$ are the coefficients of the polynomial, $\boldsymbol{z_0}$ is the vertical constant offset, and $\boldsymbol{m}$ is the model degree. Choosing an appropriate model order ensures a good model fit without overfitting.

$$f(u, v) = \sqrt{\sum_{n=1}^{m/2} a_n u^{2n} + b_n v^{2n}} + z_0; \qquad \text{with } u = x - x_0, \quad v = y - y_0 \tag{7}$$

This model has particular benefits in capturing the dynamics of lower power output values. The choice of even exponents and a square root function allows for capturing the nonlinear characteristics of lower power output values, enhancing the model's accuracy and applicability. By selecting an appropriate maximum degree m, the model balances complexity and the risk of overfitting, ensuring a robust fit.

The development of these three different methods - RSA, USA, and BSA - provides a comprehensive approach to optimizing sensor accuracy in slender structures, particularly wind turbines. Each technique, with its methodology and focus, addresses specific aspects of sensor analysis.

3 Study Design

This section introduces the measurement setup and the used data sets for training and testing and gives an overview of the feature selection process.

3.1 Measurement setup

This study analyzes a tilt (ASC TS92V5-015) and an acceleration (ASC EQ-3211-003) sensor installed on a tower platform at the height of 139 m, right below the nacelle. Both sensors are mounted on the inner circumference as depicted in Figure 2, positioned at approximately 195.9 deg and 141.7 deg from true north. The coordinate systems are rotated 285.9 deg and 141.7 deg clockwise from true north. For simplicity, it is assumed that the sensors are located on the tower axis.

3.2 Data set

This paper analyzes a comprehensive dataset from a wind turbine, spanning 2 382 hours (99.25 days) from 2023-09-16 18:00:00 to 2023-12-24 23:59:59 in UTC time. The sensors sampled with 100 Hz are resampled to 0.1 Hz to focus on quasi-static states. The sampling rate of 100 Hz is adequate to analyze the structure's Eigenmodes up to the 3$^{\text{rd}}$ bending mode at 3.3 Hz as they are analyzed by Botz et al. [1]. To address data imbalance, such as for lower resolution Supervisory Control and Data Acquisition (SCADA) data, missing values are filled by propagating from the last valid observation to the next valid observation or, for yaw angle data, using a fixed gradient backward interpolation method [6]. The dataset's wind direction predominantly ranges from South-West and North-West, with negligible data share from North to East. However, data from all wind directions is present, as illustrated in Figure 4. For validation purposes, a test data set is introduced in Section 5 that covers 168 hours (7 days) of data from 2023-12-25 00:00:00 to 2023-12-31 23:59:59 in UTC time.

3.3 Feature Selection

Data evaluation requires a feature selection process. In this context, three distinct methodologies are deployed. For RSA, the data set is refined based on specific criteria: The rotor speed at 0 RPM, indicating a non-operational state of the turbine; pitch angle fixed at 90 deg, removing wind influence; wind speed below 6 m/s to ensure minimal external force impact; and consistent 360-degree rotation of the nacelle observed, providing a complete rotational profile. This approach identifies the system's intrinsic behavior in a controlled setting.

To understand the turbine's operational behavior, characteristic curves are derived from the 10-second mean data, shown in Figure 5. The variable rotor speed reaches its nominal speed at 2300 kW power output and a wind speed of almost 10 m/s. At a wind speed of 11.1 m/s or a power output of 2700 kW, the pitch angle rises to limit the power output to the nominal power rate of 3000 kW. At a wind speed of 12.3 m/s, the pitch angle adapts to the full load operational behavior. Data of wind speeds above the cut-off wind speed of 25 m/s represent wind gusts and show high fluctuation.

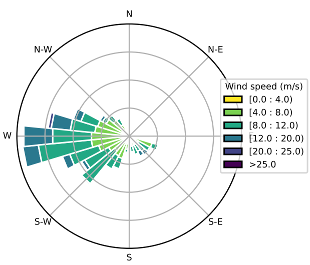

Figure 4: Wind distribution in direction and speed of used training data set.

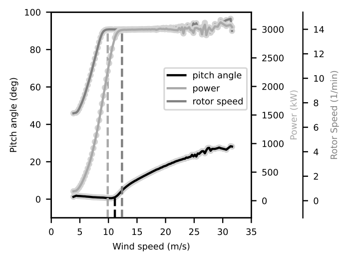

Figure 5: Turbine characteristics from cut-in to cut-off wind speed providing knowledge for feature selection.

A more comprehensive feature selection algorithm was developed for USA. Higher frequency vibrations are filtered by averaging the data over 10-second intervals to focus on quasi-static sensor amplitudes. Feature selection deploys specific operational boundaries: power output range from 500 kW to 2500 kW, pitch angle limit of 0.1 deg to maintain a consistent correlation between power and sensor output; and wind speed range between 4 m/s and 12 m/s to avoid full load and transient operational scenarios. Afterward, the subset is divided into directional data concerning the sensor axis orientation.

Similarly, BSA uses 10-second data without restricting the yaw angle in its 10-second averaged data. Feature selection criteria: power output range from 500 kW to 2500 kW; pitch angle limit of 0.1 deg; and wind speed range between 4.0 m/s and 12 m/s, focusing on operational data.

4 Results

This section evaluates the three methods using the data set presented in Section 3.2. Three events of a 360-degree rotation during shutoff and low wind speeds occurred in the data set, and data of the full 2 382 hours data set is used USA and BSA. Sections 4.2 and 4.3 focus on the tilt sensor. Analysis of the acceleration data works similarly and can be made available upon request.

4.1 Rotational Sensor Adjustment (RSA)

The feature selection process identified three suitable events with low wind speeds during a 360-degree rotation at downtime. They feature a duration of 665.84 s (2023-09-24), 663.75 s (2023-10-08), and 664.84 s (2023-10-16), resulting in an average rotational speed of 0.542 deg/s. Figure 6 depicts the wind speed and yaw direction of the 2023-10-16 event. The mean wind speed is 2.01 m/s, with wind direction changing from 0 deg (North) to 45 deg (North-East). The wind direction during the event is absent in the SCADA data.

The sensor data's 100 Hz time series is provided as input to the model. The tilt sensor data and the model fit is shown in Figure 7 (a, b), the acceleration data and the model fit in Figure 7 (c, d). Dynamic oscillations of higher frequency superimpose the data. However, the mean values correspond to the fitted result. The result represents a sinusoidal course of an amplitude that directly relates to the sensor sensitivity, a frequency corresponding to the rotational speed of the nacelle, a phase representing the sensor axis orientation, and the sensor offset.

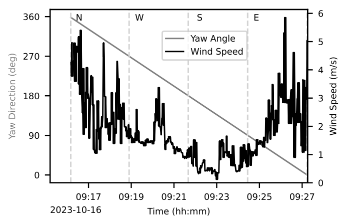

Figure 6: Wind speed and yaw direction during 360-degree rotation at downtime of the turbine on 2023-10-16. The mean wind speed during the event is 2.01 m/s. The rotational direction is counterclockwise. Wind direction before and after the event is approximately 0 deg (North) and 45 deg (North-East).

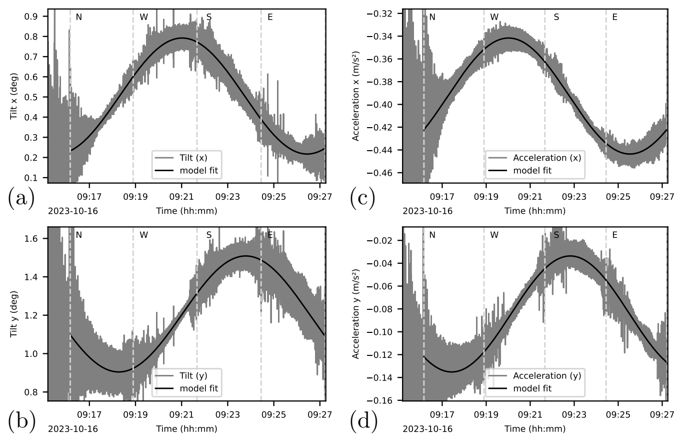

Figure 7: Tilt (a, b) and acceleration (c, d) data during 360-degree rotation of turbine with fitted sinusoidal function.

Table 1 shows the model parameters for the tilt and acceleration sensors. The amplitude parameter offers insights into relative sensor sensitivities but no absolute sensor sensitivity. The tilt sensor's x-axis show a minor deviation of −4.6 %, while the acceleration sensor axes are well-aligned. The frequency parameters match the nacelle's rotation speed (0.542 deg/s). The phase parameters, consistent with the sensor axis orientations (refer to Figure 2), show phase differences between axis pairs at 87.9 deg and 96.6 deg for tilt and acceleration sensors, respectively, against an ideal orthogonal phase difference of $\pi/2$ radians. The model's offsets indicate environmental influences on the sensor axes. In the discussion section (Section 5), a deeper analysis of these offset values is provided. The mean Root Mean Square Error (RMSE) for the tilt sensors -axis is 0.047 deg, while the y-axis shows a higher mean RMSE of 0.098 deg. The acceleration sensor axes do not exhibit any significant divergence.

	2023-10-16				**2023-10-08**				**2023-09-24**			
	Tilt (x)	**Tilt (y)**	**Acc. (x)**	**Acc. (y)**	**Tilt (x)**	**Tilt (y)**	**Acc. (x)**	**Acc. (y)**	**Tilt (x)**	**Tilt (y)**	**Acc. (x)**	**Acc. (y)**
A	0.288	0.302	0.051	0.051	0.288	0.302	0.050	0.051	0.287	0.301	0.051	0.051
f	0.0015	0.0015	0.0015	0.0015	0.0015	0.0015	0.0015	0.0015	0.0015	0.0015	0.0015	0.0015
ϕ	5.045	3.511	5.664	3.977	4.644	3.511	5.269	3.649	4.450	2.927	5.123	3.468
C	0.505	1.207	-0.393	-0.084	0.681	1.461	-0.389	-0.027	0.635	1.246	-0.380	-0.070
RMSE	0.041	0.081	0.009	0.002	0.042	0.093	0.010	0.009	0.058	0.121	0.016	0.013
MAE	0.029	0.054	0.006	0.006	0.032	0.066	0.007	0.007	0.044	0.080	0.010	0.009

Table 1: Parameterization of 360-degree rotation model for tilt and acceleration sensor axes.
A: Amplitude in sensor data unit (deg for tilt and m/s^2 for acceleration sensor); f: Frequency in Hz; ϕ: Phase shift of the model fit in rad from start angle of rotation from true north (2023-10-16: 359.85 deg; 2023-10-08: 22.87 deg; 2023-09-24: 33.55 deg); C: Constant offset in sensor data unit (deg or m/s^2); RMSE: in sensor data unit (deg or m/s^2); Mean Absolute Error (MAE): in sensor data unit (deg or m/s^2).

4.2 Uniaxial Sensor Adjustment (USA)

For USA, a refined subset of the full data set is used. The data is resampled to 10-second-mean values, with the feature selection process reducing the data set to 22.82 %. To analyze symmetric tower bending as a function of the power output in the sensor axis direction, dividing the subset to data in positive and negative axis direction limits the data set to 0.877 % and 0.001 % for the x-axis and 0.310 % and 2.635 % for the y-axis, respectively. This shows a high imbalance and insufficient data for the negative x-axis. The results for both axes are shown in Figure 8 and Table 2.

For the negative x-axis direction, a function regression is not possible, making the workflow unsuitable for this data set. However, for the y-axis data, the regression functions for both directions yield good results with $RMSE = 118.0\ kW$ and $MAE = 107.1\ kW$.

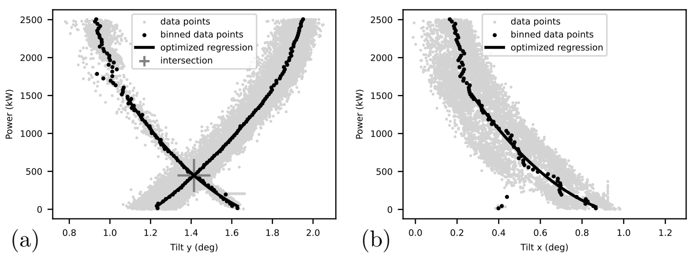

Figure 8: Uniaxial adjustment of tilt sensors y-axis (a) and x-axis (b) (Altitude: 139 m) with bidirectional regression intersection.

Model		Univariate
$\mathbf{x_0}$	deg	-
$\mathbf{y_0}$	deg	1.4139
RMSE	kW	118.0
MAE	kW	107.1

Table 2: Fit results of univariate quadratic polynomial model.

4.3 Biaxial Sensor Adjustment (BSA)

We developed a biaxial approach to address missing data in the uniaxial method, using 11.48 % of the data set after feature selection, increasing the accuracy in determining the sensor offset in the x-axis direction. Figures 9 (a) and 10 (a) represent the subset of 10-second mean data for the tilt and acceleration sensor. Due to the highly imbalanced subset, a direct regression is not feasable.

A 2D grid is created to analyze wind turbine power distribution relative to sensor data. Sensor data points are binned based on their x and y coordinates, forming a matrix where each cell represents the average power output for that segment. The data distribution is unbalanced and incomplete, and the sensors are not aligned in the same direction. The analysis will focus on the tilt data only, as the workflow is identical for different sensor types.

The subset is interpolated into a grid, creating a smooth representation of power output across the x-y sensor data (Figure 11 (a)). Due to the incomplete surface of the data, a direct application of a gradient descent algorithm may not be effective.

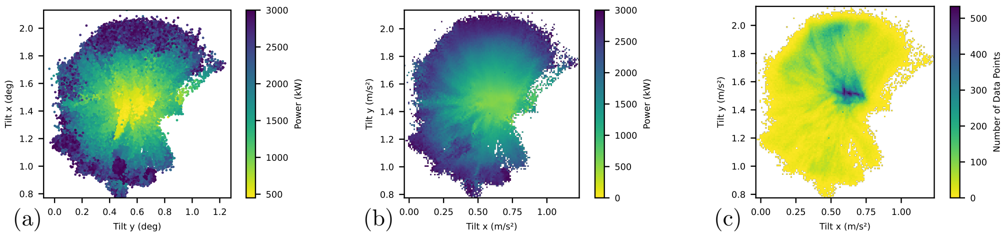

Figure 9: Tilt sensor data distribution in bins of bin size 0.01 deg: (a) 10-second-mean value; (b) mean power output of each bin; (c) number of data points per bin.

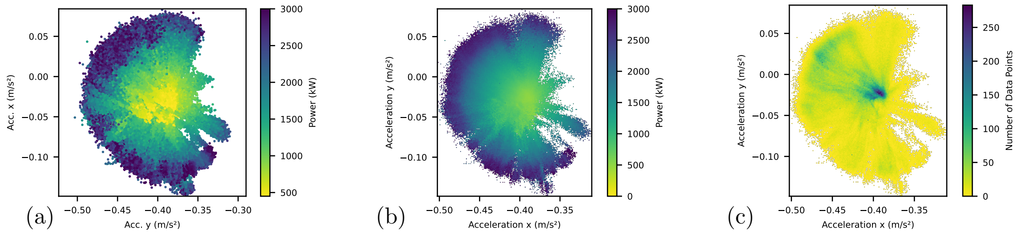

Figure 10: Acceleration sensor data distribution in bins of bin size $0.001\,\mathrm{m/s^2}$: (a) 10-second-mean value; (b) mean power output of each bin; (c) number of data points per bin.

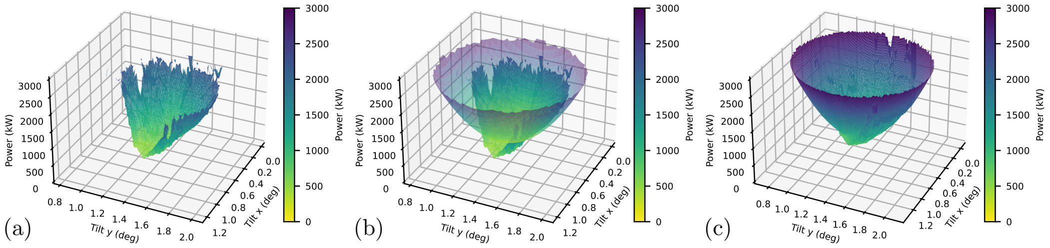

Figure 11: Biaxial model fit: (a) Surface of tilt sensor data.; (b) Surface of tilt sensor data and quadratic regression model of 2$^{\text{nd}}$ degree overlayed.; (c) Merged surface to smooth results and to extend gathered data to all possible operational states.

A bivariate quadratic polynomial (Equation 6) is used to fit the data, determining offsets in both the x and y direction. The input data is shown in Figure 11 (a). The data is reduced to a subset containing a power output range of 750 kW to 2500 kW, as empiric analysis showed the best results for these boundaries. Data below or above the range may contain external influences from transient operations, negatively influencing results or may contain edge cases, distorting the result.

The parameterized function is depicted in Figure 11 (b). For simplification, the parameters a_{10}, a_{01}, and a_{11} from Equation 6 are set to 0, and parameter a_{00} is limited around the previously determined value of 443 kW. Assuming equal sensor sensitivity, a_{20} and a_{02} are set equally for symmetry. Subsequently, the regression model and the derived characteristic can be averaged to smooth and extend the result to all operational states and all directional angles, thus making it an independent characteristic curve (Figure 11 (c)). The mean squared error of the model is $RMSE = 253.6\,\mathrm{kW}$ with $MAE = 195.3\,\mathrm{kW}$.

To reduce RMSE and MAE, the method is refined by using a Gaussian filter to derive the measurement grid that applies a bell-shaped curve that averages nearby values more heavily than distant ones. This creates the surface, blurring sharp edges and smoothing transitions. The result of the refined surface is depicted in Figure 12 (a).

Modifying the regression model to a conic polynomial (Equation 7) leads to a further refined model fit with $RMSE = 229.2\,\mathrm{kW}$ and $MAE = 176.0\,\mathrm{kW}$, improving the result. The fitted model is shown in Figure 12 (b). (c) represents the optimized merged fit. The model represents the biaxial tilt data and the predicted power output of the turbine for the operational state above the true zero tower tilt (power output of 443 kW).

A third pipeline represents an iterative enhancement of sensor offset determination and model accuracy

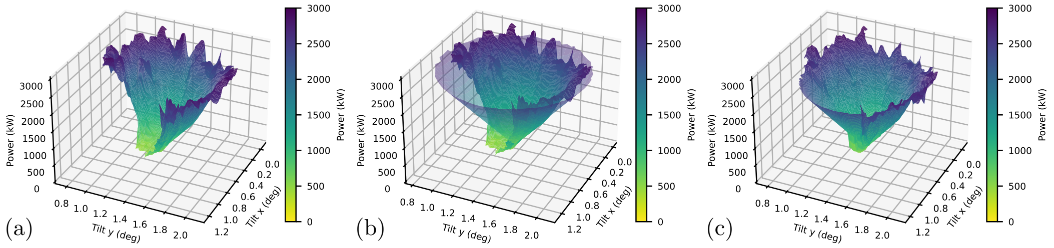

Figure 12: Biaxial model fit: (a) Surface of tilt sensor data with applied Gaussian filter; (b) Surface of tilt sensor data with applied Gaussian filter and conic regression model of 2$^{\text{nd}}$ degree overlayed; (c) Optimized merged surface to smooth results and to extend gathered data to all possible operational states.

to refine the results. Initially, the process generates a loss function, which combines raw surface data with the previous model parameters identified in Figure 12 (b). To refine the data quality, outliers exceeding the 90th percentile are removed, followed by a Gaussian filter, resulting in a smoother surface, particularly noticeable in the central region of the data where the most artifacts occur, as shown in Figure 13 (a).

Optimization of the model parameters, illustrated in Figure 13 (b), reduces the MAE to 104.2 kW, leading to offset parameters of $x_0 = 0.6210$ deg and $y_0 = 1.4434$ deg. The final optimized merged result is shown in 13 (c).

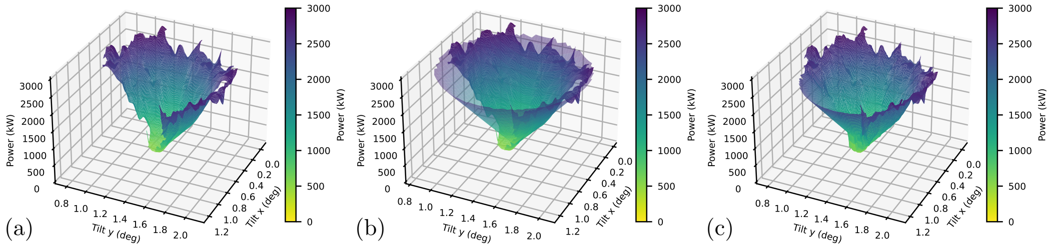

Figure 13: Biaxial model fit: (a) Surface of tilt sensor data with applied Gaussian filter and outlier removal; (b) Surface of tilt sensor data with applied Gaussian filter and outlier removal and conic regression model of 2$^{\text{nd}}$ degree overlayed; (c) Optimized merged surface to smooth results and to extend gathered data to all possible operational states.

Table 3 shows the parameters x_0 and y_0 and the statistical measures for all models. Incorporating a Gaussian filter and a modified model significantly enhances the results. Specifically, the conic model shows a decrease of approximately 9.6 % in RMSE and 10.0 % in MAE. Furthermore, the outlier removal-optimized conic model achieves RMSE and MAE reductions of 49.4 % and 46.7 %, respectively, compared to the quadratic model. However, the changes in the sensor offsets x_0 and y_0 are relatively minor, with no significant improvements observed in the optimized conic model.

Model		**Quadratic**	**Conic**	**Conic (optimized)**
$\mathbf{x_0}$	deg	0.6434	0.6213	0.6210
$\mathbf{y_0}$	deg	1.4235	1.4494	1.4434
RMSE	kW	253.6	229.2	128.3
MAE	kW	195.3	176.0	104.2

Table 3: BSA fit results of bivariate quadratic polynomial and conic polynomial models.

5 Discussion

This section evaluates the three developed methods for sensor data analysis. Each method has distinct applications that can be combined for comprehensive analysis.

Rotational Sensor Adjustment (RSA): This method is ideal for initial sensor adjustment immediately post-installation, specifically for determining offsets and orientations. However, it is sensitive to wind-induced variation bending the tower, although the pitch angle is set to 90 deg to minimize influences. The method can also be used to identify sensitivity differences and to quantify noise spectral density.

Uniaxial Sensor Adjustment (USA): This method utilizes operational data from both positive and negative directions of an axis, significantly improving accuracy. The sensor axis orientation must be known to perform the analysis. An adequate quantity of data in both directions is required, as seen in Figure 8 (b), where no solution was given due to missing data. The uniaxial method can also detect offset for sensors placed in FA direction, e.g., directly installed into the nacelle as the system developed in Rupfle and Grosse [7].

Biaxial Sensor Adjustment (BSA): This method uses data from two perpendicular sensor axes to determine x and y-axes sensor offsets without specific yaw angle data. A feature selection process is developed to ensure an accurate model fit, selecting features only for power output values of operational states above the threshold, where the thrust force compensates for the mass-induced bending. The corresponding value can be either an assumption or determined using RSA.

RSA can determine sensor offset, orientation, and relative sensitivity in a very efficient and fast manner. We analyzed three instances of a 360-degree rotation during system downtime in the data set, each covering approximately 11 minutes of 100 Hz data. The mean offsets determined for the tilt sensor's x and y-axes are 0.607 deg and 1.304 deg, respectively. While a sample size of three is limited for comprehensive accuracy, it offers a preliminary assessment. The method's limitations include external wind influences that cannot be entirely excluded and the fact that a 360-degree rotation event is triggered by unpredictable changes in wind conditions, rather than occurring periodically.

USA offers a more precise offset determination and can also determine parameters of an operational state when the thrust force fully compensates for rotor weight-induced tower bending. For the y-axis, this method calculates an offset of 1.414 deg, using a substantial data set of 26 656 data points across both axis directions, totaling 70.16 hours of operational data. However, it cannot be applied to the x-axis due to missing data. This method no longer relies on triggered events but continuous data collection, yet its effectiveness depends on available data across both sensor axis directions.

To address previous limitations and accurately determine offsets for the x and y-axes, BSA was developed. The results show offsets of 0.621 deg and 1.443 deg for the x and y axes, respectively, using 98 423 data points, equivalent to 273.40 hours of operation. The method employs a two-stage outlier filtering based on the initial model, improving statistical measures. Although increasing the model's degree did not enhance the results, a second-order model was chosen to avoid overfitting. Unlike USA, BSA is not restricted to data from specific directions as it considers both sensor axes and utilizes an appropriate model. However, data availability and variability in yaw angle and power output significantly impact the results.

To validate the findings, sensor offsets and orientations are applied to a 168-hour test data set. Tilt and acceleration data are transformed into a nacelle-fixed coordinate system as defined by Rooij [19] based on yaw angle. The data set is refined by selecting only data points with a pitch angle below 0.1 deg to exclude power reduction, resulting in 119 642 data points over 332.34 hours.

Fore-Aft (FA) direction: Data validation in Figure 14 (a) confirms accurate determination of offsets and orientations, aligning with results from USA.

Side-Side (SS) direction: Tilt data in Figure 14 (b) initially aligns closely with zero bending but trends towards negative values, likely due to vertical wind gradients and gyroscopic precession opposing rotor rotation. Further details on gyroscopic effects in wind turbines are detailed by Chen et al. [20].

To further justify the methods and validate their accuracy, the relation of acceleration and tilt in FA direction is analyzed. Figure 14 (c) depicts the validation data set, indicating a linear relationship between the dependent and independent variables. In fact, the sinusoidal relationship can be linearized for small angles up to $\theta_L = 15\ deg$, which is the maximum detectable angle of the tilt sensor in its present configuration. A substitution of $sin\theta_L$ by its Taylor series expansion leads to Equation 8.

$$sin\theta_L = \sum_{n=0}^{\infty}(-1)^n \frac{\theta_L^{2n+1}}{2n+1!} = \theta_L - \frac{\theta_L^3}{3!} + \frac{\theta_L^5}{5!} - ... \tag{8}$$

If $sin\theta_L$ is substituted by θ_L, the maximum error can be estimated by $|\theta_L^3/3!|$, which is a relative error of 1.2 % for 15 deg. The relative error for an angle of 1 deg is approximately 0.005 %. Linearization around $\theta_L = 1$ deg (Equation 9) leads to a slope of $b = 0.17121\ \mathrm{m/s^2 deg}$.

$$b = \frac{1}{\theta_L} * g * \sin\theta_L \approx g\frac{\pi}{180\,\mathrm{deg}} \tag{9}$$

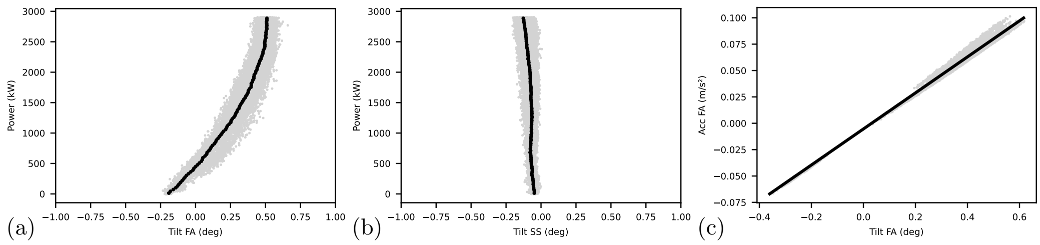

(a) (b) (c)

Figure 14: Tilt sensor data in FA (a) and SS (b) coordinates after offset removal with $x_0 = 0.621\,\mathrm{deg}$ and $y_0 = 1.443\,\mathrm{deg}$ and offset corrected and coordinate transformed test data set (c) for validation purposes with linear regression of $b = 0.17129\,\mathrm{m/s^2 deg}$ and intercept of $a = 0.0014\,\mathrm{m/s^2}$. $RMSE = 0.00257\,\mathrm{m/s^2}$ and $MAE = 0.00205\,\mathrm{m/s^2}$.

A linear regression leads to a slope of $b = 0.17129\,\mathrm{m/s^2 deg}$ and an intercept of $a = 0.0014\,\mathrm{m/s^2}$, showing an RMSE of $0.00257\,\mathrm{m/s^2}$ and an MAE of $0.00205\,\mathrm{m/s^2}$ and accurately represents the linearized relationship. It can be used for sensor fault detection and long-term drift analysis. Analyzing a potential tower misalignment might also be possible using BSA and would lead to a distorted surface, leading to a directional-dependent cost function.

6 Conclusion

This paper presents three approaches for determining sensor offsets, orientation, and faults using a subset of measurement data.

Rotational Sensor Adjustment (RSA)

- Can be applied for initial sensor adjustment post-installation, determining offsets and orientations.
- Sensitive to wind-induced variations that can affect the accuracy of the results.
- Provides insights into sensor sensitivity differences and allows for the quantification of noise spectral density.

Uniaxial Sensor Adjustment (USA)

- Utilizes long-term operational data from both positive and negative directions of an axis, significantly improving accuracy.
- Requires knowledge of sensor axis orientation and sufficient data across both directional axes.
- Can also be applied to nacelle-fixed sensors in wind turbines or uniaxial sensors in slender structures, allowing for precise offset determination and identification of states where thrust force fully compensates for rotor weight-induced tower bending.

Biaxial Sensor Adjustment (BSA)

- Combines data from two perpendicular sensor axes to determine sensor offsets without requiring specific yaw angle data.
- Utilizes a comprehensive feature selection process and a two-stage outlier filtering mechanism to ensure accurate model fits.
- Particular advantages for biaxial sensors, considering multi-directional loads and enabling fault detection and drift analysis over time.

Applied corrections show significant accuracy in the relation of tilt and acceleration with real-world scenarios. This allows for fault detection and drift analysis over time. It also allows for more precise RUL estimation, considering static loads. Determination of sensor orientation is performed directly using RSA. Future modifications in BSA could enable orientation determination by integrating yaw angle analysis. Future research shall explore structural misalignments and directional stiffness variations using the BSA model's cost function, thus broadening applicability for many SHM contexts.

Statement

The presented work is based on the PhD thesis of Johannes Rupfle entitled Wind Turbine Tower Top Motion Assessment for the Development of a Digital Shadow, submitted at Technical University of Munich in March 2024 as a first draft. The authors have no competing interests to declare relevant to this article's content. Data may be made available upon request.

Acknowledgements

The authors express their gratitude to the *German Federal Ministry for Economic Affairs and Climate Action* for funding the projects *MISTRALWIND* under grant number 0325795 and *IM Wind* under grant number ZF4561204DB9. Thanks to *Max Bögl Wind AG* and *Siemens Gamesa Renewable Energy* for providing access to the test facility. The authors also acknowledge the support of the *TUM International Graduate School of Science and Engineering (IGSSE)* and Professor Christian Grosse for overall supervision of the projects. Finally, special thanks to *Balázs Horváth* and *Ramzes Mosiej* for their valuable contributions to data treatment.

References

[1] M. Botz *et al.*, "Monitoring of wind turbine structures with concrete-steel hybrid-tower design," in *8th European Workshop On Structural Health Monitoring (EWSHM 2016)*, 2016.

[2] C. Geiss, "The mistralwind project – towards a remaining useful lifetime analysis and holistic asset management approach for more sustainability of wind turbine structures," 2017.

[3] C. Grosse, "Monitoring and inspection techniques supporting a digital twin concept in civil engineering," 2019.

[4] J. Rupfle, B. Wondra, and C. Grosse, "Long-term multiple sensor monitoring of a hybrid tower wind turbine – lessons learned," in *Experimental Vibration Analysis for Civil Engineering Structures*. Springer Nature Switzerland, 2023, pp. 539–549.

[5] M. Botz *et al.*, "Überwachung und Modellierung der Tragstruktur von Windenergieanlagen," *Beton- und Stahlbetonbau*, pp. 342–354, 2020.

[6] J. Rupfle, A. Emiroglu, and C. U. Grosse, "Investigation of the measurability of selected damage to supporting structures of wind turbines," *Journal of Physics: Conference Series*, vol. 2151, no. 1, p. 012008, 2022.

[7] J. Rupfle and C. Grosse, "Development of a minimalistic smart sensor system for motion measurement of wind turbine towers," *Lecture Notes in Mechanical Engineering (LNME)*, 2024.

[8] C. Rebelo *et al.*, "Structural monitoring of a wind turbine steel tower - part i: System description and calibration," *Wind and Structures An International Journal*, vol. 15, pp. 285–299, 2012.

[9] T. Loss, O. Gerler, and A. Bergmann, "Online calibration of accelerometers for monitoring of wind turbine blade movement," in *2020 IEEE International Instrumentation and Measurement Technology Conference (I2MTC)*. IEEE, 2020.

[10] C. Jonscher *et al.*, "Dynamic displacement measurement of a wind turbine tower using accelerometers: tilt error compensation and validation," *Wind Energy Science*, 2023.

[11] A. Movsessian, M. Schedat, and T. Faber, "Feature selection techniques for modelling tower fatigue loads of a wind turbine with neural networks," *Wind Energy Science*, vol. 6, no. 2, pp. 539–554, 2021.

[12] M. Khazaee, P. Derian, and A. Mouraud, "A comprehensive study on structural health monitoring (shm) of wind turbine blades by instrumenting tower using machine learning methods," *Renewable Energy*, vol. 199, p. 1568–1579, 2022.

[13] H.-C. Kim, M.-H. Kim, and D.-E. Choe, "Structural health monitoring of towers and blades for floating offshore wind turbines using operational modal analysis and modal properties with numerical-sensor signals," *Ocean Engineering*, vol. 188, p. 106226, 2019.

[14] B. Wondra *et al.*, "Analysis of icing on wind turbines by combined wireless and wired acceleration sensor monitoring," in *European Workshop on Structural Health Monitoring*. Springer International Publishing, 2023, pp. 143–155.

[15] B. K. Oh *et al.*, "Evolutionary learning based sustainable strain sensing model for structural health monitoring of high-rise buildings," *Applied Soft Computing*, vol. 58, p. 576–585, 2017.

[16] J. Shan *et al.*, "Health monitoring and field-testing of high-rise buildings: A review," *Structural Concrete*, vol. 21, no. 4, p. 1272–1285, 2020.

[17] P. Ghannadi and S. S. Kourehli, "Efficiency of the slime mold algorithm for damage detection of large-scale structures," *Struct. Des. Tall Spec. Build.*, vol. 31, no. 14, Oct. 2022.

[18] S. Kapoor *et al.*, "Reforms: Consensus-based recommendations for machine-learning-based science," *Science Advances*, vol. 10, no. 18, 2024.

[19] R. Rooij, "Terminology, reference systems and conventions," *TU Delft OpenCourseWare*, 2001.

[20] J.-h. Chen *et al.*, "Study on gyroscopic effect of floating offshore wind turbines," *China Ocean Engineering*, vol. 35, no. 2, p. 201–214, 2021.

List of Supervised Student Projects

Implementation of a Real-Time Data Analysis Environment in MATLAB/ Simulink

This thesis investigates different monitoring approaches for the supervision of the support structure of wind turbines, as part of the IMWind project at the Technical University of Munich. The tower of a test turbine is equipped with several sensors to measure acceleration, velocity, temperature, inclination, strain, and nacelle position. The main focus is the creation of a workflow for Real-Time Data transmission and the evaluation of the measurements in MATLAB/ Simulink. A measuring system from Gantner Instruments is installed in the plant. The main component is a Q.Station101T as well as the associated control software GI.Bench with the extension test.con. Necessary configurations are described. Data transfer between the measuring system and the evaluation program takes place using the MQTT network protocol. Two open source brokers from mosquitto are implemented for Real-Time Data transfer. In a comparison with other monitoring approaches, the data transfer via MQTT is convincing due to its lean structure and secure data transmission. A MATLAB app was programmed to analyze the measurement data. To better place the work in the context of wind turbine monitoring, various monitoring systems and their areas of application are discussed.

Author: Stephan Zimmermann

Merging of measurement data from various Structural Health Monitoring systems for further analysis

This thesis deals with the processing and archiving of measurement data generated during the monitoring of a wind turbine as part of the *IM Wind* project at the Technical University of Munich. The measurement systems found in the test facilities include a fixed and modular Data Acquisition measurement system, several wireless measurement systems, individual sensors with data loggers and a Supervisory Control and Data Acquisition system. The work assumes that the raw measurement files are available from the outset. The focus is on the separate and individual processing of the different data files as well as the merging, storage and subsequent access to these measurement data files. Particular attention is paid to synchronising the data over time and the various measurement frequencies. The data is merged using two MATLAB features, the tall array and the datastore, providing a practical example of the use of these MATLAB features. In addition to the evaluation of the archiving process, the compression of MATLAB files and the usable file versions are also evaluated in terms of the requirements for storage space, loading and saving time and the most favourable version for the archiving process is identified.

Author: Balázs Horváth

Automation of a script for downloading SCADA data via a programming interface

The utilization of wind energy as a sustainable and renewable source has witnessed significant growth in recent years, highlighting the importance of effectively monitoring and analyzing wind turbine performance The SCADA system plays a key role in providing real-time monitoring and control of complex industrial processes, including those in the wind energy sector. SCADA data is crucial for assessing the operational health and performance of these complex machines. The SCADA central server exposes an API that allows authorized users to retrieve relevant information. The API provides standardized endpoints and authentication mechanisms, ensuring secure access to the required data. However, there is a need to develop a script in a scripting programming language that can act as an interface between the team and the wind turbine's API, facilitating seamless retrieval of the necessary data. This thesis focuses on the development of two Python scripts tailored for a team engaged in studying damage measurability and long-term monitoring of wind turbine supporting structures. The scripts aim to retrieve both archive and real-time SCADA data from wind turbines. Archive data represents historical information collected over a given period, providing valuable insights into past turbine parameters such as pitch angle, frequency or current wind direction. Real-time data will be obtained by implementing polling, continuously querying the wind turbine's data source to ensure a consistent flow of up-to-date data, enabling real-time analysis and performance monitoring.

Author: Ramzes Mosiej

Design and Implementation of a Central Data Collection and Visualization System for a Multi Sensor Wind Turbine Monitoring System

The sensors of a SHM system produce a vast amount of data in various formats. To be useful, this data must be unified, stored long-term, and available for further processing. This thesis covers the different possibilities for transferring the data from the sensors, the storage types, and visualization software for real-time monitoring of the data on a theoretical level. Further, a Python script for data acquisition and transfer, with a special emphasis on data security and reliability was developed. The data storage backend is realized with the NoSQL database Apache Cassandra for which a data scheme was developed and deployed. For real-time monitoring and visualization of stored data, a Grafana instance with specially developed database queries is implemented.

Author: Jonas Theisen

List of Abbreviations

Adam	Adaptive moment estimation
ADC	Analog Digital Converter
AE	Acoustic Emission
AI	Artificial Intelligence
ANN	Artificial Neural Network
AOD	Age of Differential
API	Application Programming Interface
AR	Ambiguity Resolution
BSA	Biaxial Sensor Adjustment
CE	Cross-Entropy
CM	Condition Monitoring
CV	Computer Vision
DAQ	data Acquisition
DFT	Discrete Fourier Transformation
DIC	Digital Image Correlation
DL	Deep Learning
DM	Digital Model
DOF	Degree of Freedom
DS	Digital Shadow
DT	Digital Twin
EMA	Experimental Modal Analysis
FA	Fore-Aft
FE	Finite Element
FEM	Finite Element Model
FFT	Fast Fourier Transformation
GNSS	Global Navigation Satellite System
IoT	Internet of Things
IRT	infrared thermography
KF	Kalman Filter
LDV	laser Doppler vibrometer
LSTM	Long Short-Term Memory
MAE	Mean Absolute Error

MCP	McCulloch-Pitts
MEMS	Micro-Electro-Mechanical System
ML	Machine Learning
MQTT	Message Queuing Telemetry Transport
MSE	Mean Squared Error
N	Nacelle Fixed Coordinates
NDT	Non-destructive Testing
NLP	Natural Language Processing
NoSQL	Not only Structured Query Language
NREL	National Renewable Energy Laboratory
OLS	Ordinary Least Squares
OMA	Operational Modal Analysis
POD	Probability of Detection
PSD	Power Spectral Density
RMSE	Root Mean Square Error
RNN	Recurrent Neural Network
RSA	Rotational Sensor Adjustment
RT	Radiographic Testing
RTK	Real Time Kinematic
RUL	Remaining Useful Life
S	Sensor Fixed Coordinates
SCADA	Supervisory Control and Data Acquisition
SGD	Stochastic Gradient Descent
SHM	Structural Health Monitoring
SS	Side-Side
SSE	Sum of Squared Errors
SSI	Stochastic Subspace Identification
SSI-COV	covariance-driven stochastic subspace identification
T	Tower Fixed Coordinates
TDD	Time Domain Decomposition
TLS	Terrestrial Laser Scanning
TMM	Tower Motion Module
TUM	Technical University of Munich
UART	Universal Asynchronous Receiver Transmitter
UCE	Untwisting Cable Events
USA	Uniaxial Sensor Adjustment
UT	Ultrasonic Testing
VI	Visual Inspection
WT	wind turbine

List of Symbols

Notation	Description	Unit
D	Cumulative fatigue damage	
H	Hidden layer output	
H	Transfer function	
I	Moment of inertia	kgm^2
J	Objective function	
L	Loss function	
M	Bending moment	Nm
P	Power	kW
R	Rotation matrix	
SSE	Sum of squared errors	
Y	Dependent variable	
Φ	Yaw angle of the wind turbine	deg
Ψ	Mode shape	
Θ	Model parameter	
α	Extrinsic rotation angle about the tower fixed z-axis	deg
β	Parameter	
δ	Deflection	m
η	Learning rate	
γ	Extrinsic rotation about the tower fixed y-axis	deg
λ	Pitch Angle	deg
$\mathbf{A}$	State transition matrix	
$\mathbf{B}$	Control input matrix	
$\mathbf{H}$	Measurement matrix	
$\mathbf{I}$	Identity matrix	
$\mathbf{K}$	Kalman gain	
$\mathbf{P}$	Estimate covariance	
$\mathbf{Q}$	Process noise covariance matrix	
$\mathbf{R}$	Measurement noise covariance matrix	
$\mathbf{S}$	Innovation covariance	
$\mathbf{X}$	Input matrix	
$\mathbf{u}$	Control input	
$\mathbf{x}$	State vector	
$\mathbf{y}$	Measurement residual	
$\mathbf{z}$	Observation	
$\mathcal{L}$	Layer	
ϕ	Mode shape	
ψ	Mode shape function	
σ	Standard deviation, normal stress	
θ	Angle of deflection	deg
ε	Error term	

Notation	Description	Unit
φ	Angle between the positive x-axis (tower fixed) and the line segment from the origin	deg
a	Acceleration	m/s^2
b	Bias	
f	Activation function	
h	Hidden size	
h	Hidden state	
l	Number of layers	
s	Displacement	m
t	Sequence length	
v	Velocity	m/s
w	Weight	
w	Window function	
x	Independent variable	

List of Figures

2.1 Hybrid tower construction dimensions. 6
2.2 Measurement setup at the test facility. 7
2.3 Tower Motion Module prototype. 10
2.4 RTK data of a long-term observation. 11
2.5 Concept of a Digital Representation. 13
2.6 Soft real-time environment. 14
2.7 Conceptual visualization of rainflow counting. 19
2.8 Building blocks of Artificial Intelligence. 21
2.9 Overview of Machine Learning concepts and applications. 22
2.10 Single neuron expressing a linear regression model ($i = 1$). 24
2.11 Basic structure of a multi-layer neural network. 24
2.12 Simplified representation of an LSTM cell. 25

3.1 Wind rose and operational states of the wind turbine during period 2023-11-17 to 2024-02-14. 30
3.2 Data pipeline from measured data. 31
3.3 Wind rose and operational states of the wind turbine during period 2023-02-15 to 2024-02-23. 34
3.4 Training loss of *ACC+SCADA*, *ACC*, and *SCADA* models with varying hidden size. 35
3.5 Error distribution and prediction error of *ACC* models with hidden size 75, 25, and 12. 35
3.6 Training loss of *ACC+SCADA* model with varying sequence length and number of layers. 36
3.7 Model performance with validation data set of *ACC* models with hidden size 75, 25, and 12. 36
3.8 Detailed estimated displacement s_E, power output P_E, wind speed v_E, and acceleration a_E of *ACC+SCADA* model. 37
3.9 Detailed estimated displacement s_E of *ACC+SCADA*, *ACC*, and *SCADA*. 38
3.10 Frequency spectra of the RTK-based displacement, the TMM predicted displacement, and the acceleration data as reference. 39

List of Tables

2.1 Summary of the installed and used measurement systems. 8

3.1 Feature selection thresholds for LSTM training data. 32
3.2 Min and Max values for normalization of features & labels. 32
3.3 Employed models and corresponding features & labels. 33
3.4 Training and validation loss (L) of trained LSTM networks. 37
3.5 Population mean and standard deviation of operational parameters in the modal analysis data set. 39